Universität Bremen

and

Universidade Federal do Rio Grande do Sul

INVESTIGATION AND ANALYSIS OF THE PRE-STRAIGHTENING INFLUENCES IN AISI 1045 STEEL DRAWN BARS

M. Sc. Carla Adriana Theis Soares Diehl

May 26th, 2020

Investigation and analysis of the pre-straightening influences in AISI 1045 steel drawn bars

From the Department of Production Technology at
UNIVERSITÄT BREMEN
and
Post-Graduation Program in Mining, Metallurgical and Materials Engineering – PPGE3M at
UNIVERSIDADE FEDERAL DO RIO GRANDE DO SUL

to obtain the degree
Doktor-Ingenieur (Dr.-Ing.)

approved
Doctoral Thesis of

M. Sc. Carla Adriana Theis Soares Diehl

Advisors:	Prof. Dr. Alexandre da Silva Rocha	
	Prof. Dr.-Ing Hans-Werner Zoch	
Examination Board:	Dr.-Ing. Jeremy Epp	– Leibniz-IWT /Germany
	Prof. Dr. Gilmar Ferreira Batalha	– USP/Brazil
	Prof. Dr. Rafael Menezes Nunes	– UFRGS/Brazil
	Dipl.-Ing. Ilya Bobrov	– Leibniz-IWT /Germany

May 26th 2020

Diehl, Carla Adriana Theis Soares
Investigation and analysis of the pre-straightening influences in AISI 1045 steel drawn bars / Carla Adriana Theis Soares Diehl. -- 2020. 154 f.

Advisors: Prof. Dr. Alexandre da Silva Rocha, Prof. Dr.-Ing Hans-Werner Zoch.

Tese (Doutorado) -- Universidade Federal do Rio Grande do Sul, Escola de Engenharia, Programa de Pós-Graduação em Engenharia de Minas, Metalúrgica e de Materiais, Porto Alegre, BR-RS, 2020.
Thesis (PhD) -- Universität Bremen, Fachbereich 4 Produktionstechnik, Bremen, DE, 2020.

1. Residual Stresses. 2. Numerical Simulation. 3. Wire Drawing. 4. Pre-straightening. orient. I. Rocha, Alexandre da Silva, orient. II. Zoch, Hans-Werner, orient.

Elaborada pelo Sistema de Geração Automática de Ficha Catalográfica da UFRGS com os dados fornecidos pelo(a) autor(a).

Prepared by the UFRGS Automatic Catalog Generation System with the data provided by the author.

ACKNOWLEDGMENTS

I acknowledge:

Firstly my family: my husband Igor Luis Diehl for always being by my side dreaming and achieving dreams always together, also supporting and helping me in my scientific life, my parents Rozaldo and Neiva Soares and my brother Everton Soares for always incentivizing me to achieve my wishes, my sister in law Marina Maciel for the English corrections, my mother in law Debora Diehl and brothers in law Victor and Daniel and the sister in law Flávia for the support.

My dear friend Drª. Juliana Zottis for the psychological and scientific support.

My dear friend Drª. Fernanda Vecchietti for the tips and incentive about the co-tutelle PhD.

My colleagues from GES/UFRGS and IWT-Bremen for the help, especially to Dr. Vinicius W. Dias for the support in the submission of this work.

My advisors Prof. Dr. Alexandre da Silva Rocha (GES/UFRGS) and Prof. Dr.-Ing Hans-Werner Zoch (IWT-Bremen) for the support and the opportunity to perform the PhD in cotutelle.

Dr. Jeremy Epp for the support and guidness.

CAPES, CNPq, DAAD and DFG for the financial support. Finally, I acknowledge HZB-Berlin to allow the realization of Neutron experiments.

Table of Contents

List of Figures

List of Tables

Glossary of symbols and abbreviations

A_1 – Instant area

A_o – Initial area

C – Cold strength coefficient when φ=1

c – Constant

d – Bar diameter

D – Diagonal between the straightening rolls

$d_{0,hkl}$ – Stress-free reference lattice spacing

d_f – Final bar diameter

d_{hkl} or d – Lattice spacing or distance between the planes

d_i – Initial bar diameter

D_{max} – Maximum diameter

D_{min} – Minimum diameter

d_n – Interplanar distance from the normal plane to the surface

d_ψ – Interplanar distance from the angle "ψ" to the surface

E – Young's Modulus

E – Young's Modulus or modulus of elasticity

f – Material's deflection

F – Force

F, G, H, L, M and N – Constant features of the current state of anisotropy

h_f – Final height of the sample

h_i – Initial height of the sample

hkl – Miller indices

k_f – True Stress

k_{f0} – Yield strength of the material

k_α – Characteristic emission spectral

l – Length of the bar

n – Diffraction order

n – Work hardening coefficient

Ø – Diameter

P_m – Mean pressure

r – Radius of curvature

v – Poisson's ratio

α – Die angle

δ – Angle between the crossed rolls

Δh – Height variation

$\Delta\theta$ – Variation of Bragg angle

ε – Strain

ε_0 – Initial uniaxial strain

ε_e – Representative strain

ε_{hkl} – Network deformation

ε_x, ε_y and ε_z – Deformations in the x, y and z directions

θ – Incidence angle or diffracted angle or Bragg angle

κ – Material constant

λ – Wavelength of monochromatic radiation

μ – Coulomb friction coefficient

σ – Stress

σ_1, σ_2 and σ_3 – Main stresses in the direction 11, 22 and 33

σ_{av} – Average principal stress

σ_e – Flow stress

σ_{max} – Maximum stress

σ_o – Yield stress

σ_{oij} – Yield stress in the direction ij

σ_x, σ_y and σ_z – Normal components of stress in the x, y and z directions

σ_ϕ – Stress in the "ϕ" direction

$\bar{\sigma}_H$ – Equivalent stress of Hill

$\bar{\sigma}_M$ – Effective stress or equivalent stress described by von Mises

τ_{12}, τ_{13} and τ_{23} – Shear stress in the directions 12, 13 and 23

τ_{ij} – Shear stress in the direction ij

φ – True strain

ψ – Tilt angle of the sample

AISI – American Iron and Steel Institute

ASTM – American Society for Testing and Materials

BER II – Research reactor from Berlin/Germany

BRAGECRIM – Brazilian-German Collaborative Research Initiative on Manufacturing Technology

EBSD – Electron Backscattering Diffraction

EDM – Electrical discharge machine

FE – Finite element

FEA – Finite element analysis

FRMII – Research Neutron Source Heinz Maier-Leibnitz

FWHM – Full width at half maximum

HPS – Horizontal pre-straightening

HV – Vickers hardness

OES – Optical emission spectroscopy

PERC – Polishing and straightening by crossed rolls

RM – Raw material

SAE – Society of Automotive Engineers

TUM – Technical University of Munich

VPS – Vertical pre-straightening

WD – Wire drawing

XRD – X-ray diffraction

Title: ***Investigation and analysis of the pre-straightening influences in AISI 1045 steel drawn bars***

Abstract

The drawn bars are the raw material for manufacturing of automotive shafts for presenting high mechanical properties, good dimensional quality and surface finish. The residual stress generated in the manufacturing process can potentially lead to distortion and dimensional variations in mechanical components. Process parameters such as pressure and distance between the pre-straightening rollers, material properties, friction between the tool and the workpiece, as well as wire drawing parameters like reducing and die angle, influence the residual stresses induced in the final product. Numerical simulation is a resourceful tool to evaluate the level of influence of each parameter involved in the process: it does not require the manufacture of prototypes and it eliminates the "try-out" process which is very common in experimental procedures. The work presented herein mainly aims at investigation and improvement of the pre-straightening influences in the wire drawing process chain by investigating the behavior of residual stresses generated in the process of AISI 1045 steel bars. Besides, the variation of process parameter such distance of pre-straightening rolls, through numerical simulation and subsequent comparison with results from experimental measurements were performed. The numerical simulations of the pre-straightening process have shown heterogeneous profiles of deformation and, consequently, heterogeneous profiles of residual stress at both the surface and in the section of the simulated bars. This heterogeneity of deformation can be noted after drawing on specific areas of the workpiece, and it leads to the conclusion that the deformations are carried from one process to the next one. The changes in the distance of the rolls have shown that the first couple of the horizontal rolls has more significant influence in the distribution of stress and strains after wire drawing.

Keywords: Residual Stresses, Numerical Simulation, Wire Drawing, Pre-straightening.

Título: ***Investigação e análise das influências do pré-endireitamento em barras trefiladas de aço AISI 1045***

Resumo

Barras trefiladas são utilizadas como matéria prima para a fabricação de eixos automotivos por apresentarem propriedades mecânicas elevadas, boa qualidade dimensional e um bom acabamento superficial. As tensões residuais geradas no processo de fabricação podem causar distorção de forma e variações dimensionais nos componentes mecânicos. Parâmetros de processo como pressão e distância entre os rolos de pré-endireitamento, propriedades do material, atrito entre ferramenta/peça, bem como parâmetros da trefilação como redução e ângulo de fieira tem influência nas tensões residuais geradas no produto final. A simulação numérica é uma ótima ferramenta para a verificação da influência de todos estes parâmetros envolvidos no processo, pois é uma ferramenta que não exige a fabricação de protótipos e reduz a quantidade de "tentativa e erro", muito comum em procedimentos experimentais. Este trabalho tem por principal objetivo avaliar o comportamento das tensões residuais e distorções geradas no pré-endireitamento e trefilação do fio-máquina de aço AISI 1045 em função da variação de parâmetros do processo como pressão, distância e número de rolos de pré-endireitamento via simulação numérica e posterior comparação com resultados de medições experimentais. As simulações do processo de pré-endireitamento, mostraram perfis heterogêneos de deformações e consequentemente de tensões residuais tanto na superfície quanto na seção das barras simuladas. Essa heterogeneidade das deformações pode ser percebida após a trefilação ao longo de toda a barra e com isso, pode-se dizer que as deformações são carregadas de um processo a outro. As mudanças na distância entre os rolos de endireitamento mostraram que a primeira dupla de rolos do endireitamento horizontal influenciam na distribuição das tensões residuais após a trefilação.

Palavras chave: Tensões Residuais, Simulação Numérica, Trefilação, Processo de Pré-endireitamento, Distorções.

Titel: ***Untersuchung und Analyse des Einflusses eines Vorrichtens auf gezogene Stäbe aus dem Stahl AISI 1045***

Zusammenfassung

Die gezogenen Stangen sind der Rohstoff für die Herstellung von Fahrzeugwellen, um hohe mechanische Eigenschaften, gute Maßhaltigkeit und Oberflächengüte zu erzielen. Die im Herstellungsprozess entstehenden Eigenspannungen können möglicherweise zu Verformungen und Maßabweichungen bei mechanischen Bauteilen führen. Prozessparameter wie Druck und Abstand zwischen den Richtwalzen, Materialeigenschaften, Reibung zwischen Werkzeug und Werkstück sowie Drahtziehparameter wie Durchmesserreduzierung und Matrizenwinkel beeinflussen die im Endprodukt induzierten Eigenspannungen. Die numerische Simulation ist ein nützliches Werkzeug zur Bewertung des Einflussniveaus der einzelnen am Prozess beteiligten Parameter: Sie erfordert nicht die Herstellung von Prototypen und eliminiert den bei experimentellen Verfahren üblichen "Try-out" -Prozess. Die hier vorgestellte Arbeit zielt hauptsächlich auf die Untersuchung und Verbesserung der Vorrichteinflüsse in der Prozesskette des Drahtziehens durch Untersuchung des Verhaltens von Eigenspannungen, die im Prozess von AISI 1045-Stahlstäben erzeugt werden. Außerdem wurde die Variation von Prozessparametern wie Abstand der horizontalen Richtwalzen durch numerische Simulation und anschließenden Vergleich mit Ergebnissen aus experimentellen Messungen durchgeführt. Die numerischen Simulationen des Vorrichtprozesses haben heterogene Verformungsprofile und folglich heterogene Eigenspannungsprofile sowohl an der Oberfläche als auch im Querschnitt der simulierten Stäbe gezeigt. Diese Heterogenität der Verformung lässt sich nach dem Ziehen auf bestimmte Bereiche des Werkstücks feststellen und lässt den Schluss zu, dass die Verformungen von einem Prozess zum nächsten übertragen werden. Die Änderungen im Abstand der Walzen haben gezeigt, dass das erste Paar der horizontalen Walzen die Verteilung der Spannungen und Dehnungen nach dem Drahtziehen maßgeblich beeinflussten.

Schlüsselwörter: Eigenspannungen, Numerische Simulation, Drahtziehen, Richtvorgang, Verzerrung.

1 INTRODUCTION

The advancement and competitiveness in the field of manufacturing of metallic parts creates the need of minimizing loss of material and energy consumption. Improved understanding and control of forming processes can avoid unnecessary costs and, at the same time, permit the outcome of products of excellent quality.

The cold drawing process chain is widely employed in the manufacture of wires and bars with many section profiles. One typical process chain is presented in Figure 1.1, where the wire rod is first uncoiled and pulled through straightening rolls, sand blasted, drawn, cut and finally polished and straightened by crossed rolls (PERC).

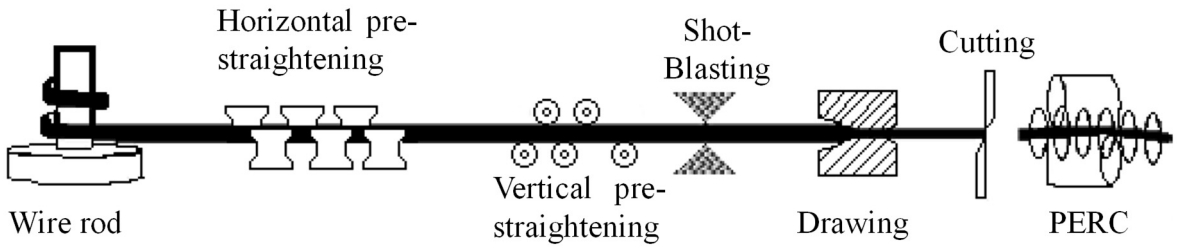

Figure 1.1: Cold drawing process chain. Source: adapted from Nunes (2012).

The pre-straightening process is required due to the bending of wire rods after uncoiling. Press rollers are applied in order to eliminate the bar pre-form by positioning the rollers in a way that causes bending moments in the wire rod leading to a straight bar at the end of the process.

Drawing is one of the oldest metal forming processes (DOVE, 1983 *apud* ATIENZA, 2001), with evidence of its use dating back to the middle of the XV century. Its use has been increased in recent years (LANGE, 2006) due to the excellent surface finishing, dimensional accuracy and gain in mechanical resistance provided by this metal forming process to the final product (DIETER, 1981, ATIENZA, 2001). Drawing reduces the diameter of a bar or wire rod by making it pass through a conical die, permitting to produce bars, wires and tubes among others.

To ensure the quality of the final product, all process' parameters must be known and controlled. Lack of control in parameters such as positioning of the straightening rolls or friction may cause losses of parts or reduce the quality of the finished products. In addition, among

other factors such as material heterogeneities, the pre-straightening parameters may generate non-homogeneous residual stresses and shape distortions (ERICSSON, 2000).

Another factor that influences residual stresses is the anisotropy, which is defined as the variation of the material's properties in different directions. Anisotropy can be caused by microstructural changes, verification of chemical composition, thermal treatments and changes in the material's shape. When the wire rod undergoes deformation as in rolling, these grains are elongated in the direction parallel to the principal axis (ATIENZA *et al*., 2005). This process decreases the yield stress in the direction perpendicular to the axis and increases the yield stress in the longitudinal direction. Therefore, anisotropy and crystallographic texture should be considered for materials that have undergone plastic deformation during their manufacturing process.

Besides, parts manufactured by mechanical forming processes may present distortions due to component's geometry, chemical composition or the generation of residual stresses in the workpiece (ROCHA *et al*., 2012; ZOCH, 2006). Eliminating the variations related to distortion in manufactured parts is essential (STEINBACHER *et al*., 2009) given that, in most cases, the removal of distortions require supplementary operations, such as machining and straightening, which incur in undesirable additional costs.

Therewith, numerical simulation is an important tool to evaluate the effects of different parameters on the drawing process, as well as of the state of residual stresses that appear in cold drawn bars. Numerical simulation eliminates the need of building prototypes and avoids costs related to unnecessary materials and processes (TEKKAYA, 2000; de SOUZA, 2011).

The metal-mechanic industry has been showing a growing interest to produce superior quality parts that combine surface finish and mechanical resistance with reduced costs and despite the initial cost of simulation software, this software is an important tool to reduce costs in industrial processes.

In cold forming processes, products can be manufactured with great dimensional accuracy, making subsequent machining operations unnecessary, thus reducing the final costs of the process. On the other hand, metal forming processes, in general, consist of materials' transformation involving more than one additional process such as machining, straightening and heat treatment processes, to achieve a desired final shape, change the materials' properties and guarantee the required hardness (DIETER, 1988). Those additional processes, as well as metal forming processes such as the cold draw process chain, generate distortions and residual

stresses that must be removed or minimized. For this reason, each step of the process chain should be investigated.

In this context, according to Wang & Gong (2002) there is no doubt that all cold-drawn and inductively hardened automotive components show dimension and shape distortion. This distortion needs to be eliminated by straightening processes at the end of manufacturing and also by controlling of the pre-straightening process prior to wire drawing. With the application of numerical methods, variations of the influencing parameters can be investigated without loss of material or extra costs. Beyond that, it permits the process to be observed as a whole, and the distribution of residual stresses to be evaluated at different intermediate process steps. Lastly, the continuous development of this technique and the correct input of process' parameters can result in optimized products for the industry.

In the wire drawing process chain, which is the topic of this study, the pre-straightening process generates an amount of deformation in the bar that depends on the magnitude of the applied bend (PAECH, 2001). Proper verification of shape distortions from residual stresses generated by these deformations in the pre-straightening and drawing processes is essential to avoid losses in the final product and to reduce costs with distorted pieces at the end of the manufacturing process.

Parameters such as pre-positioning of the straightening rolls and bar shape influence are critical for the evaluation of residual stresses and represent important boundary conditions to be taken into account as input in the simulation process (CHEN *et al*., 2014). The topic of this study has significant relevance as considering the influence of the rolls in the shape of bars, and consequently, of the residual stresses at the end of the pre-straightening process, can lead to new knowledge about the distortions that appear in the bar after heat treatment and also to a better understanding of the effect of process' parameters in the whole process chain.

The work presented herein mainly aims at investigation and improvement of the pre-straightening influences in the wire drawing process chain by investigating the behavior of residual stresses generated in the process of AISI 1045 steel bars. Besides, the variation of process parameter such as the shape of the bar and distance of pre-straightening rolls, through numerical simulation and subsequent comparison with results from experimental measurements were performed. For the main objective to be successfully achieved, the following goals were defined:

- Identification of the sources of heterogeneous deformations in the process chain;
- Analysis of the equipment employed for pre-straightening;

- Prediction of the residual stresses generated in the pre-straightening process by numerical simulation;
- Prediction of residual stresses and strains after the drawing process via numerical simulation;
- Experimental characterization of residual stresses generated in pre-straightened and drawn bars.
- Verification of the relationship between the positioning of the straightening rolls and the profile of residual stresses generated in the processes.
- Comparison between numerical simulation and experimental results.
- Study of the heterogeneity of deformation after the wire drawing process chain.
- Proposal of a new rolls configuration for the straightening process.

The intention of this research project is to evaluate this memory effect found by Nunes (2012) due to deformations carried during the process chain according to the stresses and distortions generated in the final bars. An overview of the methodology applied to the process chain is shown in Figure 1.2.

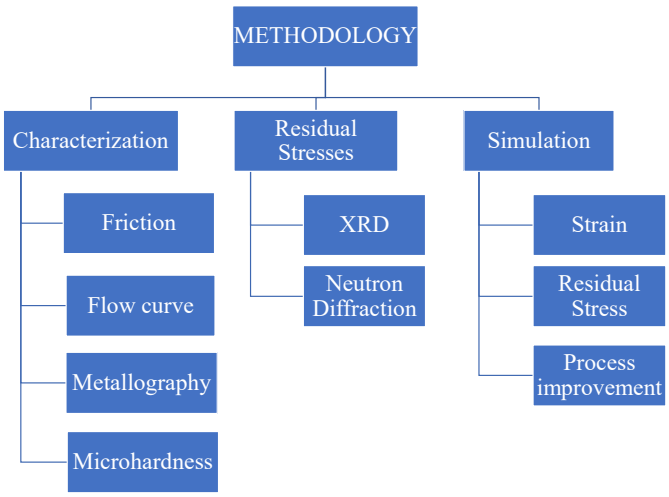

Figure 1.2: Overview of the methodology.

Based on numerical simulation of pre-straightening and drawing processes, X-ray and neutron diffraction analysis and microstructural analysis, this study means to contribute scientifically and technologically to aspects such as:

- Understanding of the distribution of strains generated in the process through the relationship between the arrangement of the pre-straightening rolls and the profile of residual stresses after drawing;

- Understanding the generation of residual stresses in the pre-straightening process and the relationship of their distribution with distortion;
- Optimizing the parameters of the pre-straightening process by evaluating numerical simulation results in order to reduce residual stress levels;
- Possible improvement in the process that could lead to considerable gains of productivity.

This thesis encompasses the chapters entitled as introduction, theoretical background, experimental measurements, numerical experimentation, general discussion, conclusions and, ultimately, bibliographic references.

The introduction chapter is composed by a brief explanation of the process, the study's motivation, the main objective, specific goals and the thesis' contribution. The theoretical background chapter presents the theory involved in the addressed subject. Thereafter, the experimental part includes a discussion of the applied methodology, as well as the presentation of the results and the assessment of the results. The numerical analysis part follows the same structure, covering methodology, results and discussion. Then, a general discussion about the experimental results and numerical analysis is presented, followed by the work's conclusions.

2 THEORETICAL BACKGROUND

To structure the work, a review of important topics in the field of residual stresses in metal forming has been conducted, covering the necessary theory to understand and to perform the experimental work, as well as the numerical analysis. A brief explanation of the wire drawing process chain, focusing on the pre-straightening process, was given. Moreover, a state-of-the-art review of the wire drawing process chain, material, residual stresses, distortions and numerical analysis was carried out.

2.1 WIRE DRAWING PROCESS CHAIN

The wire drawing process chain is widely used in the manufacturing industry of wires, bars, shafts, screws, among others. After casting and hot rolling, the wire rod is stored in a Ø1.2 m coil which gives to the bar a curved shape. To perform the drawing step, the bar should have a certain straightness to avoid tool breakage, high level of residual stresses, distortion, among other problems. This is the reason why there are two pre-straightening processes before the wire drawing.

The wire drawing process chain is represented schematically in Figure 2.1. The process consists of uncoiling of the wire rod, passage of the wire through the steps of vertical and horizontal pre-straightening, blasting, drawing, cutting and finally polishing and straightening with crossed rolls (PERC).

Figure 2.1: Schematic of wire drawing process chain. Source: Adapted from Dias (2013).

2.1.1 Pre-straightening process

Nakagiri and Inakazu (2004) state that for the accomplishment of a drawing processes, the wire rod should have a certain degree of straightness. This is because a high amount of bending in the wire rod raises considerably the drawing force and may cause a premature break of the tool (die) and reduce the fatigue life of the product.

The pre-straightening process consists in the arrangement of several forming rolls for the passage of the wire rod that needs to be straightened due to its curvature resulting from the storage coil as shown in Figure 2.2. Pre-straightening is the most common process employed to eliminate the curvature due to the initial shape of the wire rod or to heat treatments applied in forming products (FISCHER & SCHLEINZER, 2002). The number of rollers depends on the quality criteria of the required linearity for the wire rod. The positioning of these rollers influences the mechanical properties of the bar and the amount of spring back at the straightened part (NASTRAN & KUZMAN, 2002).

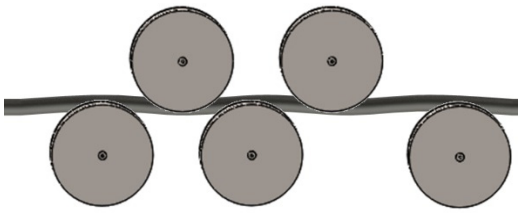

Figure 2.2: Schematic view of a sequence of rollers for pre-straightening. Source: adapted from Espinoza (2007).

Straightening of wire has a wide field of applications that go from wire drawing to finished and semi-finished products (PAECH, 2001). Such process is one of the key production steps (PAECH, 2008) as it provides to the wire the straightness necessary to reduce the required process force and also a good finish to the product. Additionally, straighteners are often used to create a defined residual curvature in the production of straight wires, when it is required.

In order to improve straightness in wire rods, an additional step of vertical pre-straightening is used in the wire drawing process chain. Mutrux *et al*. (2010) and Yoshida and Sugiyama (2009) affirm that research on the pre-straightening process are rare and little is known about the correct positioning of the rollers and the effect on the residual stresses due to the positioning of these rollers.

Nastran and Kuzman (2002) explain that, although it has been insufficiently studied, the pre-straightening stage is extremely important for the quality of the final product, that being due to the heterogeneities of the strains involved in the process that cause residual stresses and distortion in the final piece.

Das Talukder and Singh (1991) presents a detailed analysis of the mechanisms of straightening in a finished product that has anisotropic behavior as well as heterogeneities along its length. The material is affected by each process in a unique and special way (PAECH, 2001) and, as a result, stresses arise and/or remain inside the straightened material. The generated

stresses are a function of the applied load type (SRIMANI *et al.*, 2005; FISCHER & SCHLEINZER, 2002) and of the zone affected by straightening, which changes according to the initial curvature of the wire rods, e.g., a greater curvature induces deeper plastic deformation in the material (YOSHIDA *et al.*, 2010 *apud* NUNES, 2012).

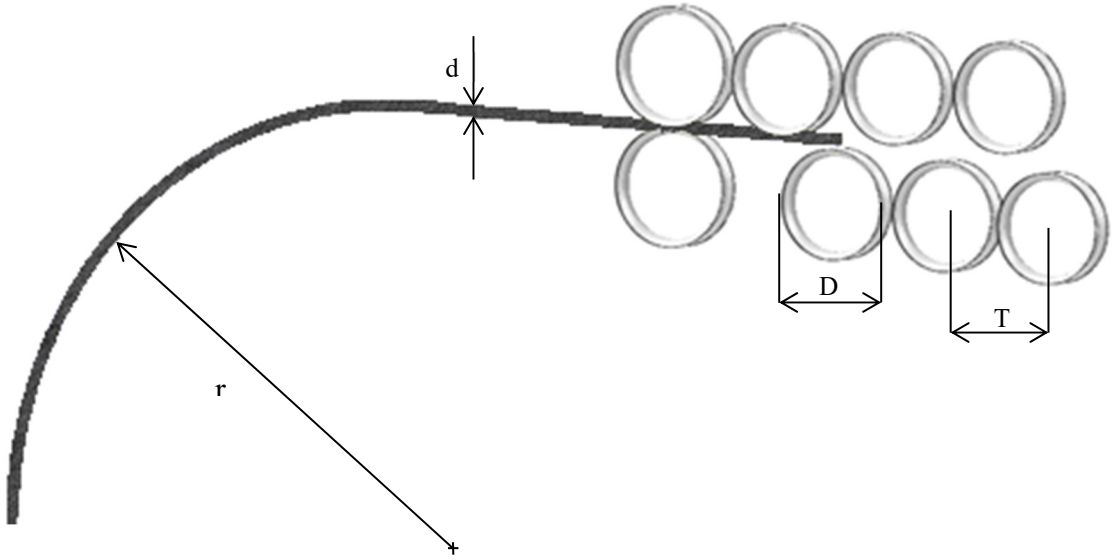

Figure 2.3: Schematic view of raw material preform in a horizontal roll straightening process. Source: adapted from Paech (2008).

Figure 2.3 shows the pre-straightening process and its variables. In addition to the working rollers, there are two guide rolls preceding the process. The maximum and minimum diameter (D) of the guide rollers are calculated by Equation 2.1 and Equation 2.2, respectively.

$$D_{min} = 2.\left[\frac{d.E.r}{d.E + 2.kf_0.r}\right] \qquad \text{Equation 2.1}$$

$$D_{max} = 2.\left[\frac{d.E.r}{d.E - 2.kf_0.r}\right] \qquad \text{Equation 2.2}$$

where “E” is the Young’s Modulus (GPa), “d” is the bar diameter (mm), “kf_0” is the yield strength of the material (MPa) and “r” is the radius of curvature (mm) (PAECH, 2002). The radius of curvature is calculated by Equation 2.3.

$$r = \frac{f^2 + {}^{l^2}/_4}{2.f} \qquad \text{Equation 2.3}$$

where “f” is the material’s deflection (mm) and “l” is the length of the bar (mm), according to the scheme shown in Figure 2.4.

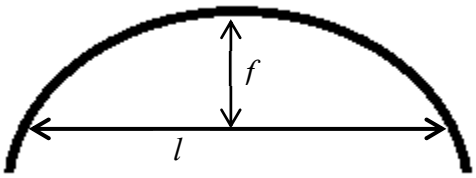

Figure 2.4: Deflection *f* over the length *l.* Source: adapted from Paech (2001).

To define a good straightening machine to straighten a wire, it is necessary to know the material properties and the maximum and minimum dimensions of the bar cross-section. Based on this, the number of straightening rolls should be decided (PAECH, 2007). Both the radius of curvature and the number of rolls have an influence on the quality of the final product (LEE *et al.*, 2007; PAECH, 2001).

The pre-straightening step, which is an important step of the wire drawing process chain, is required due to the bending which the wire rod gets from the storage coil. This step consists of vertical and horizontal pre-straightening, as shown in Figure 2.5. The curvature of the wire rod may damage the drawing tool and greatly enhance the required force of the process, as well as incur in results with shape distortion. Thus, the wire rod must have a degree of linearity for the drawing process to be performed (NAKAGIRI & INAKAZU, 2004; NUNES, 2012).

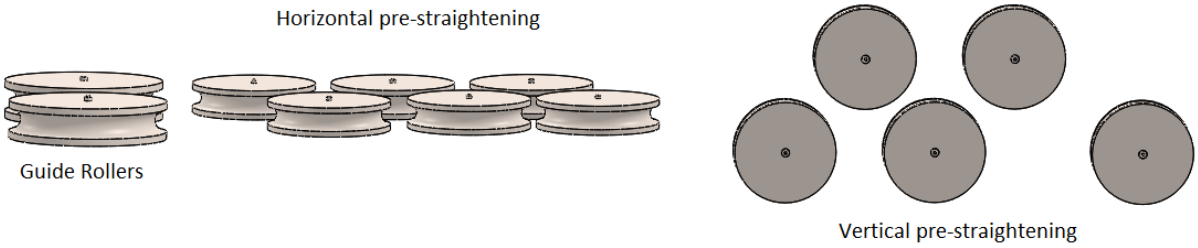

Figure 2.5: Schematic view of rolls set of the pre-straightening process: horizontal (a) and vertical (b). Source: adapted from Paech (2001).

2.1.2 Shot blasting

In the wire drawing process, shot blasting is used for cleaning the wire rod as it is a quick, simple and less costly alternative. The process consists of the jet of small particles of steel, ceramic or polymer, with diameters ranging from 50 microns to 6 mm, which impact the surface of the material removing oxides formed during hot-rolling, one of the first steps in the

material manufacture (TANGE & ANDO, 2000; NUNES, 2012; de SOUZA, 2011). The speed of these particles may reach 150 m/s on the surface of the wire rod, causing plastic deformation at the locations of collision. Such located plastic deformation causes an elongation of the surface of the material, generating tensile stresses within the material that produce compressive residual stresses on the workpiece surface (LIU, 2005; de SOUZA, 2011).

Results from shot blasting performed by Nunes (2012) point out that the residual stresses have a compressive or tensile behavior depending on the peripheral position in which the wire rods are touched by the jet, along the same axial peripheral position.

Upon reaching the part, the jet shot makes the stresses compressive on the surface of the bar and tensile below the surface. The differences in the residual stresses in the peripheral positions of the bar observed by Nunes (2012) show that these stresses remained of pre-straightening processes are not superimposed in the shot blasting process.

2.1.3 Wire drawing

Drawing is defined as a plastic deformation manufacturing process in which the wire rod is pulled through a tool (die), causing a reduction in the cross section area of the bar and an increase in its length (DIETER, 1981; BÖLLINGHAUS *et al.*, 2009, MERKEL & ENGINEER, 2015). The process is composed by indirect compressive forces and the primary forces applied are often tensile. However, indirect compressive forces developed as a reaction between the material and the die reach high values, allowing the material to flow in a combined stress state that includes high compressive forces in at least one of the main directions (DIETER, 1981).

One of the main features of drawing is to produce high-quality precision parts and besides that, drawing increases the tensile strength and yield stress of the material due to the work hardening process the material undergoes during the process. Figure 2.6 shows a schematic model of the drawing process.

Figure 2.6 shows drawing of a rod passing through the die, which is the tool used for the drawing process, due to the application of a pulling force F applied linearly and continuously (MERKEL & ENGINEER, 2015). The wire rod enters the drawing tool with an initial diameter d_i and, after crossing the die, it exits with a final diameter d_f, smaller than the original diameter. This reduction in diameter is caused by plastic deformation in the conical region of the die.

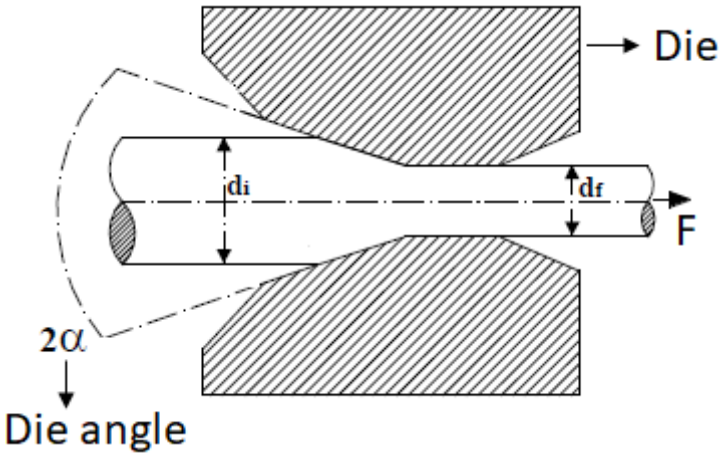

Figure 2.6: Schematic view of the drawing process. Source: adapted from NUNES (2012).

The die can be made with different shapes and geometries, with or without coating to reduce friction or to protect the die, depending on the application of the required product. This tool is generally made of hard metals with Tungsten Carbide due to the great durability and high hardness (WANG & GONG, 2002). These metals are produced by compression of sintered metal powder in high temperatures in furnaces with controlled atmosphere, and the final shape is obtained by scraping and polishing with diamond paste. In Figure 2.7 the drawing tool (die) can be observed.

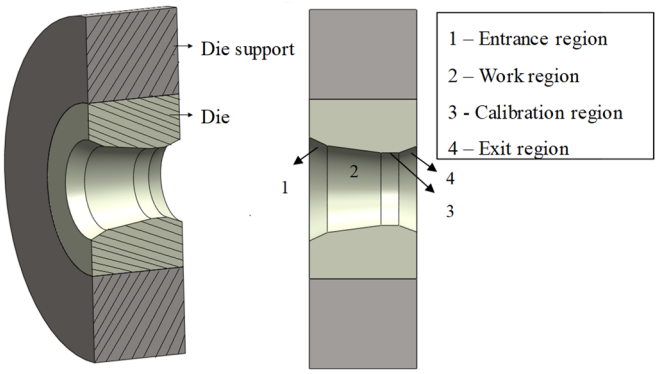

Figure 2.7: (a) Drawing tool and (b) parts of the die. Source: adapted from Soares (2012).

Figure 2.7 *(a)* represents the shape of the die. The outside part of the die contains a support made of steel, whereas the inside part is made of Tungsten Carbide or diamond. In general, the die has four regions of importance for the drawing process (DIETER, 1981; KABAYAMA *et al.*, 2009; de SOUZA, 2011), as illustrated in Figure 2.7 *(b)*, where: region one is the cone or angle of entry, which directs the wire rod into the die; region two is the cone or working angle, where the metal is deformed; region three is the calibration area where adjustment of the wire's diameter and stabilization of the material's mechanical properties take

place; lastly, region four, namely exit region, facilitates the exit of the wire rod and the adherence between the material's surface and the die in case of an interruption in the process.

Analyzing the drawing process involves not only assessment of the tool, but also the consideration of a significant number of factors that influence the process, such as: the effort required to perform the operation, lubrication of the die/metal interface, finishing and final mechanical properties of the product, to name a few (METZ, 2007; SANTOS, 2008; de SOUZA, 2011).

In metal forming, wire drawing is used to manufacture parts such as wires and tubular or cylindrical bars with applications in vehicles, construction machinery, tools, textile machines and industrial equipment (SANTOS, 2008).

2.1.4 Cutting, polishing and straightening by crossed rolls and hardening

The cutting process is part of the process chain has and it influences the residual stresses in the region to be cut. In the process chain addresses by this study, the drawn bar is cut into six-meter long pieces and, after polishing and straightening by crossed rolls (PERC), the long bars are cut one more time into short pieces of 400 mm. According to Dias *et al.* (2015), the cut region affected by residual stresses can reach 30 mm from the bar cut, or 15% of the final piece.

After the first cutting process, the bar moves to the PERC, which is the final process in the chain. The PERC process is composed by two rolls, one concave and another convex, positioned with an angle δ between them, as indicated in Figure 2.8. In this process, deformations are generated by the convex roll when the bar moves along, producing compressive residual stresses on the surface of the bar (NUNES, 2012). The angle δ may vary from 10 to 20 degrees, depending on which material is being used, and it has an influence on the final residual stresses of the bar.

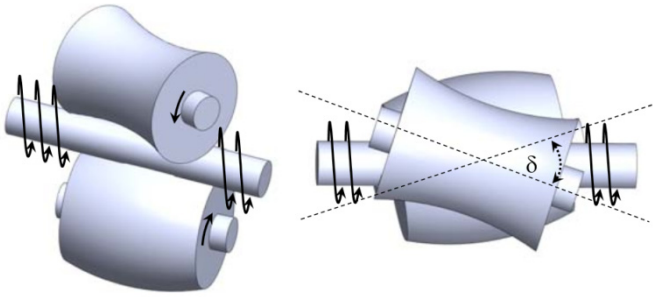

(a) (b)

Figure 2.8: Schematic view of PERC process rolls: (a) 3D view and (b) top view. Source: Nunes (2012).

2.2 MECHANICAL PROPERTIES

2.2.1 Flow stress

The yield strength describes the elastic behavior region, determining the maximum limit that the stress can reach before the material enters plastic flow (DIETER, 1981). It is an important factor that is associated with the generation of residual stresses in the cold drawn bars. Figure 2.9 shows the stress vs. strain curve from a typical tensile test.

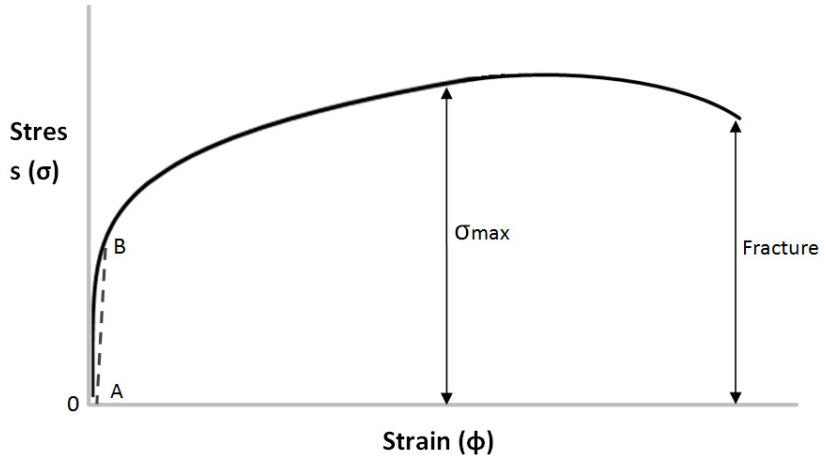

Figure 2.9: Stress-strain curve of a tensile test. Source: adapted from Dieter (1981).

The phenomenon of flowing of a given metallic material may be observed during experimental tests, resulting in the curve shown in Figure 2.9. Following this curve, it is possible to understand that, if the equivalent stress in the sample is lower than the yield stress (point B), the material behaves elastically and the tension stress in the sample is linearly proportional to the deformation as stated by the Hooke's law. When loading ceases, the material returns to its original dimensions.

In the case of tension stress in the sample exceeding the yield stress, the material's elastic behavior is replaced by a plastic behavior, and the stress-strain relationship is no longer linear. When unloaded, the material will not return to its initial shape. Plastic behavior is often defined, in metallic materials, when deformation exceeds 0.2%, corresponding to the B in the curve shown in Figure 2.9. The elastic region of the stress-strain curve is governed by the Hooke's law, expressed by Equation 2.4*:*

$$\sigma = E.\varepsilon \qquad \text{Equation 2.4}$$

where "σ" is the stress (MPa), "ε" is the strain and "E" is the Young's Modulus or modulus of elasticity (GPa).

Within the plastic region, or the region where the material behaves non-linearly, an equation that predicts the inelastic behavior in cold process was proposed by Ludwig-Hollomon and is expressed in Equation 2.5.

$$k_f = C.\varphi^n \qquad \text{Equation 2.5}$$

where "k_f" is the stress (MPa), "C" is the cold strength coefficient when φ=1 (MPa); "n" is the strain hardening coefficient and it always assumes values lower than 1.0.

The equivalent strain, in the case of the drawing process, is described by the deformation of the area, φ, of the drawn bar. This equivalent strain can be calculated by Equation 2.6.

$$\varphi = \ln\frac{A_0}{A_1} \qquad \text{Equation 2.6}$$

The shape and amplitude of a flow curve, in the first stage, are function of the chemical composition of the metal, its orientation, the test temperature and the strain rate (DIETER, 1981). For isotropic materials, the flow limit is the same for every direction (x, y and z). However, anisotropic materials, such as materials that have suffered major deformations during manufacturing, present yield strength with distinct values for each main direction. In drawn round bars, flow stress of the tangential and radial directions can be considered equal due to the symmetry characteristic of this process (CARLSSON & HUML, 1996).

The flow curve showed in Figure 2.9 can be simplified for implementation in numerical modeling. Some possible simplifications are shown in Figure 2.10.

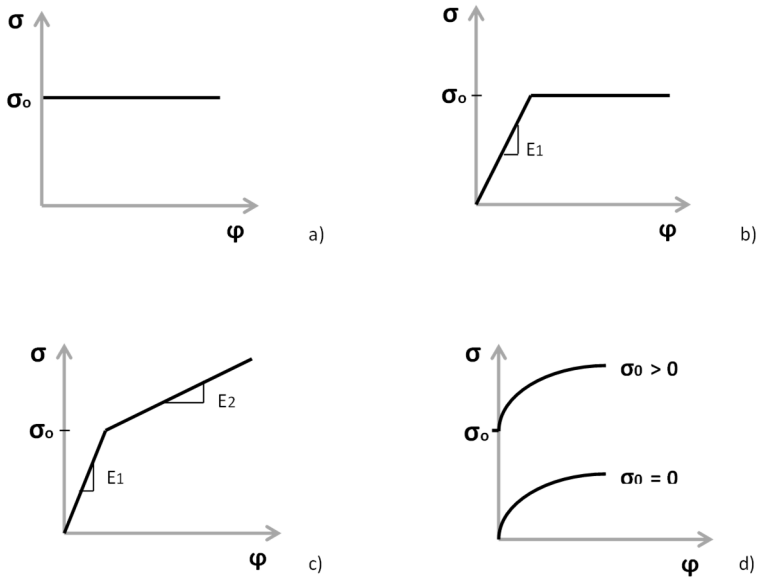

Figure 2.10: Material behavior of the true strain vs. true stress in (a) perfectly plastic; (b) perfectly elastoplastic; (c) perfectly elastoplastic with linear strain hardening; and (d) parabolic strain hardening
Source: Meyers & Chawla (2009).

In Figure 2.10, it is possible to notice the disparities in the behavior presented by different metallic materials when they undergo deformation. The perfectly plastic state (Figure 2.10 *(a))*, occurs when the material does not present an elastic response nor undergo strain hardening. The behavior presented in Figure 2.10 (b), typical of perfectly elastoplastic materials, does not show strain hardening, and possesses an elastic portion of the curve that cannot be neglected.

The case of perfectly elastoplastic materials with linear strain hardening, Figure 2.10 *(c)*, is a good approximation of the real behavior of materials. This curve is characterized by two distinct slopes, E_1 and E_2, that represent the elastic and plastic behavior of the material, respectively.

In Figure 2.10 *(d)*, parabolic strain hardening is shown, which should be used when representation of the strain hardening of the material is important. This behavior is expressed by the Ludwik-Hollomon's equation (Equation 2.5), that derives the flow stress curve of the material, k_{fo} (MEYERS & CHAWLA, 2009) as shown in Equation 2.7.

$$k_f = k_{fo} + C.\varphi^n \qquad \text{Equation 2.7}$$

The experimental tests most commonly used to obtain the flow curve are the compression and tensile tests. The tensile test is one of the most widely used tests for determining the mechanical behavior of materials, including elastic deformation, flow, plastic deformation and fracture. In this test, the maximum deformation is limited by necking, e.g., the data about the plastic behavior of the material collected during deformation are valid only until necking is initiated (DAVIS, 2004). The samples used for tensile tests need to be prepared following a specific geometry, which is pre-determined by the standard. Meanwhile, the samples for the compression test require a cylindrical geometry, which is simpler to obtain than those of the tensile test. The compression test can also be used to determine the material flow curve. This test results in strains higher than the strains obtained with tensile test (HOSFORD, 2010).

For polycrystalline materials, results obtained with both the tensile and the compression tests are generally equal with respect to elastic and plastic deformations. Moreover, the elasticity modulus, the yield stress and the flow curves show similar behavior in both tests (DAGNESE, 2012).

2.2.2 Isotropy

Macroscopic isotropy is the characteristic of materials that present the same mechanical properties independently of the considered direction (HOSFORD, 2010). Such materials have a homogeneous microscopic structure, and their elastic properties are defined by the modulus of elasticity (E) and the Poisson's ratio (v).

One of the criteria that describe the flow of isotropic materials was developed by von Mises in 1913 in the form of a quadratic function shown in Equation 2.8 (DIETER, 1981; MARTINS & RODRIGUES, 2005). Such criterion considers that plastic deformation begins when the distortion's elastic energy value per volume unit reaches a critical value.

$$\bar{\sigma}_M = \frac{1}{\sqrt{2}}[(\sigma_1 - \sigma_2)^2 + (\sigma_2 - \sigma_3)^2 + (\sigma_3 - \sigma_1)^2]^{1/2} \qquad \text{Equation 2.8}$$

where σ_1, σ_2 and σ_3 are main stresses (MPa) and $\bar{\sigma}_M$ is the effective stress or equivalent stress described by von Mises (MPa).

2.2.3 Anisotropy

The physical and mechanical properties of crystals generally depend on the crystallographic direction in which they are measured. The dependence of properties with direction is defined as anisotropy (CARLSSON & HUML, 1996; HOSFORD, 2010).

It is essential to understand how anisotropy affects a material, as this may be of crucial importance for the forces and deformations involved in the drawing process and in the residual stress profile (ATIENZA *et al*., 2005). There are two distinct types of anisotropy: mechanical and crystallographic anisotropy (MEYERS & CHAWLA, 2009).

Anisotropy is normally caused by crystallographic texture, wherein grains are preferably aligned in certain crystallographic directions of the material. Anisotropy may also arise from mechanical texture, originated from the aligned grain flow due to grain deformation. This deformation, in turn, can be caused by forming processes, such as rolling, drawing, forging or extrusion (HOSFORD, 2010). The property that is affected by anisotropy to a larger extent is the flow stress.

Mechanical anisotropy often emerges during the later stages of deformation, therefore influencing fracture. This anisotropy occurs due to the alignment of metal's grains and the

particles of the second phase along specific directions, generally parallel to the wire axis, in the case of drawing.

There are various proposed criteria with the objective to evaluate the anisotropy of a material. The criterion proposed by Hill in 1948, however, is the one that requires fewer experimental tests in order to obtain the necessary parameters to describe the anisotropy and is the basis for all other criteria (BANABIC *et al.*, 2000).

Hill has defined his criterion of anisotropic flow by simplifying the criteria originally proposed by von Mises, presented in Equation 2.8. Hill assumed in his theory that the material has symmetrical characteristics with respect to three orthogonal planes (x, y, z), that the initial yield stress (σ_o) depends on six components (σ_1, σ_2, σ_3, τ_{12}, τ_{13} and τ_{23}), and defined the equation with one second-order polynomial (HILL, 1948; ATIENZA *et al.*, 2005; DITIX & DITIX, 2008, HOSFORD, 2010), which can be observed in Equation 2.9:

$$F(\sigma_2-\sigma_3)^2+G(\sigma_3-\sigma_1)^2+H(\sigma_1-\sigma_2)^2+2.L.(\tau_{23})^2+2.M.(\tau_{31})^2 + 2.N.(\tau_{12})^2=(\bar{\sigma}_H)^2 \quad \text{Equation 2.9}$$

where: F, G, H, L, M and N are constant features of the current state of anisotropy and $\bar{\sigma}_H$ is the equivalent stress of Hill (MPa). F, G and H may be determined by compression tests and L, M and N by shear test or by empirical equations (MASSÉ *et al.*, 2011). The omission of linear terms in Equation 2.9 and the appearance of differences between normal stress components come from the assumption that the response of the material is equal in tension and in compression (OLIENICK FILHO, 2003).

The constants in the Hill's criterion can be expressed as functions of the yield stress in the x, y and z directions related to the ratio of the yield stress in each direction and the initial yield stress. Expressions to calculate the Hill's indexes using experimental data of the yield stress are shown in Equation 2.10 to Equation 2.15*:*

$$2F=\frac{1}{(\sigma_{o22})^2}+\frac{1}{(\sigma_{o33})^2}-\frac{1}{(\sigma_{o11})^2} \quad \text{Equation 2.10}$$

$$2G=\frac{1}{(\sigma_{o11})^2}+\frac{1}{(\sigma_{o33})^2}-\frac{1}{(\sigma_{o22})^2} \quad \text{Equation 2.11}$$

$$2H=\frac{1}{(\sigma_{o11})^2}+\frac{1}{(\sigma_{o22})^2}-\frac{1}{(\sigma_{o33})^2} \quad \text{Equation 2.12}$$

$$2L=\frac{1}{(\tau_{o23})^2} \quad \text{Equation 2.13}$$

$$2M=\frac{1}{(\tau_{o13})^2} \quad \text{Equation 2.14}$$

$$2N = \frac{1}{(\tau_{o12})^2} \quad \text{Equation 2.15}$$

where σ_{oii} and τ_{oij} are related to the stresses determined by Equation 2.16 to Equation 2.18. The anisotropy indices in Equation 2.10 to Equation 2.15 are determined by the relationship between the yield stress, for each direction, and the principal stresses (σ_{av}), from Equation 2.16. For the shear case, Equation 2.17 expresses the relationship between the shear stress in each direction and the initial shear stress. Shear stress is proportional to the yield stress of the material and, according to von Mises, flow occurs in shear test under the condition expressed by Equation 2.19 (CARLSSON & HUML, 1996; SANTOS, 2005; ATIENZA *et al*., 2005):

$$\sigma_{oii} = \frac{\sigma_{ii}}{\sigma_{av}} \quad \text{Equation 2.16}$$

$$\tau_{oij} = \frac{\tau_{ij}}{\tau_o} \quad \text{Equation 2.17}$$

$$\sigma_{av} = \frac{\sigma_{11} + 2.\sigma_{22} + \sigma_{33}}{4} \quad \text{Equation 2.18}$$

$$\tau_o = \frac{k_{fo}}{\sqrt{3}} \quad \text{Equation 2.19}$$

In the flow direction (deformation of the material), the resistance of forged steel is higher along its longitudinal axis and decreases in the transverse direction. The number of elastic and plastic constants also increases when comparing an isotropic material to an anisotropic, since the magnitude of the deformation produced by each strain varies with the orientation.

2.2.4 Strain hardness correlation

The material properties and the influence of each process parameter need to be investigated in order to solve problems involved in the manufacturing process chain such as residual stresses and distortions. Sonmez & Demir (2007) affirms that hardness profiles can be related to the forgeability of the material undergoing a cold forming process. Hardness and strains measurements, according to Zottis *et al.* (2018), are important parameters that can be related to each other using a computational numerical approach. Tabor (1948) developed an empirical approach to convert strain into hardness.

For the compression test, the Ludwig-Hollomon Equation (Equation 2.20) can be applied if the assumption that the material under uniaxial loading is valid.

$\sigma = k \cdot \varepsilon^n$ (Equation 2.20) $HV = 0.9272(Pm)$ (Equation 2.21)

$\mathrm{Pm} = \mathrm{c}\ (\sigma_e)$ (Equation 2.22) $HV = ck(\varepsilon_0 + \varepsilon_e)^n$ (Equation 2.23)

where "κ" is a material constant and "n" is the coefficient of work hardening. In the Vickers hardness (HV) test, a diamond squared pyramid is forced onto the part being tested through a pyramidal indenter. HV is defined as the load divided by the surface area of the permanent impression and its value is given by the Equation 2.21, where P_m is the mean pressure (applied force divided by the projected area).

Tabor (1948) assumed that there is a representative flow stress (σ_e) that is linearly related to the mean pressure (Equation 2.22). Based on the hardness values obtained through samples that had been compressed using several reductions, Tabor concluded that if the initial uniaxial strain (ε_0) is additive to the representative strain (ε_e=0.08) using a constant c of 2.9, then HV may be expressed by Equation 2.23. By taking the previously presented analytical equations and combining them with simulation results of compression tests with different reductions, a strain–hardness correlation can be obtained.

2.3 RESIDUAL STRESSES

2.3.1 Definition and origin

Residual stresses are the result of the interaction of time, temperature, deformation and microstructure. The material characteristics that trigger residual stresses are, among others, the thermal conductivity, modulus of elasticity and Poisson's ratio, plasticity, kinematic and thermodynamic transformations, mechanisms of transformation and plastic processing (BHADESHIA, 2002).

In the wire drawing process chain, the material undergoes plastic deformations. As a result, internal stresses are often created due to different levels of deformation taking place at the same time and in different regions of the part (KALPAKJIAN, 2000).

Differences in the strain levels may appear due to disparities in the strength of the phases in the material, the different shapes of the die and/or the temperature gradient along the piece (WANG & GONG, 2002; MARTINEZ-PEREZ *et al.*, 2005; MARTINS & RODRIGUES, 2005). In wire drawing, for a small reduction of about 10%, induced internal stresses may

remain in the piece after the end of the process in the form of residual stresses. These residual stresses are further influenced along the steps of the process chain. However, there are evidences that a "memory effect" of residual stresses occurs from one stage to the next, i.e. the inhomogeneous elastic/plastic deformations that cause these stresses are not completely superimposed by the subsequent step and thus are carried out through the entire manufacturing process affecting the “memory effect” (NUNES, 2012).

Residual stresses are usually defined as the balance of existing internal stresses in a body free from the influence of external forces or boundary restrictions. These stresses are induced in the workpiece on purpose or unintentionally during manufacturing and they modify the mechanical behavior of the material, affecting the mechanical strength, fatigue and corrosion resistance (GALAMBOS, 1998; WANG & GONG, 2002; MARTINS & RODRIGUES, 2005). These remaining stresses are within the elastic range, therefore the maximum effective value that can be achieved is the actual yield stress of the material after being deformed (DIETER, 1981). The analytical calculation of residual stresses is extremely complex, hence numerical calculation or experimental measurements are often used (MARTINS & RODRIGUES, 2005).

Residual stresses can be minimized by heat treatments such as annealing or stress relief. However, these are additional treatments that require operator time and increase the cost of the process, not to mention that such treatments can reduce the surface hardness of the product, which is not desirable in some cases. Another way to reduce residual stresses is to optimize the geometry of the employed tool by evaluating its deformation zone, as it has a significant impact on the generation of such stresses (WANG & GONG, 2002).

Tensile residual stresses are particularly critical at the surface of parts and, in some cases, can lead to immediate failure by brittle fracture, decrease of the fatigue life and corrosion under tension (METZ, 2007; NUNES, 2008). On the flip side, compressive residual stresses at the surface of the bar are beneficial for the fatigue life of the material and, if necessary and desirable, can be induced in the sample through different process as shot blasting (PERINI, 2008). When a large reduction in diameter is done by the drawing process, experimental results indicate that the residual stresses are distributed as tensile stresses on the surface of the bar and as compressive stresses in the center (YANG *et al.*, 2008).

To properly identify the type of stress that is being measured, one must know the distinction between micro stresses and macro stresses (WALTON, 2002). Micro stresses result from changes in the atomic level and is balanced on small volumes. Conversely, macro stress

is the result of operations involving large deformations, such as forging, rolling and drawing (RUUD, 2002). There are basically three kinds of residual stresses (ATIENZA, 2001):

- First order, which are macroscopic, easy to measure and can span over several grains of the material;

- Second order, microscopic or structural microstress, which are limited to one grain or portion thereof;

- Third order, which are found at the atomic level strictly in a part of the grain;

Despite forming processes generate macro stresses in the produced parts, micro-stresses are also generated at the atomic level of the material. Measurements of these stresses in a specimen are held at the atomic level and only in one phase of the material. In materials that have more than one phase, the residual stresses can differ from one phase to another (Van ACKER *et al.*, 1996; NUNES, 2012). In order to obtain a more concise result of the macro stresses, an average of all phases is calculated so that the experimentally measured stresses can be compared to the overall amount of residual stresses provided by computer simulation (NUNES, 2012).

Experimental techniques that permit measuring residual stresses involve destructive methods that require the removal of a portion from the sample's strained material to induce stress redistribution in the rest of the analyzed specimen. On the other hand, non-destructive measuring methods are available, in particular diffraction techniques which use the interatomic spacing of a set of crystallographic planes in the stressed material for the measurement of residual stresses.

Residual stresses are difficult to be precisely calculated by analytical methods. Therefore, the variety of experimental measurement methods has been increasing in the recent years. As a result, selecting the appropriate method has become a complex task that must consider various features to be successful (KANDIL *et al.*, 2001).

2.3.2 Residual stresses in the wire drawing process chain

Residual stresses are important factors to be considered for workpieces that have gone through a forming process. The roller straightening process induces several non-homogeneous deformations. These deformations generate residual stresses, which create a distortion at the end of the process chain. According to Espinosa (2007), the largest contribution of residual

stresses to the final product is due to the pre-straightening process, and that fact is usually not considered according to Paech (2002).

Varney & Farris (1997) have used the elastic-plastic theory to study the distribution of residual stresses of straightened rail track beam and as a result they found a zig-zag pattern of longitudinal stresses. In addition, residual stresses from roller straightening by in the peripheral angular position was measured by Krause *et al.* (1978) and as a result a non-rotationally symmetrical residual stress distribution with large amounts of tensile and compressive stresses was found. The profile of residual stresses obtained by Varney & Farris (1997) is shown in Figure 2.11 (a) and the profile in the peripheral angular position measured by Krause *et al.* (1978) is shown in Figure 2.11 (b).

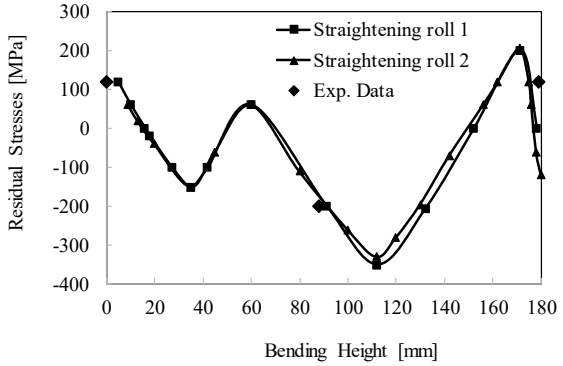

(a)

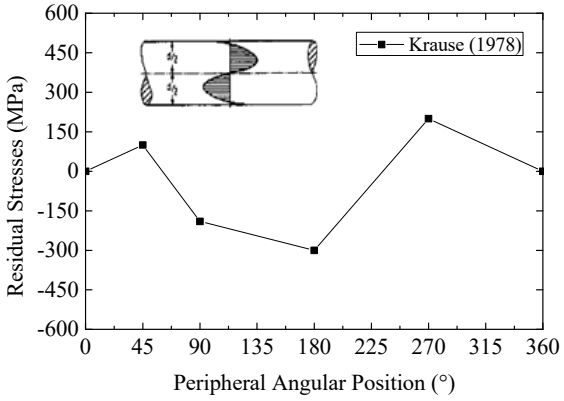

(b)

Figure 2.11: (a) Profile of residual stresses in a straightened sample (Adapted from Varney & Farris (1997)) and (b) profile of residual stresses in the peripheral angular position of a straightened sample (Adapted from Krause *et al.* (1978)).

Atienza *et al.* (2012), on the other hand, studied the generation of residual stresses in drawn bars employed in concrete structures using numerical simulation and experimental procedures involving X-Ray and Neutron diffraction. In his work, Atienza called the attention to the importance of studying residual stresses in drawn bars, once the stresses caused by

heterogeneous deformations within the material may cause failure, modification of mechanical properties and even reduction of the fatigue life of components.

De Souza (2011) de Souza *et al.* (2012) conducted axisymmetric simulations, using finite element method, of residual stresses generated during wire drawing of AISI 1045 steel round bars. The author compared numerical results with experimental measurements of residual stresses from neutron diffraction and applied equations from the literature to evaluate forces and deformations. De Souza (2017), after applying simulation to evaluate the wire drawing tool, reinforced the need of pre-straightening being included in models used to predict residual stresses after the process chain.

Nunes (2012) investigated variations of five parameters of the wire drawing process chain in order to identify distortion potentials present in the manufacturing route: running, die angle, straightening angle, stress relief temperature and depth of hardened layer. The residual stresses were characterized at all stages of the process employing techniques that include X-Ray diffraction, Neutron diffraction and Synchrotron radiation diffraction. In addition, the author concluded that the analysis of residual stresses should be extended in order to investigate the existence of a "memory effect" of the residual stresses from one step to next in the process chain.

Following this same line of studies, Dias (2013) examined the effects of residual stresses and hardness in the cutting region of bars that passed through a wire drawing process chain. The cut by shear and saw were evaluated as potential carriers of distortion in bars.

Zoch (2009 and 2006) affirmed in his works that distortions are changes in size and shape suffered by components in the manufacturing path and that, even though these have been studied for over a century, they still cause significant economic losses. Epp *et al*. (2010a) recognized that interactions between the state of residual stresses and the behavior of distortions still need to be clarified, as numerous factors influence the occurrence of these distortions.

2.3.3 Measurement methods

At the moment, no universal method is available that can fulfill all desirable requirements for an ideal experimental test, such as low cost, short measurement time, availability, etc. (DIAS, 2013). However, some key parameters should always be considered in order to choose the best technique to perform a residual stress experiment. These parameters

will depend on the nature of the component, the type of residual stress present in the component, the gradient of the residual stresses and the geometry of the component, to name a few.

There are several experimental methods available to measure residual stresses. These methods are divided into non-destructive (e.g. X-Ray, Neutron diffraction and Synchrotron radiation), semi-destructive (hole drilling) and destructive methods (deflection methods). In the current section, some of these methods will be discussed.

2.3.3.1 Residual stress analysis by Neutron diffraction

In Neutron diffraction method, the strain components are obtained by measuring the distance between crystallographic planes resulting from the presence or not of residual stresses (WEBSTER, 1992). For a monochromatic beam of wavelength λ impinging on a material, the Bragg equation (Equation 2.24) describes the angular positions of the maximum values for a family of crystallographic planes with distance "*d*" (EZEILO & WEBSTER, 1999; NUNES *et al.*, 2010).

$$n.\lambda = 2.d_{hkl}.\sin\theta \qquad \text{Equation 2.24}$$

where "θ" is the incidence angle or diffracted angle from the Neutron radiation, "λ" is the wavelength of monochromatic radiation, "d_{hkl}" is the distance between the planes and "*n*" may be any positive, non-zero integer, named diffraction order.

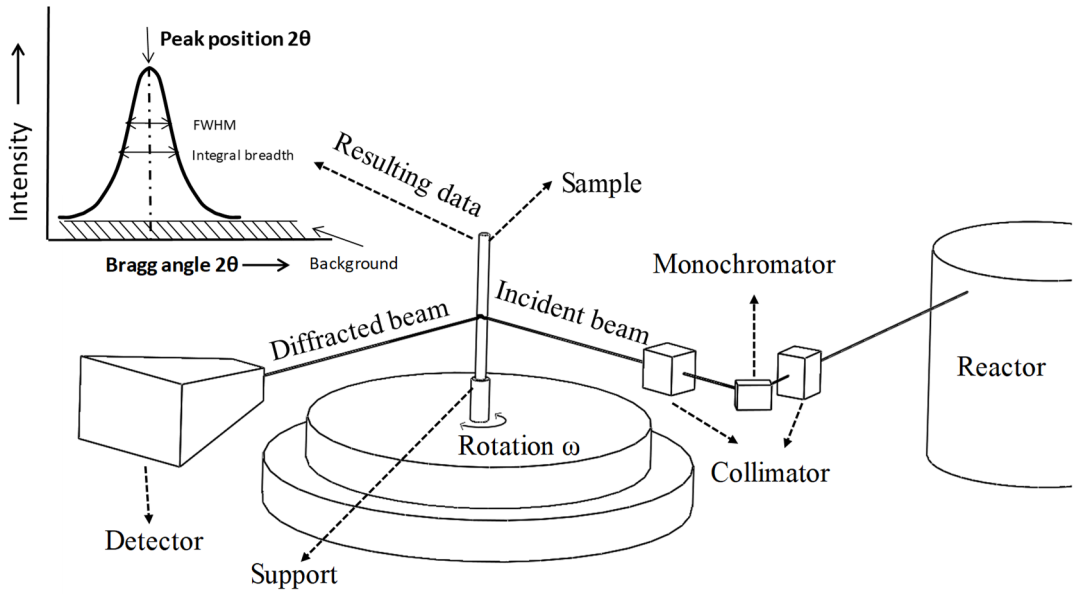

Figure 2.12: Schematic view of diffraction measurements using monochromatic Neutron beam. Source: adapted from Webster (1992).

A schematic drawing of the measurement is shown in Figure 2.12. In the figure, an incident monochromatic beam generated by a reactor can be observed as it impinges on the sample, being posteriorly diffracted. As a result of the measurement, peak positions (2θ), incidence angle or diffracted angle of each point are obtained.

A small variation in the lattice spacing "*d*" is sufficient to change the "Δθ" in the angle position "θ" of the Bragg reflection, so that the network deformation "ε" is given on the vector direction for a monochromatic beam, as shown in Figure 2.12. The generated deformation is given by Equation 2.25:

$$\varepsilon_{hkl} = \frac{d_{hkl} - d_{o,hkl}}{d_{o,hkl}} = -\Delta\theta . \cot\theta \qquad \text{Equation 2.25}$$

where "ε_{hkl}" is the network deformation, "d_{hkl}" is the d-spacing measured using Bragg's law and "Δθ" is the variation of the angular position. The "$d_{0,hkl}$" is the stress-free reference lattice spacing that can be measured in a small stress-free cube in different Omega positions.

Finally, to determine the stresses at one position within the material, three measurements in three orthogonal directions (x, y and z) should be performed and evaluated according to Equation 2.26 to Equation 2.28*:*

$$\sigma_x = \frac{E}{(1+v).(1-2.v)} . \left[(1-v).\varepsilon_x + v.(\varepsilon_y + \varepsilon_z)\right] \qquad \text{Equation 2.26}$$

$$\sigma_y = \frac{E}{(1+v).(1-2.v)} . \left[(1-v).\varepsilon_y + v.(\varepsilon_x + \varepsilon_z)\right] \qquad \text{Equation 2.27}$$

$$\sigma_z = \frac{E}{(1+v).(1-2.v)} . \left[(1-v).\varepsilon_z + v.(\varepsilon_x + \varepsilon_y)\right] \qquad \text{Equation 2.28}$$

where "E" is Young's modulus (GPa), "v" Poisson's ratio, ε_x, ε_y and ε_z are deformations in the x, y and z directions, σ_x, σ_y and σ_z are the normal components of stress in the x, y and z directions (MPa).

One of the advantages of the Neutron diffraction technique is the penetration of the beam of Neutron, capable of reaching depths up to 40 mm in the sample greater than that of the X-Ray diffraction technique, allowing for a larger portion of the material to be analyzed (EZEILO & WEBSTER, 1999). A disadvantage of this method is the high cost of the sophisticated equipment involved.

2.3.3.2 Residual stress analysis by X-Ray diffraction

X-ray diffraction is a technique used to identify the crystalline phases in materials and to measure residual stresses. In addition, the method is employed to determine present phase texture, phase contents, thickness of thin films, multilayers and atomic arrangements in amorphous materials (BRUNDLE, 1992).

In the field of residual stress, the X-ray diffraction technique presents certain limitations. Residual stresses in the core of a material with large grain size and in heavily textured crystallographic materials can be difficult or even impossible to measure by X-ray diffraction (ERICSSON, 2014).

Basically, this technique uses the same theory as that of the neutron diffraction technique. The monochromatic X-ray impinges in the material, producing diffraction peaks that are modified according to the variation of the material properties (NUNES, 2012). The residual stresses are obtained by evaluating the elastic deformation of the crystals, once the elastic constant of the material is known and assuming the stress proportional to the deformation (DIAS, 2013, RUUD, 2002).

The lattice spacing, caused by residual stresses are evaluated using the Bragg's law (Equation 2.24), whereas the deformation generated by this spacing can be calculated using Equation 2.25. Hence, a number of stresses in any direction between the interplanar spacing may be determined using Equation 2.29 (FITZPATRICK, 2005).

$$\sigma_{\phi} = \frac{E}{(1+v).sin^2\psi}.\frac{d_{\psi} - d_n}{d_n} \qquad \text{Equation 2.29}$$

where "σ_{ϕ}" is the stress in the "ϕ" direction; "ψ" is the tilt angle of the sample; "d_{ψ}" is the interplanar distance from the angle "ψ" to the surface and "d_n" is the interplanar distance from the normal plane to the surface.

When choosing between X-Ray and Neutron diffraction, one should take advantage of the specific characteristics of each of them. For instance, Neutron diffraction can be used to measure deeper residual stresses, until the center part, whereas X-ray diffraction is more effective at the surface, capturing the stresses up to a depth of less than five micrometers or as successive layer removal (HAUK, 1997; RUUD, 2002). The typical beam size of X-Ray is 1/6 of the radius of a cylindrical specimen for a 5% error and ¼ for 10% error in the hoop direction (LU, 1996). The Figure 2.13 shows the penetration depth varying with the angle 2θ for the Cr and Cu radiation in the Psi tilt 0° (ROCHA, 2000).

Some limitations of the X-ray diffraction method are related to metallurgical parameters such as the presence of impurities and gaps, which are often impossible to detect in order to implement corrections. Other limiting factors for the use of the method are the high cost of the equipment and the emission of radiation associated with the measurement method.

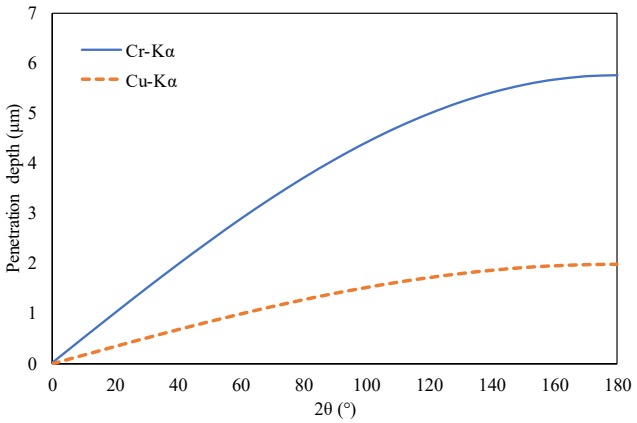

Figure 2.13: Penetration depth of Cr and Cu radiation. Source: adapted from Rocha (2000).

2.4 DISTORTION

Distortions are mainly generated by volume variations caused by mass or density changes and by plastic and elastic deformations. The aforementioned factors lead to variations in size, due to alteration of dimensions, and in shape, due to alteration of angles and curvatures of the components. Changes in size and shape are known as distortions (LÜBBEN, 2014).

Distortions generated by residual stresses have been a target of research for decades. The lack of homogeneity in the distribution of residual stresses within a part is a decisive parameter for the resulting distortion. (EPP *et al.*, 2010a). Distortions in the mechanical components are associated with the manufacturing history of the material (ZOCH, 2006) and depend on: a) the geometry of the components; b) the chemical composition and local variations; c) the mechanical history of the components; d) time and temperature sequences during manufacturing; e) the microstructure and phase transformation; f) relaxation and generation of tension/compression/residual stresses.

Figure 2.14 presents a list of factors that generate distortions in a part after heat treatment, causing variations in shape and size due to stresses generated by thermal gradients, manufacturing processes and heat treatment, among others.

Initial geometric imperfections or distortions resulting from the manufacturing processes quantitatively represent the distance of the real surface to the idealized surface during the workpiece manufacture. These distortions represent a setback for manufacturing, as the deviations in shape and final dimensions affect the finished product, in addition to generating excessive costs related to the discard of these defective products. (ZOCH, 2006).

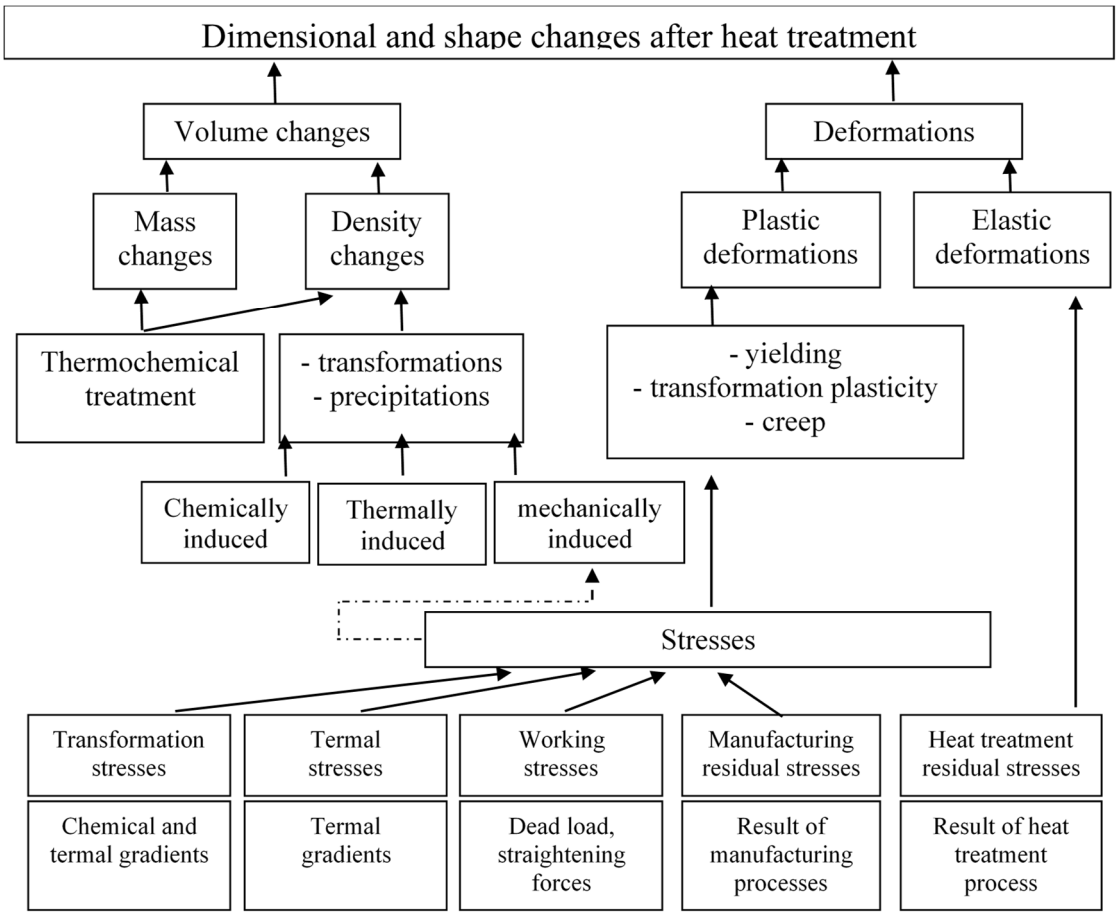

Figure 2.14: Causes of changes in size and shape afer heat treatment. Source: Adapted from Lübben (2014)

In the wire drawing process chain, a major source of losses during processing of the material is distortion. The study of residual stresses becomes of vital importance as these stresses are directly linked to the distortion issue. The probable "memory effect" of residual stresses, quoted by Nunes (2012), may be a significant distortion potential, incurring in distortions at the end of the wire drawing process chain. Therefore, controlling this important feature of the process becomes essential in order to reduce costs due to loss of material caused by distortions in the final product, and thereby to increase the product competitiveness in the market. (ROCHA *et al.*, 2012; ZOCH, 2006).

2.5 NUMERICAL ANALYSIS

The term “finite element” was first introduced in the 50s in the field of civil engineering. Its first application was in solving structural analysis problems. In manufacturing processes, the use of this analysis method started only in the 60s. The first developed programs were based on a solid formulation for infinitesimal deformations, resulting from a generalized form of existing structural analysis programs, which did not consider nonlinearities associated with geometry and material resulting from large deformations (MARTINS & RODRIGUES, 2005; ARAÚJO, 2009)

In the 70s, a formulation for plastic flow, which characterized the metals’ material flow under plastic deformation, was developed following a form analogous to that of the flow of viscous incompressible fluids. Plastic extensions were neglected, the material was described by laws of rigid-plastic/viscoplastic behavior and the relationship between stress and strain rate was based on the constitutive equations of Levy-Mises (DIETER, 1981; MARTINS & RODRIGUES, 2005; GEIER, 2007).

Subsequent to the formulation for plastic flow, two-dimensional simulations were developed, first in the steady state for rolling processes and extrusion, and later in the non-steady state with manual remeshing. In the late 80's and early 90's, the automatic mesh generation technology was developed in parallel to the emergence of powerful computational workstations that favored the practical use of finite element simulations (OH *et al.*, 1991; GEIER, 2007).

In recent years, finite element methods (FEM) have gained considerable attention as they became proven to be a great tool for analyzing mechanical forming processes, including the analysis of residual stresses (WANG & GONG, 2002). Industries around the world have been using numerical simulation for cost optimization and quality improvement in product implementation, development of new products in less time, increasing the know-how in the process and assistance in training (TEKKAYA, 2005; ARBAK, 2007).

Simulation is already an integrated part of the manufacturing process of many products in several industries. The use of simulations can eliminate prototyping, thus reducing costs and material and energy losses, as well as improving the technological parameters of metals and the quality of the final product (TISZA, 2004; SOUZA, 2011).

For forming processes, numerical simulation can be employed for predicting the material flow, dimensions and positioning of the parts, residual stresses, temperature

distribution, the exercised force, tool wear, distortions, as well as any defects or flaws that can surge during shaping. Moreover, numerical simulation can aid the evaluation of the microstructure and the residual stresses generated at the end of the process chain, among other parameters and/or problems, avoiding material loss and unnecessary expenses that would exist if the residual stresses were evaluated experimentally (ALTAN & VELAZQUEZ, 1996; SCHAEFFER *et al.,* 2005; de SOUZA, 2011).

Besides, in the last years, several studies were conducted involving simulation and experimental measurements of residual stresses in the pre-straightening process. However, most part of the literature regarding this process focuses on applications for railway rails manufacturing (ZHAO *et al.,* 2011; PUTTEN & DAUBE, 2010; ESPINOZA, 2007; TALAMINI *et al.,* 2004; FISCHER & SCHLEINZER, 2002).

Talamini *et al.* (2004) developed different models for two and three-dimensional finite elements analysis to predict residual stresses generated during the pre-straightening process in railways. This study investigated the effect to the residual stress profile caused by the load characteristics generated by the process, the influence of distortions on these stresses and the effect of heat treatment performed on the rails in the final profile of residual stresses. Later, Putten & Daube (2010) developed a computational simulation model of the pre-straightening process related to long rails. The authors stated that distortions in long products are caused by residual stresses induced by heterogeneities due to plastic deformation and the effects of the friction coefficient. In addition, the authors concluded that an approximation by finite element method is required in order to analyze the internal stresses of the material during and after the pre-straightening process.

Martins & Rodrigues (2005) explains that, since the analytical calculation of residual stresses is extremely complex, numerical calculations or experimental measurements are normally chosen to determine these stresses. Therefore, numerical simulations may be implemented to the study of the pre-straightening process as a tool to facilitate the evaluation of the rollers' positioning.

Finite-element-based programs divide the deformable workpiece in several compatible elements interconnected by nodal points on the boundaries to generate accurate results at the end of the analysis. The displacement field within each finite element is approximated by shape functions. The nodal values of the functions are unknown. The shape of the displacement field determines the distribution of deformations and the constitutive equations. The balance of equations for all nodes and boundary conditions is enough to determine all the unknowns and,

thus, give a final response for the specimen under analysis (GAMBIN, 1977; NORASETHASOPON & YOSHIDA, 2008; ARAÚJO, 2009).

The subdivision of the deformable workpiece is called meshing and it generally consists, for two-dimensional cases, of triangular or quadrilateral elements, and of hexahedral elements for three-dimensional cases. The elements' vertices are called nodes of the mesh. The mesh or grid is composed of elements, compound's faces and nodes, which are points of intersection and connection between the elements (HUTTON, 2004).

Certain care must be taken when the model is created to avoid errors in the numerical simulation. For instance, to simulate an anisotropic material, a non-axisymmetric model is suitable, and a three-dimensional model should be created, or symmetry should be assigned to the model, when possible. Assigning symmetry to the model reduces the computational time and contributes to the stability of the numerical calculations (TEKKAYA, 2005). In the case of wire drawing, assigning symmetry means simply simulating only a part of the bar and assuming the same results for the remaining parts of the bar.

The most common numerical problems are associated with the variables shown in Figure 2.15. In order to ensure accuracy, a detailed study of these variables should be performed.

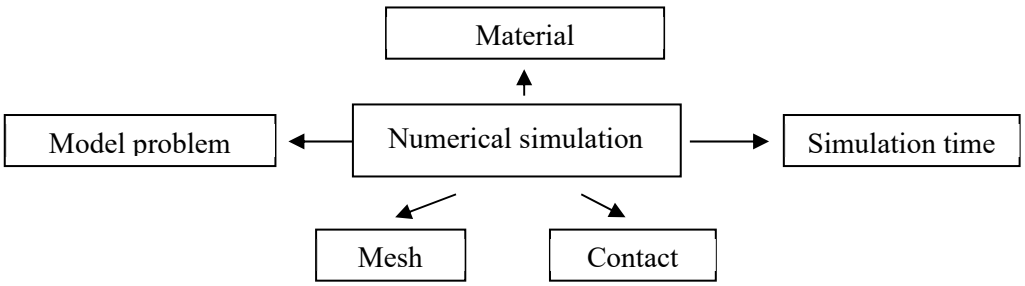

Figure 2.15: Main variables in a numerical simulation. Source: adapted from Aponte (2001).

Another precaution to avoid errors in the simulation is in the definition of the material model to be used. Two types of material models are most commonly input in the software for metal forming processes: rigid-plastic or elastoplastic materials (VAN BAEL, 1991).

When rigid plastic material model is selected, all information about the elastic behavior of the material is ignored and therefore the solution algorithm is unable to compute residual stresses in the product after forming.

On the other hand, in the elastoplastic model, the disadvantage present in the rigid-plastic model do not exist. For the elastoplastic material model, the yield curve and the

hardening data are needed in order to calculate the plastic deformation and the stresses occurring in the material.

3 METHODOLOGY

In this chapter, the methodology applied for the experimental measurements and simulations is presented in detail.

3.1 EXPERIMENTAL PROCEDURE

The wire drawing process chain under study (illustrated in Figure 3.1) is utilized in the production of shafts and is divided into uncoiling, horizontal and vertical pre-straightening, shot blasting, wire drawing and cutting. Closing the process chain, there is the process of polishing and straightening by crossed rolls, which is not covered by the work presented herein.

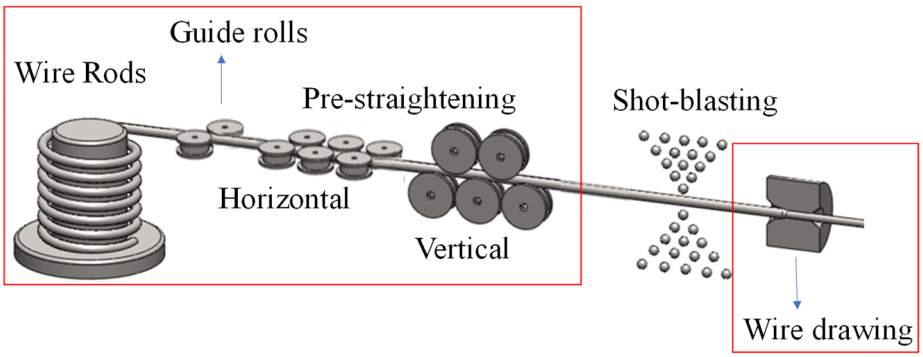

Figure 3.1: Investigated wire drawing process chain. Source: adapted from Dias (2013).

Figure 3.1 depicts the typical sequence of steps evaluated through experimental measurements. The process chain starts with the uncoiling and the pre-straightening processes, which are important steps concerning bar straightness. Posterior to those steps, the wire is shot blasted with the intent to remove the scale. According to Nunes (2012), the shot blasting process has a low distortion potential and therefore has no major influence on the residual stresses remaining after the wire drawing. The next step on the process chain is the cold wiredrawing. Finally, the bar crosses through polishing and straightening by crossed rolls that, according to Nunes (2012), will strongly modify the residual stress state in the final bar.

The bars that were 6 m-long are cut again into small pieces of 400 mm in length and then are subjected to additional manufacturing steps, such as machining and induction hardening treatment. The 400 mm-long bars are employed in the manufacturing of final products, e.g. shafts of automotive dampers or transmission shafts. Due to all these operations, the cold-drawn bars will show some distortion – a deflection up to some tenths of a millimeter

– at the end of the process. The correction of this distortion requires an additional bend-straightening and/or grinding, incurring in additional costs and in delay of delivery.

In order to achieve the goal of this work, experimental characterization of the wire rod, the pre-straightened bar and the drawn bars were carried out. The results are expected to aid the identification and understanding of the sources of non-homogeneities, such as strains and residual stresses generated during the process chain. For that, evaluation of the microstructure, hardness and residual stresses will be performed.

3.1.1 THE INVESTIGATED PROCESS

The wire rod manufacturing process starts with steel production at the steel plant. The first step of the steel production is the cast of scrap and pig iron using an electric arc furnace. The next steps are the primary and secondary steel refining, where the control and/or addition of elements such as Carbon, Silicon, Manganese, deoxidizing, among others is performed. Finally, the last step at the steel production is the continuous casting that is responsible for the steel solidification. After solidification, the ingot with a square section (150 x 150 mm^2) pass through a subsequent hot rolling, reaching the final round shape with a diameter of around 21 mm and a length of several meters. The wire rod is then stored in large coils of 1200 mm in diameter.

The wire drawing process chain begins with uncoiling of the wire rod (Figure 3.2a). This stage requires especial attention due to the wire rod's curvature developed during the storage phase, which will have induced residual stresses in the wire rod.

Even after uncoiling, the wire rod remains curved and presents an irregular shape. Hence, it must be pre-straightened before the drawing process proceeds. Subsequent to the pre-straightening process, the wire rod is guided by a pair of guide rolls with diameter of 250 mm. The equipment employed for pre-straightening is formed by several rollers, which are arranged in two groups that are responsible for two distinct processes. The first process is named horizontal pre-straightening (Figure 3.2b) and it is performed by a set of six rollers with diameter of 230 mm. The following process, named vertical pre-straightening, occurs over a set of five rollers with diameter of 192 mm (Figure 3.2c). Residual stresses generated in the shot blasting process are not evaluated in this study and were characterized by Nunes (2012).

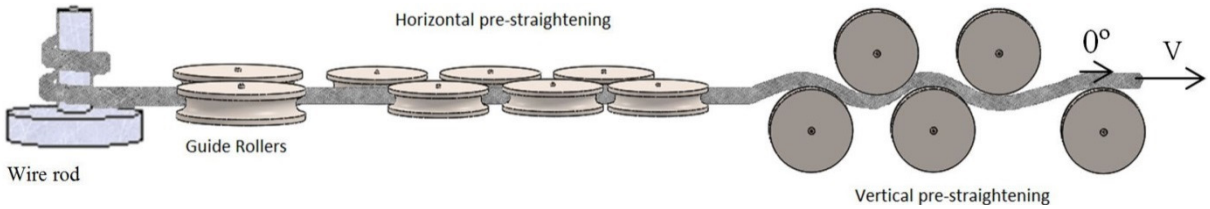

(a) **(b)** **(c)**

Figure 3.2: (a) raw material (b) Horizontal and (c) vertical pre-straightening steps.

In this study, the wire drawing process was performed with a total die angle (2α) of 15 degrees (°) manufactured with hard metal encapsulated with an AISI 1045 steel. The selection of the 15° die was based on previous results from a research carried out within the BRAGECRIM project (Brazilian-German Collaborative Research Initiative on Manufacturing Technology), where the performance of two die angles, 15° and 20°, was investigated. Results showed that, in the bars drawn with the 15° die angle, the longitudinal residual stresses were more homogeneous than those of the bars drawn with the angle of 20°. Furthermore, the die with 15° exhibited higher penetration of plastic deformations than that of the die with the angle of 20° (NUNES, 2012).

Examining the straightened material and defining requirements for the final product require identification and specification of characteristics of the material prior and posterior to the process. The characterization is based on relevant geometric parameters, such as cross-sectional geometry and curvature, and the mechanical properties of the material. In this work, the following experimental measurements were carried out:

- ✓ Determination of the flow curve in two directions of the wire rod, obtaining anisotropy indices that were used as input to the simulation software;
- ✓ Definition of the hardness distribution to be correlated with the simulation strains;
- ✓ Metallographic and EBSD analysis;
- ✓ Analysis of residual stress distribution using X-Ray diffraction and Neutrons Diffraction, aiming at comparing the results with the simulation results;

The samples were collected at four distinct stages of the process chain, which are indicated in Figure 3.3. The flow curves were obtained by compression tests (using samples from stage 1, just before the guide rolls). Samples from all four stages were used to measure residual stresses and perform metallographic analysis, whereas samples from the stage 4 were subjected to Electron Backscatter Diffraction – EBSD.

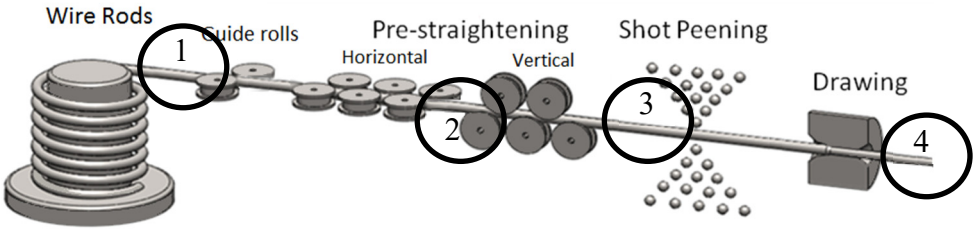

Figure 3.3: Places of withdrawal of samples. Source: Adapted from Dias (2013).

3.1.2 MATERIAL CHARACTERIZATION

3.1.2.1 Chemical composition

The chemical composition of the AISI 1045 steel employed in this work was measured by optical emission spectroscopy (OES) in samples from each step of the process chain: wire rod, horizontal pre-straightening (HPS), vertical pre-straightening (VPS), wire drawing (WD). OES was also performed by Dong *et al.* (2016) in the same material but using a different lot. The measured values are compared with the maximum and minimum values allowed by the standard SAE J-403:1994 and listed in Table 3.1. It is possible to notice a deviation in the values corresponding to the Mn element, which is within the limits allowed by the standard though.

Table 3.1: Chemical composition of the AISI 1045 steel.

Alloying element / % mass	C	Si	Mn	P	S	Cr	Mo	Ni	Cu	Nb
OES-raw material	0.46	0.27	0.77	0.016	0.024	0.14	0.03	0.07	0.2	0.009
OES-HPS	0.47	0.27	0.76	0.016	0.024	0.14	0.03	0.07	0.2	0.008
OES-VPS	0.47	0.26	0.76	0.018	0.024	0.13	0.03	0.07	0.2	0.008
OES-WD	0.46	0.26	0.77	0.017	0.021	0.13	0.03	0.07	0.2	0.008
Standard	0.43-0.5	-	0.6-0.9	0.03	0.05	-	-	-	-	-
Dong *et al*. (2016)	0.47	0.23	0.87	0.024	0.034	0.09	0.02	0.08	0.16	0.02

Source: Dong *et al*. (2016) and standard SAE J-403:1994

3.1.2.2 Flow curve

Determining the flow curves of a specific material is extremely useful, as they can describe the plastic behavior of the material during a given metal forming process. Compression tests are commonly used to define the flow curves of a material due to the large plastic strains which can be achieved in the same ranges as in metal forming processes.

Compression tests were performed on cylindrical samples of Ø10 x 15 mm collected from the transverse and axial directions of the raw material, as it can be observed in Figure 3.4. Six cylindrical samples were machined from the 0º direction (axial to rolling), whereas other six samples were machined from the 90º direction (transverse to rolling). Due to the process being continuous, just the raw material was evaluated in this step.

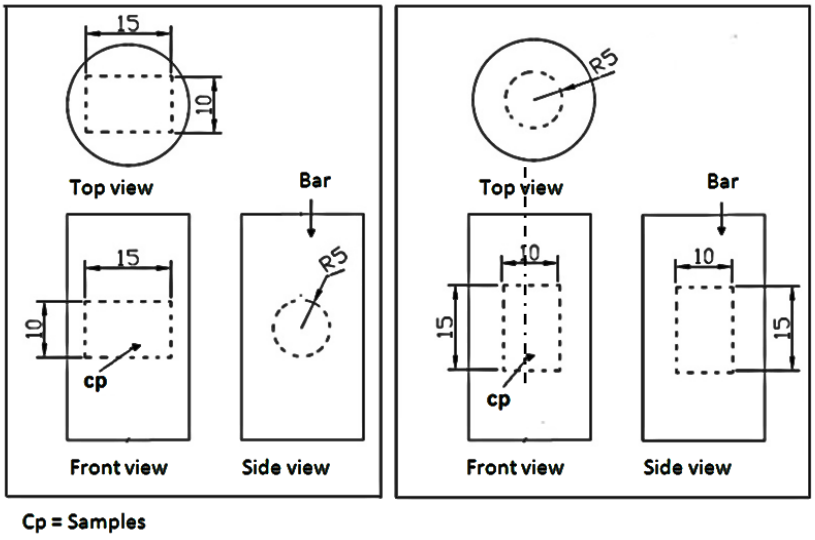

a) b)

Figure 3.4: Location of samples in (a) hoop and (b) axial directions. Source: SOARES (2012).

For compression tests, it is recommended that the ratio of the height and the diameter (h_i/d_i) of the specimen does not exceed 1.5 (HOSFORD, 2010) so buckling can be avoided, and friction effects can be minimized.

The experimental tests were performed in a universal testing machine, INSTRON/EMIC model EMIC 23-600, with a maximum capacity of 600 kN (at room temperature) using graphite powder as lubricant. The pressing speed was maintained as constant at 5.0 mm/s. The flow curves were calculated from the average result of each direction.

Two flow curves were obtained for the axial and transverse directions of the wire rod and are plotted in Figure 3.5. The flow stress corresponding to 0.2% strain in the axial direction

(0°) was equal to 390 MPa. In the transverse direction (90°), it was equal to 349 MPa, which is 10% smaller than the flow stress in the axial direction. In terms of anisotropy, that indicates the material has low anisotropy.

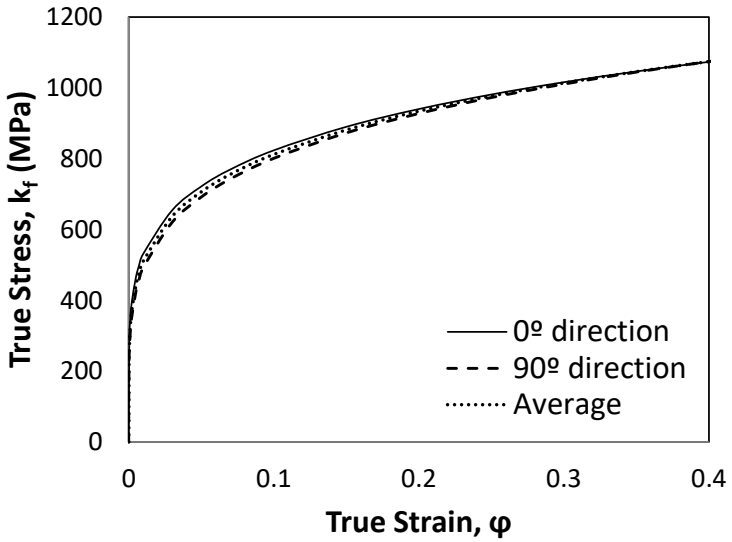

Figure 3.5: AISI 1045 flow curve in different directions. Source: SOARES (2012).

Points from the recorded data were singled out for strains ranging from 0.002 to 0.4, interval that corresponds to the occurrence of deformations in the wire drawing process (DAGNESE, 2012). The Ludwig-Hollomon Equation (Equation 3.1) for the flow curve was obtained by averaging the curves from the two different directions. This equation was then used as an input for the numerical simulations. For the given strain interval of 0.002 to 0.4 (relevant for the drawing process under investigation), Equation 3.1 may be derived:

$$k_f = 1292{,}8.\varphi^{0{,}2018} \qquad \text{Equation 3.1}$$

3.1.2.3 Friction coefficient

The ring test method is typically employed to estimate values of friction in metal forming processes due to the severe degree of deformations employed by those processes. It consists of the geometrical evaluation of steel rings during compression. As the ring height decreases due to the applied compression, the outer diameter, which deforms in the outward direction of the ring, will show a smaller increase if the friction coefficient is higher. Thus, the variation of the external diameter is a function of the height reduction. The inner diameter, on

the other hand, will present a decrease in size, as it deforms in the inward direction. Therefore, the variation of the inner diameter with respect to the height reduction (applied deformation) can be used to evaluate friction, considering a constant friction value during the deformation process (SAHIN *et al*., 2005; ROBINSON *et al.*, 2004). The ring test to evaluate the friction coefficient was used due to the high level of deformation during the wire drawing process chain.

The original dimensions of the rings, which were made from wire rod samples, were 20 mm outer diameter, 10 mm inner diameter and height of 6 mm. These rings were subjected to height reductions of approximately 20%, 40% and 60%. Three samples were compressed at each reduction. The variation of the inner diameter was recorded as a function of the height reduction. The tool used for the compression tests was made from the same material as the drawing die (a WC-Co, cemented carbide), had the same surface finishing and was covered by the same lubricant used in the manufacturing of bars (SOUZA, 2011; ROCHA, 2011; SOARES, 2012).

To determine the friction coefficient, the experimental data were plotted over calibration curves as shown in Figure 3.6, which were generated by FEM simulations of the ring test with multiple given Coulomb friction coefficients.

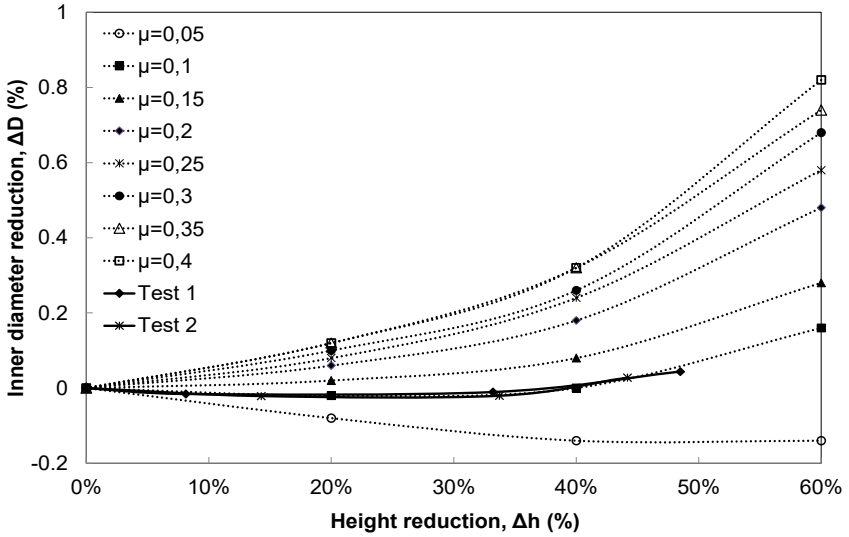

Figure 3.6: Calibration curves for the ring test. Source: (SOUZA, 2011).

The simulations were conducted in an axisymmetric two-dimensional model of the ring and tools with a 50x50 elements mesh, considering the tools as rigid and using the material's flow curve determined experimentally. Eight simulations were performed using the Simufact.Forming GP® software with a compression speed of 0.1mm/s and varying the

Coulomb friction coefficient (μ) from 0.05 to 0.4. The resulting experimental and simulation curves of the ring test are shown in Figure 3.6, where the internal diameter variation in percentage is plotted as a function of the percentage (%) of height reduction. By comparing the experimental curves with the curves obtained from simulation for different friction values, a Coulomb friction coefficient (μ) value of 0.1 was determined to be used in the combined wire drawing simulations.

3.1.2.4 Metallography

The samples for the metallographic analysis were prepared with the SiC grinding paper of mesh from 220 to 1200, with the samples being rotated 90º after each grind. This technique smooths the surface of the sample, minimizing irregularities caused by the cut. After grinding, the samples were submitted to polishing and finally to chemical attack, which lasted for 20 seconds and involved a solution of 3% alc. HNO_3.

For the metallographic analysis, samples were taken after wire rod, pre-straightening and wire drawing processes, at the peripheral 0°, 90°, 180° and 270° angular positions of the round samples and as close as possible to the surface and the center of the sample, as illustrated in Figure 3.7 (a).

In addition, samples from the vertical roller straightening and drawing processes were evaluated by Electron Backscattering Diffraction (EBSD). To analyze a sample by EBSD, a metallographic preparation of the sample must first be performed, which is paramount for the reliability of the obtained images. Three positions in two different sections, 0-180º and 90-270º, as shown in Figure 3.7 (b) and (c), were evaluated by EBSD.

Electron Backscatter Diffraction (EBSD) is a technique that provides the crystallographic information of samples in the scanning electron microscope. With this method, it is possible to analyze the crystal orientation, grain size, phase and strain, among others (DZIASZYK *et al*., 2010). EBSD requires use of a special holder to tilt the specimen 70° to the electron beam. EBSD detector comprises a phosphor screen to collect the diffracted backscattered electrons over a large solid angle, and a digital camera. Besides, the electron diffraction follows the Bragg's law.

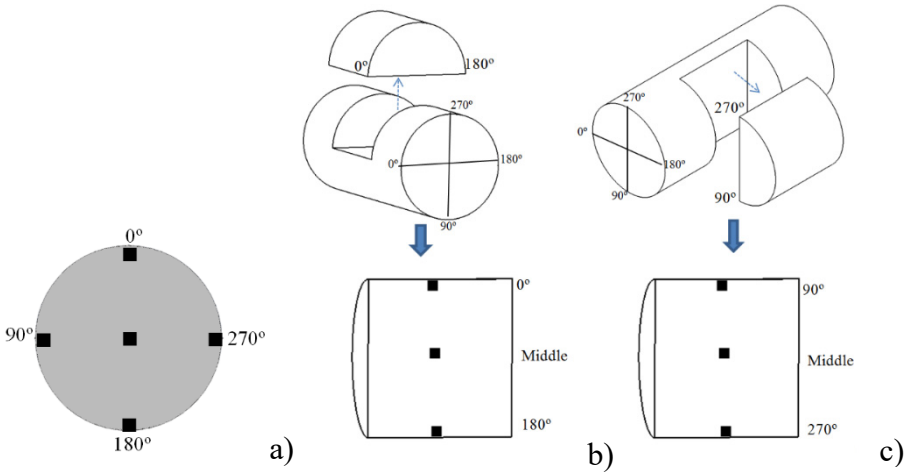

Figure 3.7: Axial measurement points in the metallographic analysis in the peripheral angular position (a) 0-180 section (b) 90-270 section (c)

3.1.2.5 Hardness

3.1.2.5.1 Microhardness

Hardness tests were carried out for peripheral angular positions in cross sections of samples collected from the wire rod, after horizontal and vertical pre-straightening and after drawing. An average of three points were analyzed for each one of the eight peripheral angular positions, which are depicted in Figure 3.8. The distance from the surface contour was determined according to the standard DIN EN ISO 6507 (2018), which states that the distance from the sample's contour should be 2.5 times the average diagonal of the indentation. The average diagonal was found to be around 160 µm, but as the surface contour of the samples was not perfectly round, this distance from the contour varied from 150 µm to 200 µm, depending on the measured point.

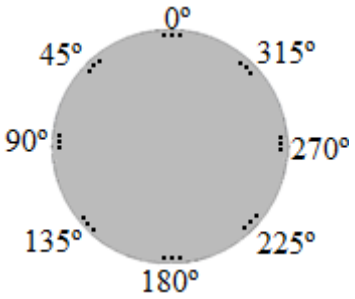

Figure 3.8: Peripheral angular measured positions for the hardness measurements.

Furthermore, measurements were performed in samples collected after all the stages in the process chain for the following positions: in the cross section, in axial direction and in the

middle, as presented in Figure 3.9. Samples from the wire rod (RM), horizontal pre-straightening (HPS), vertical pre-straightening (VPS) and wire drawing (WD) were evaluated through the Vickers hardness test with a load of 500 gf ($HV_{0.5}$). Those samples were cut in the transverse direction from 0° to 180° (Figure 3.9a) and from 90° to 270° (Figure 3.9b), where 21 indentations in each cross section were applied, 1 mm apart from each other.

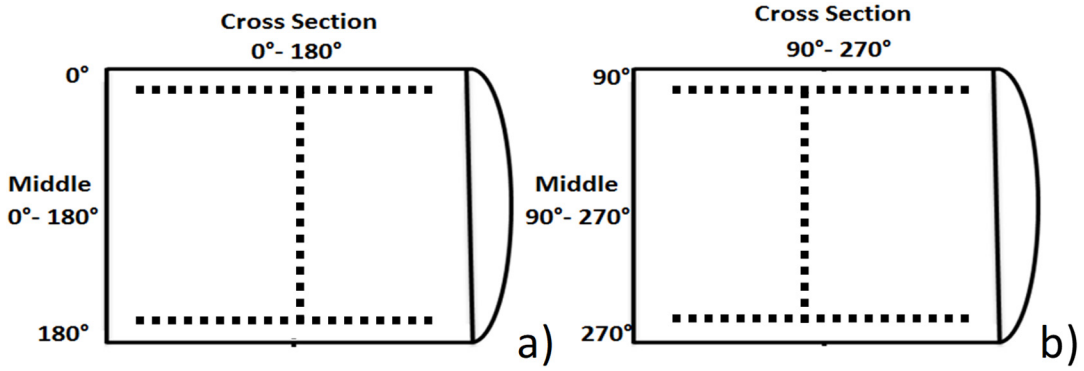

Figure 3.9: Measuring positions of Vickers hardness (HV0.5) in the cross section of the samples in 0-180 sections (a) and 90-270 section (b).

The hardness profiles were measured to be compared with the strains of the bar obtained from FEM analysis. Those results were also correlated with the full width at half maximum of the X-ray and Neutron diffraction.

3.1.2.5.2 Hardness x Strain curve

Normally, the manufacturing of cold-formed parts involves several steps before achieving in the final product. In each step, the material undergoes additional plastic strains. These plastic strains can be investigated through numerical simulations. According to Sonmez & Demir (2007), one practical way to characterize strength is through hardness, which is a measure of the level of formability of a material undergoing a cold forming process. Those two parameters can be correlated by the application of the Tabor method (TABOR, 1948), which permits the conversion of strain into hardness, previously mentioned in the theoretical background section.

In order to do so, cylindrical samples from the AISI 1045 wire rod were manufactured to be used in compression tests. Hardness profiles were measured by Vickers hardness, with the purpose of creating a calibration curve along with the strain resulting from simulation of the compression tests. Simulated strains and hardness profiles were correlated following the scheme shown in Figure 3.10. A detailed description of the method used in the simulations and the experimental procedure can be found in Zottis *et al*. (2018).

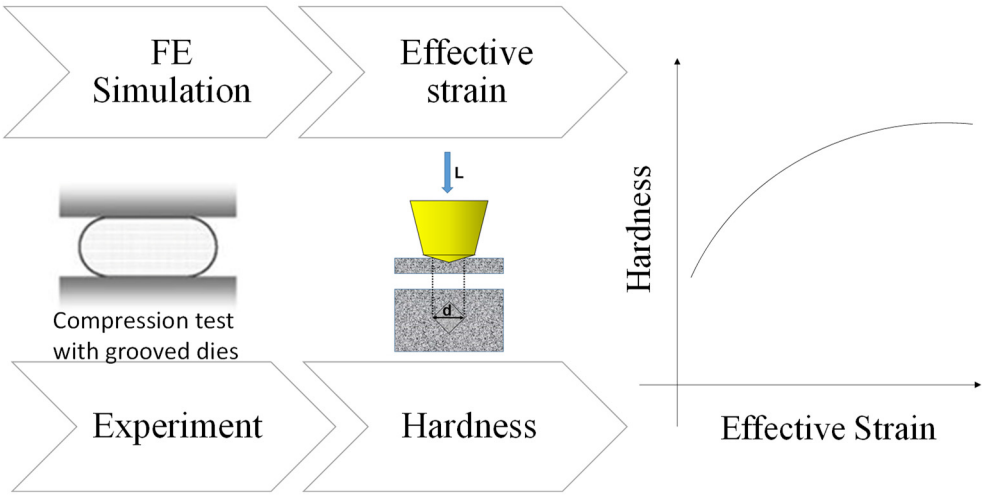

Figure 3.10: Schematic from the strain x stress calibration curve. Source: Adapted from Sonmez & Demir (2007).

The compression tests were conducted applying five different reductions (10%, 20%, 30%, 50% and 60%), and four samples were analyzed for each reduction. The samples had 10 mm diameter and 15 mm length. Subsequent to the compression test, the deformed samples were prepared for metallographic analysis so the Vickers hardness could be performed, with a load of 1 kgf, as prescribed by the ASTM E92 (2016) Standard test methods for Vickers and Knoop hardness of metallic materials. Figure 3.11 shows the hardness test scheme for the cross section (a) and for the longitudinal section (b).

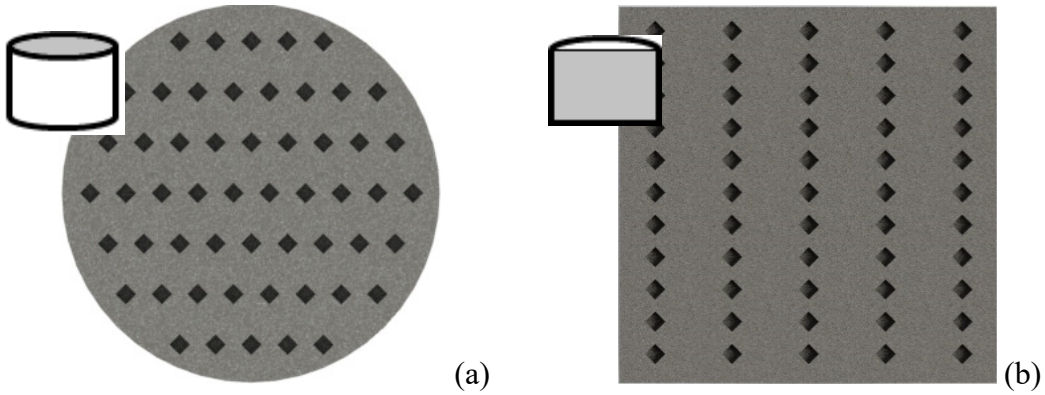

Figure 3.11: Vickers hardness measurement points in the cross-section (a) and longitudinal region (b).

In order to obtain a strain x hardness curve, the strain for each reduction from the compression tests needed to be calculated. For that, the von-Mises effective strain, shown by Equation 3.2, was employed (YU *et al.*, 2014).

$$\bar{\epsilon} = \frac{\sqrt{2}}{3}\sqrt{(\epsilon_1 - \epsilon_2)^2 + (\epsilon_2 - \epsilon_3)^2 + (\epsilon_3 - \epsilon_1)^2} \quad \text{(Equation 3.2)}$$

where ϵ_1 , ϵ_2 and ϵ_3 are the principal strains and $\bar{\epsilon}$ is the effective strain. The main strains in each direction are given by $\varepsilon_1 = \ln(h_i/h_f)$ and $\varepsilon_2 = \varepsilon_3 = \ln(d_i/d_f)$. With the measured hardness and the calculated effective strain for each reduction, it was possible to define the experimental strain x hardness curve and use it as calibration for the SAE 1045 steel. Additionally, a characteristic equation for Vickers hardness (HV) as a function of strain could be derived.

3.1.3 RESIDUAL STRESS ANALYSIS

In following subchapter, measurements of residual stresses by X-Ray diffraction and Neutrons diffraction are explained.

3.1.3.1 X-Ray diffraction

The surface residual stress was characterized by X-Ray diffraction method, for samples with 400 mm in length taken from the wire rod, after horizontal and vertical pre-straightening and after wire drawing.

The axial residual stresses were measured at eight angular peripheral locations on each sample, as shown in Figure 3.12 (a), which will be referred to as measuring circles. The residual stress measurements were performed at six measuring circles distributed along the bar at 150 mm, 170 mm, 190 mm, 210 mm, 230 mm and 250 mm from the end of each sample, as illustrated in Figure 3.12 (b).

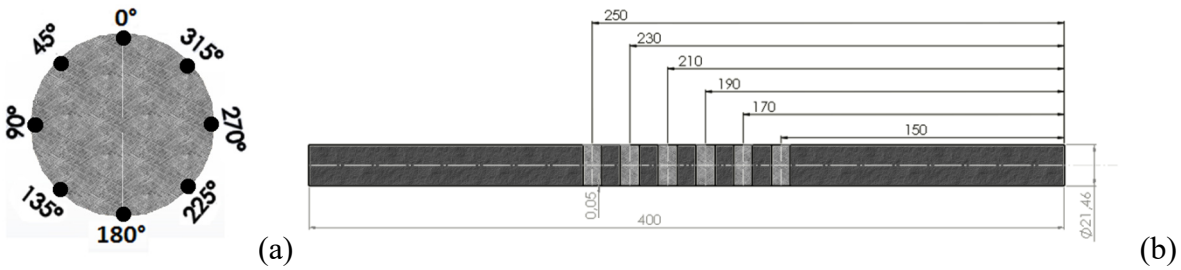

(a) (b)

Figure 3.12: Location of residual stress measurement (a) on the peripheral angular positions and (b) along the bar.

Due to the presence of an oxide layer on the surface of the samples, an electropolishing process was conducted to remove 50 µm of surface material from the samples. An electrolyte solution containing 80% H_3PO_4 (phosphoric acid) and 20% H_2SO_4 (hydrochloric acid) was utilized and total duration of the layer removal was about 30 minutes. Subsequently, the X-Ray diffraction method was used to characterize the surface's residual stresses at the mentioned measuring circles and peripheral angular positions. In addition, to examine the residual stresses along the bar's depth, another set of electropolishing to 125 µm, 250 µm, 375 µm and 500 µm in depth, limited to one measuring circle (190 mm) was performed.

For the X-Ray diffraction method, residual stresses were measured in a GE® Inspection Technologies equipment, depicted in Figure 3.13, model Analytical X-Ray MZ VI E.

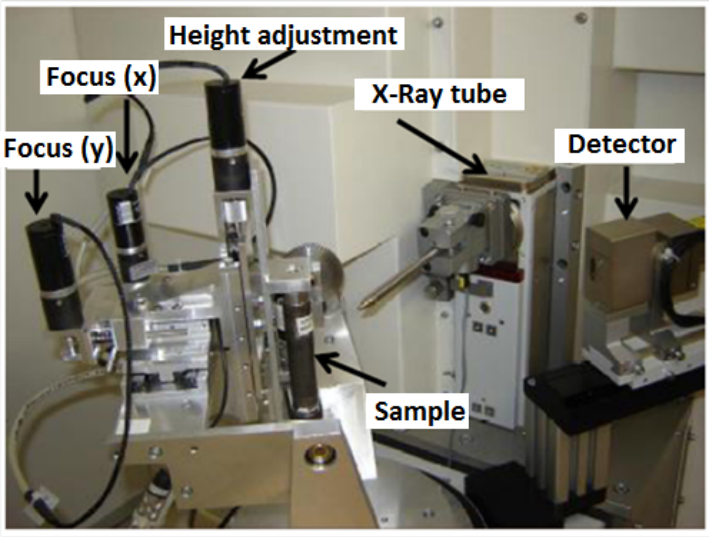

Figure 3.13: X-ray diffractometer. Source: adapted from Nunes (2012).

The residual stresses were computed using the conventional $\sin^2\psi$-method with {211} lattice planes using Cr-K_α radiation and vanadium filter. 2θ scanning was carried out from 153º to 159º. The Cr-radiation was generated by a sealed tube operated at 33 kV and 40 mA. Chi-mode with a tilt angle between +45º and -45º in eleven steps was adopted for the measurements. A collimator with a diameter of 2 mm and a Scintillation Detector were also used. The peak position was determined by the center of gravity method and with linear background correction. The penetration depth in the X-ray measurement achieve almost 6 µm using Cr-radiation for a tilt angle of 0°. A Young's Modulus of 220 GPa and a Poisson's ratio of 0.28 were adopted as the elastic constants of the iron material (KATEMI *et al*., 2014). More parameters involved in the X-ray diffraction measurements are listed in Table 3.2.

Table 3.2: Parameters used in the XRD.

Radiation	Cr-Kα
Detector	Scintillation counter
Anode Voltage	33 kV
Anode Current	40 mA
Wavelength	2.2897 Å
Background correction	Linear
Peak position determination method	Mean center of gravity
Polarization, Lorentz, Absorption corrections	Not used
Reference Peak	156.080 ({211} of the α-Fe)
Young's Modulus (E)	220 GPa
Poisson's Ratio (υ)	0.28
Measurement time	1h 58min
Angular Step	0.1°
Step time	10 s

The samples were adjusted in the X-ray diffractometer using a laser positioning system for the X and Y axis and a dial gauge for the Z axis. After the measurements, the diffraction data were evaluated with the software Analyze version 2.501 (*GE Sensing & Inspection Technologies GmbH, Ahrensburg*) to calculate the resulting residual stresses.

The values of full width at half maximum (FWHM) were also acquired by X-Ray diffraction. The FWHM is determined by the distribution of the randomly oriented lattice plane distance (HAUK, 1997) and can be used to characterize the work hardening in the material as well as the hardness measurements (NALLA *et al*., 2003). According to Hauk (1997), the FWHM may also be correlated to residual stress values and influenced by many aspects such as crystallite size and microstrains.

3.1.3.2 Neutron diffraction

In order to complement the measurements of surface residual stress by X-Ray diffraction, Neutron diffraction was used in the cross section of the bar. This technique is quite efficient for the measurement of residual stress in the core of samples, as it can reach depths

that the X-Ray diffraction technique cannot, permitting a residual stress profile to be captured from near surface to the center of the bar without cutting the sample (FITZPATRICK, 2005).

The Neutron diffraction measurements were conducted in the Neutron strain measuring instrument E3 in the beam line of the research reactor BER II of the Neutron Scattering counter at the *Helmholtz-Zentrum Berlin*, Germany. The diffractometer is an angular dispersive type, where neutrons are separated by a steady-state reactor source. A single wavelength of 1.486 Angstroms was obtained by a Si (400) double focusing monochromator from the polychromatic neutrons produced by the reactor (WIMPORY & BOIN, 2011). For the determination of the stress-free lattice parameter, $d_{0,hkl}$, a cube of size 3 x 3 x 3 mm was cut by wire electrical discharge machine (EDM) from the sample material. The gauge volume (27 mm^3) was measured in different Omega angular values.

The {211} diffraction line of alpha iron was selected for the measurements. The peak position was around 77.8°. For the analysis of the diffraction pattern, the Software Stresstex developed by C. Randau of FRMII/TUM has been used (EPP *et al*., 2010b).

In Neutron diffraction, the interplanar distance of a given plan to the axial, hoop and radial directions in the horizontal pre-straightened samples were measured at the middle of the bar on the section corresponding to 90°-270º, according to Figure 3.14a. The vertical pre-straightened sample was measured in two sections, from 90º to 270º and from 0º to 180º, as shown in Figure 3.14b. Both horizontal and vertical pre-straightened samples were measured at the surface at 200 mm from the bar end. The angular positions were defined by the "right-hand rule", according to which the right thumb should be pointed to the process direction.

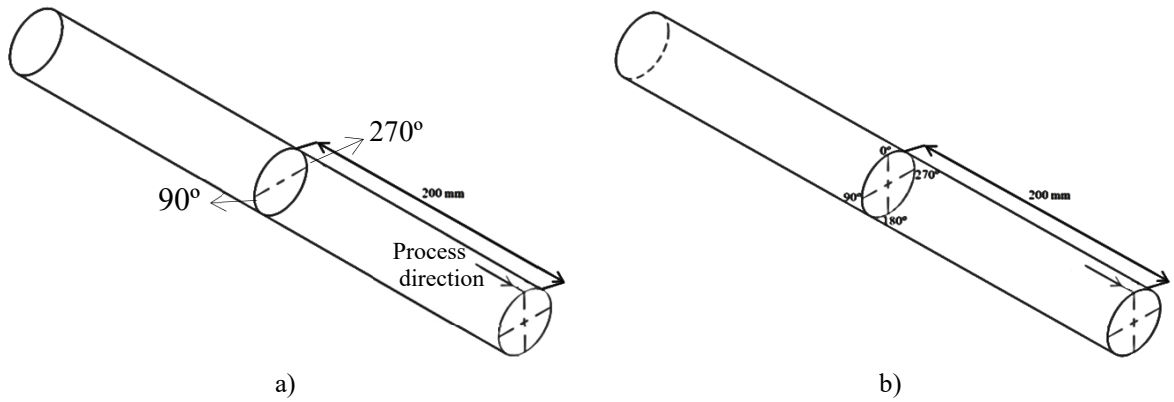

a) b)

Figure 3.14: Residual stresses measurement by Neutron diffraction in (a) horizontal pre-straightening sample (line from 90º to 270º) and vertical pre-straightening sample (lines from 0º to 180º and from 90º to 270º).

The basis of neutron diffraction is the measurement of lattice spacing through diffraction peak positions (2θ). From this information, the interplanar distance can be calculated by the

Bragg's law, as explained in the section 2.4, residual stresses. With the interplanar distance, the strains can be calculated and finally the residual stresses can be determined for the three principal directions using the elastic constants of the material, i.e. Young's modulus and Poisson's ratio.

The balance of residual stresses was checked against the measured values, since the accuracy of measurements taken with Neutron diffraction depends on the precision of the interplanar distance d_o determined without the action of residual stresses (HAUK, 1997). The results of these measurements were thereby compared to the stresses obtained with numerical simulation.

3.2 NUMERICAL SIMULATION

In this work, the resource of numerical analysis using the software ABAQUS CAE was utilized with the purpose of aiding the understanding of the equipment currently employed in pre-straightening, as well as of the development of residual stresses in the bar during and posterior to the process chain. Here, the arrangement of the rolls set was modified in order to produce the best straightened bar, with a more homogeneous profile of strains and a good balance of residual stresses in the peripheral angular position of the bar.

The distribution of residual stresses along the length of drawn products is also not completely understood currently, as it is affected by small variations during or prior to the process. These variations contribute to the distortion of these products. Employing simulation, it becomes possible to examine the generation of residual stresses along the bar as a whole, as opposed to localized to a point or strict to a portion of the bar as it is the case when experimental measurements are applied.

In this chapter, the methodology involved in the simulation process will be presented, focusing on the configuration adopted for the models that were developed to reproduce the pre-straightening and wire drawing processes done in reality. However, models that received different parameters for the horizontal step of pre-straightening and their resulting bars after wire drawing will be presented in section 6, as a proposed improvement to the process. The numerical analysis were divided into two stages, as illustrated in Figure 3.15, namely:

1) Simulation of the pre-straightening process and wire drawing with parameters set to reproduce the actual process, followed by evaluation of the residual stress profile.

2) Simulation of the pre-straightening process and wire drawing with two proposed modifications in the rolls' arrangement of the horizontal pre-straightening process, in order to improve the residual stress profile.

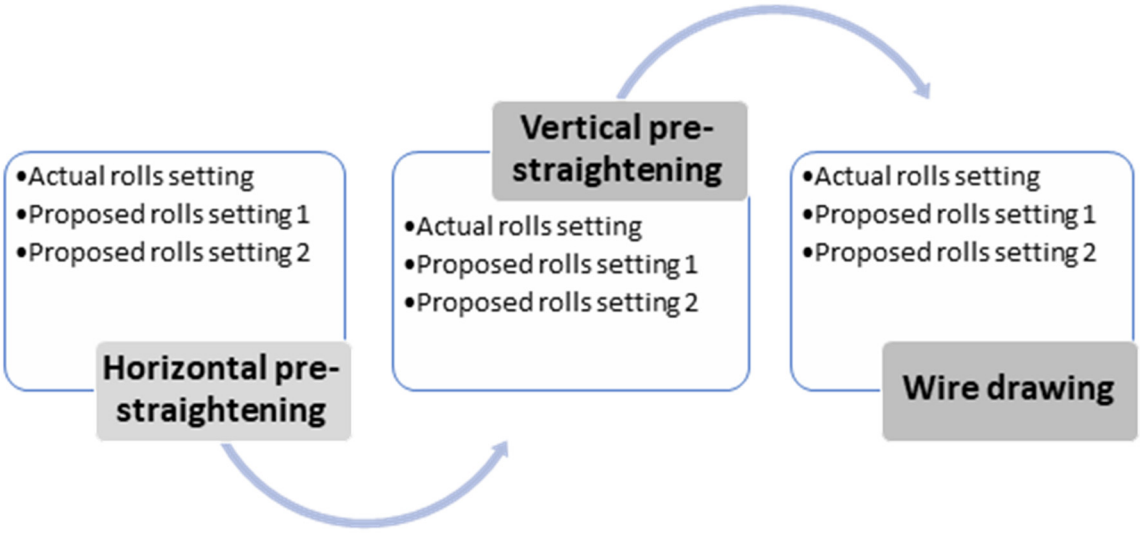

Figure 3.15: Stages of the numerical simulations performed.

3.2.1 Simulation parameters

3.2.1.1 Mesh

To ensure the accuracy of the simulation results, it is necessary to first examine the mesh to be selected for the model regarded to type and size. For the process chain model, the mesh generation begins with a 2-D sketch, followed by an extrapolation into hexahedral elements through expansion along a curve with the shape of the bar. This procedure is required in order to achieve a final hexahedral mesh that provides realistic residual stresses in a curved bar. The final mesh is depicted in Figure 3.16.

Mesh convergence, mesh size and element type were investigated prior to definition, so satisfactory results could be achieved along with a suitable computational time requirement for the residual stress analysis in the process chain. As a result, the mesh size was created with 2 mm in diameter and 4 mm in length, using the C3D8R element (element type with 8-node linear brick, reduced integration) and neglecting remeshing criteria. This kind of element possesses

hourglass control, which prevents the elements from having only one integration point. Therewith, the element will not distort in such a way that would lead all the strains calculated at the integration point to be equal to zero, which would implicate an uncontrolled distortion of the mesh (ABAQUS, 2013). The modelling decision to neglect remeshing was previously validated by a wire drawing simulation, as no differences were found in the results between the simulations considering remeshing and without remeshing.

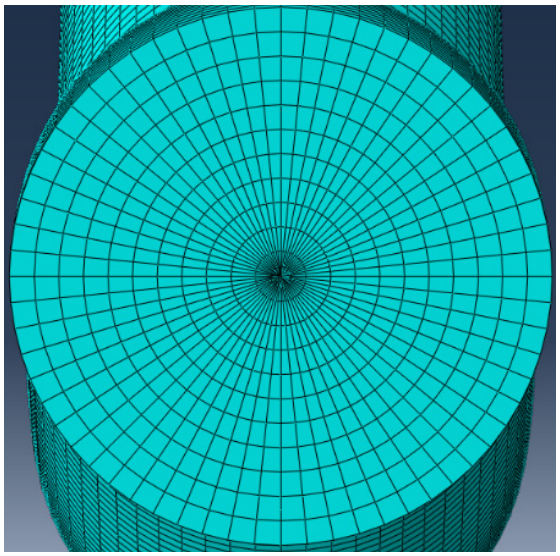

Figure 3.16: Mesh with C3D8R elements (hex. mesh)

3.2.1.2 Model of the raw material

The wire drawing process chain is conducted with coiled wire rod, which gives to the bar a curved shape. To determine the parameters of the wire rod's curvature, a 3-D laser scanner was employed. The scanner application is scanning finished products, either complex or not.

Following the process chain, the wires are cut into bars of 6 m in length. Then, each bar is cut into smaller samples of about 400 mm in length, which keep the initial curved shape of the wire rod obtained by 3-D scanning. The scanner generates a points' cloud that must be converted into a surface, so the bar can be fed in the model in ABAQUS CAE. The final solid bar is shown in Figure 3.17.

The length of the samples were 353 mm, 348 mm and 367 mm, from the wires 1, 2 and 3, respectively. The three samples were assembled in the software SolidWorks, where their corresponding curvatures were determined. Thereby, a model considering the actual curvature

of the wire rods could be developed and used as input for the simulations before entering in the horizontal pre-straightening process. In addition, the diameter of the bar was measured using a micrometer on six residual stresses measurement points on four peripheral angular positions to evaluate the variation of the diameter along the length of the bar.

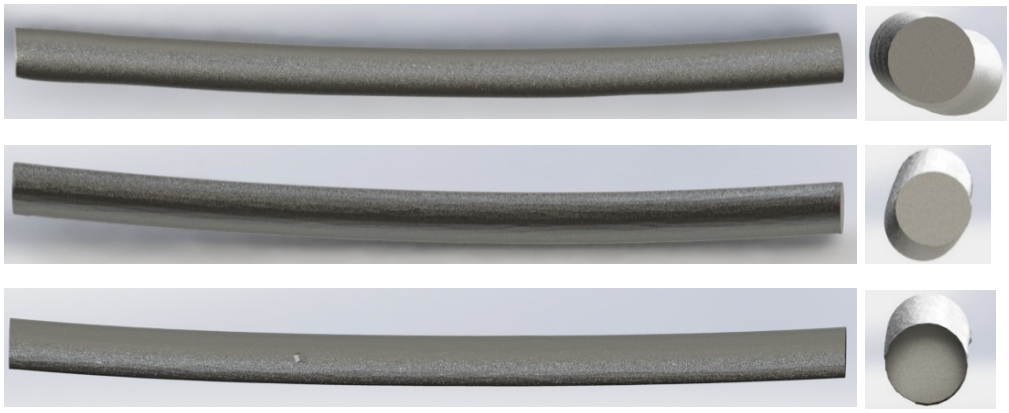

(a)

(b)

(c)

Figure 3.17: Front and side view of wire road, (a) wire 1, (b) wire 2 and (c) wire 3

3.2.1.3 Material and contact interaction

The material defined for the numerical analysis was the AISI 1045 steel, which is widely used in the industrial manufacturing of shafts. This steel is classified as medium carbon, has good mechanical properties, toughness, good machinability and weldability when hot-rolled or normalized, and contains the chemical composition presented in Table 3.1.

The material density is 7860 kg/m^3. Mass scaling was employed to reduce the calculation time. The rollers were generated with analytical rigid surface. The bar's material model was defined as elastoplastic with a yield stress of 369 MPa which was run in a dynamic explicit simulation. The kinematic hardening effect and Bauschinger effect were not considered. The anisotropy indices, which were based on previous work (DIAS *et al.*, 2014; SOARES, 2012), the flow curve and the friction coefficient considered in the analysis are presented in Table 3.3.

Mechanical contact interactions were established by tangential behavior with a general contact between the rigid tool and the deformable bar. The surface-to-surface contact prevents undetected penetration of master nodes into the slave surface to occur. Heat transfer between the deformable bar and the rigid die was not considered. A Coulomb friction coefficient of 0.1

between the rollers and the bar, as well as between the bar and the die, was used. This coefficient was based on the data obtained experimentally through ring tests by de Souza (2011).

Table 3.3: Material properties from AISI 1045 (DIAS et al., 2014).

Property	**Value**
Material	AISI-1045
Young's Modulus (E)	210 GPa
Poisson's ratio (υ)	0.3
Yield point (k_{f0})	368.87 MPa
Flow Curve	$k_f = 1292.8.\phi^{0.2018}$
Shear Modulus	80.77 GPa
Anisotropy indices (F, G, H)	0.634; 0.424; 0.424
Anisotropy indices (L, M, N)	0.5; 0.692; 0.692

3.2.2 Modelling of the actual process

The numerical analysis begins with a meticulous evaluation of the actual process that is to be emulated. The curvature of the wire rod was obtained by previous evaluation of the samples by 3-D scanning and, to better reproduce the results from the experimental tests, the bar was defined to cross simultaneously the two straightening processes and the wire drawing process, so its length was set as 3 m.

A wire rod with lenght of 800 mm was selected. This wire rod was collected from the coil starting at a distance of 1250 mm, as indicated in Figure 3.18a.

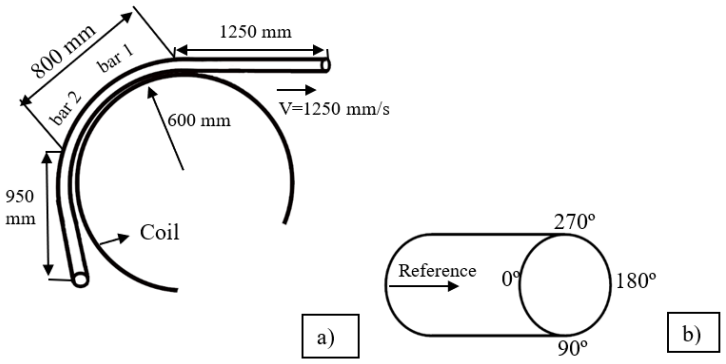

Figure 3.18: Top view of the bar geometry (a) and reference position (b)

In other words, just a part of the bar was used, corresponding to a middle length, where a stationary state has been reached in order to avoid effects from the puller and from near the end of the bar. Furthermore, the wire rods with 800 mm were divided into two small pieces of 400 mm (named bar 1 and bar 2). Figure 3.18b shows reference positions used to analyze the results.

A CAD model, which can be seen in Figure 3.19, was developed using parameters from the real process and considering the group components presented in Figure 3.2. Figure 3.19a shows the directions of the motion in the horizontal step and the position of the process in the chain.

The wire rod (Ø21.46 mm) is uncoiled and pulled out in a velocity of 1250 mm/s. The coil has a diameter of 1200 mm, thereby, the wire rod has the geometry of the coil. After uncoiling, the wire rod passes through two guide rolls (Ø250 mm). The next step is the horizontal pre-straightening, which is composed by a set of six rolls of Ø230 mm each, as shown in Figure 3.19b. The second pre-straightening process is the vertical, consisting of a set of five rolls with Ø192 mm (Figure 3.19b). The model in Figure 3.19b is presented from a view angle that better displays the shape of the wire rod. The real placement of the horizontal and vertical roll can be seen in Figure 3.19a.

The six straightener rolls from the horizontal process were placed according to the dimensions and distances of the experimental process and as illustrated in Figure 3.20a. The A, B and C values from Figure 3.20a will be altered in the simulation of a proposed improvement to the process. The movement of the rolls is controlled by the distance between the central axes of the pairs formed between the upper and lower rolls, which ranges from 230 mm to 280 mm and is represented by the diagonal *D* in Figure 3.20b. Therewith, the A, B and C values should respect this range. The variation of these distances was investigated, along with the distance between the central axis of each roll in the longitudinal direction, because it is believed that all of them have a significant influence on the profile, shape and intensity of the residual stresses that remain in the bar after drawing.

Due to the curvature that remains after the horizontal pre-straightening, the use of the vertical pre-straightening, presented in Figure 3.21, is also necessary. This process is performed by a set of five straightener rolls of Ø190 mm positioned with 90° angular variation in relation to the horizontal process central line. The simulation model reproduced the same arrangement of the rollers as that of the real case.

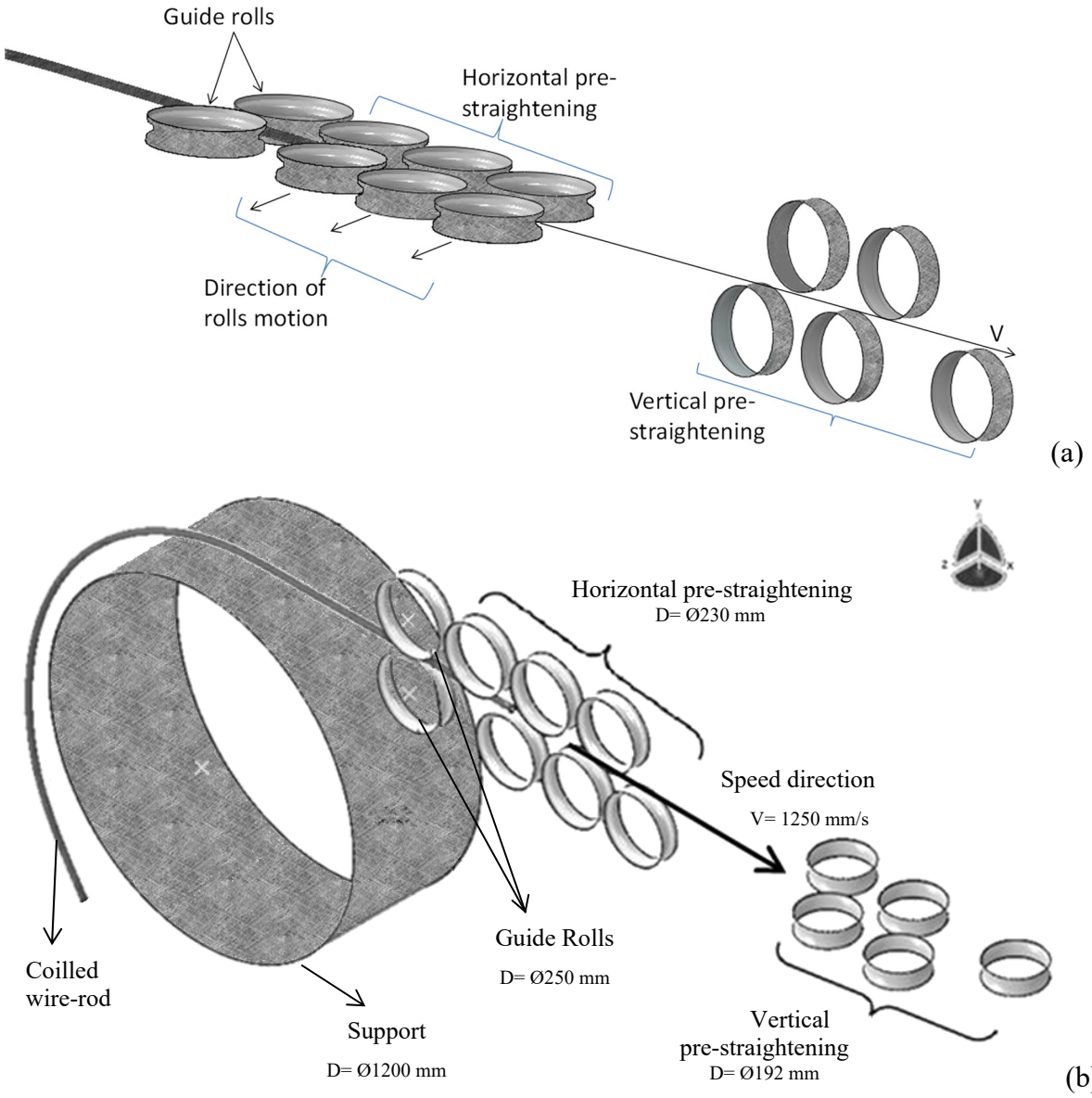

Figure 3.19: Direction of the rolls' motion in the real composition of the straightening (a) and the developed model for the simulation with the rolls dimensions (b).

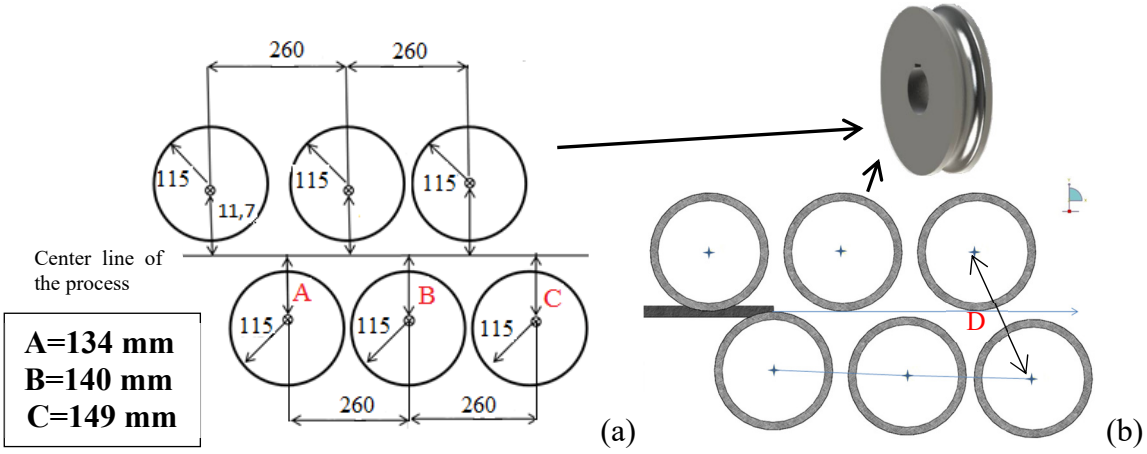

Figure 3.20: Dimensions of the pre-straightening process (a) and straightener roll (b).

When simulating multiple processes, it becomes essential that the outcome from one process analysis be carried to the analysis of next process. Therefore, the bar in the vertical pre-straightening simulation should include all the resulting parameters, such as residual stresses and final shape, from the horizontal pre-straightening model analysis.

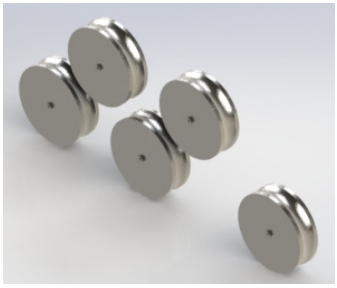

Figure 3.21: Vertical pre-straightening

After the straightening rolls, the wire rod continues to be drawing. Prior to the drawing process, the wire is shot blasted. However, this process is not considered in the simulations presented since. During the drawing process, the wire diameter undergoes an 11% reduction, reaching Ø20.25 mm. The wire drawing is performed by a tool of W-Co named die, which is encapsulated in an AISI 1045 steel (Figure 3.22a).

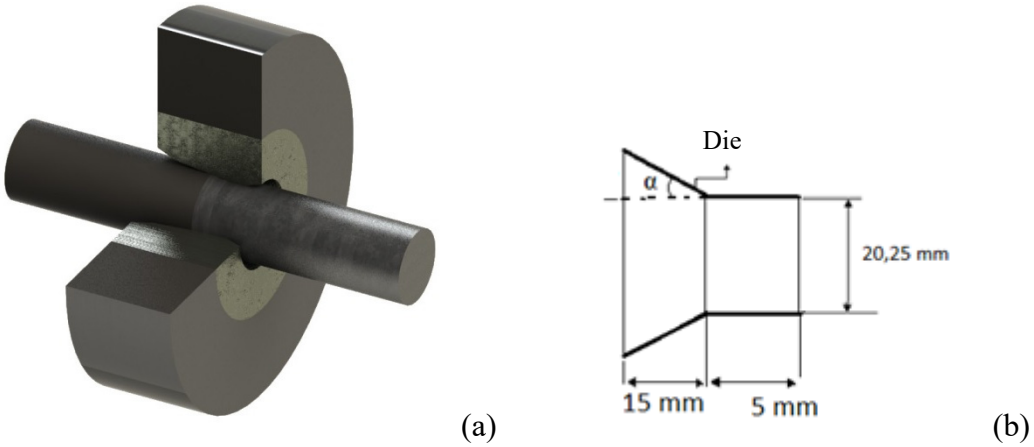

Figure 3.22: Wire drawing tool (a) and the tool dimensions (b).

The wire drawing step in the process chain was evaluated by Nunes (2012), where two die angles were studied: 15 degrees and 20 degrees. For the simulations in this project, the evaluated angle (Figure 3.22b) was 15 degrees ($\alpha = 7.5^{o}$), as to follow previous results obtained by the BRAGECRIM project. Due to the influence of the pre-straightening parameters, a computational model combining the vertical and horizontal pre-straightening processes

together with wire drawing process had to be developed. The results from one process were transfered to next one in order to reduce the processing time and to maintain the memory state of results of each process.

3.2.3 Rolls settings for processing improvement

Following an assessment of the process chain with pre-straightening rolls positioned as indicated in Figure 3.20b, two additional layouts were evaluated using simulation of the horizontal pre-straightening process due to the level of deformations of the horizontal process be higher than the level of deformations caused by the vertical process. Settings 1 and 2 were selected from multiple layouts that were simulated and evaluated in terms of residual stresses and bar shape at the end of the wire drawing process.

Figure 3.23 illustrates proposed Setting 1, which is opposite to the original position of the rolls. Figure 3.23 (b) presents the dimension of the rolls and the distances adopted between rolls in Setting 1.

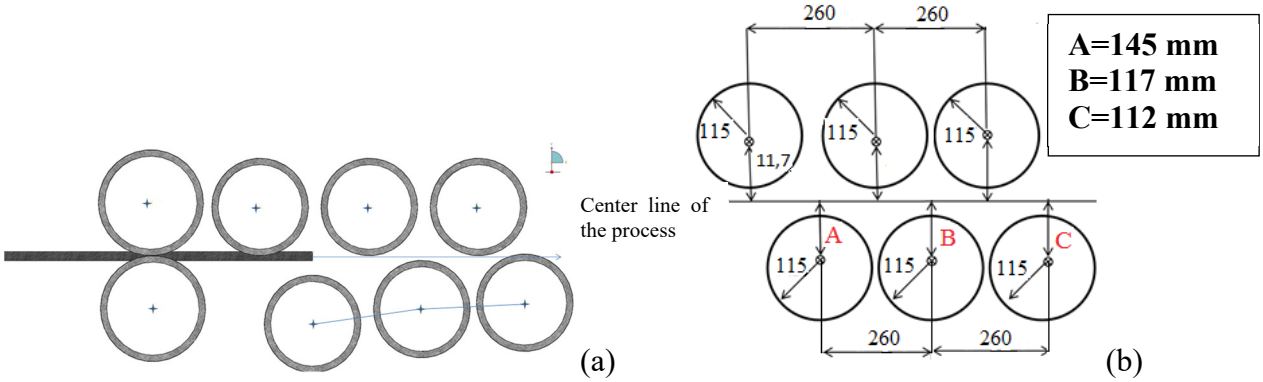

Figure 3.23: Setting 1: (a) new rolls layout and (b) dimension of the rolls and distances adopted between rolls.

Figure 3.24 (a) illustrates the arrangement of Setting 2, which was defined with intermediate dimensions between the original layout of rolls set and Setting 1. Figure 3.24 (b) shows the dimensions of the rolls and the distances adopted between the rolls. Note that the parameters that were altered correspond to that represented by A, B and C in Figure 3.24 (b). Simulation of the horizontal process was followed by the development of new models for the vertical and wire drawing processes, which maintained their original configuration and were just altered with respect to the horizontal process.

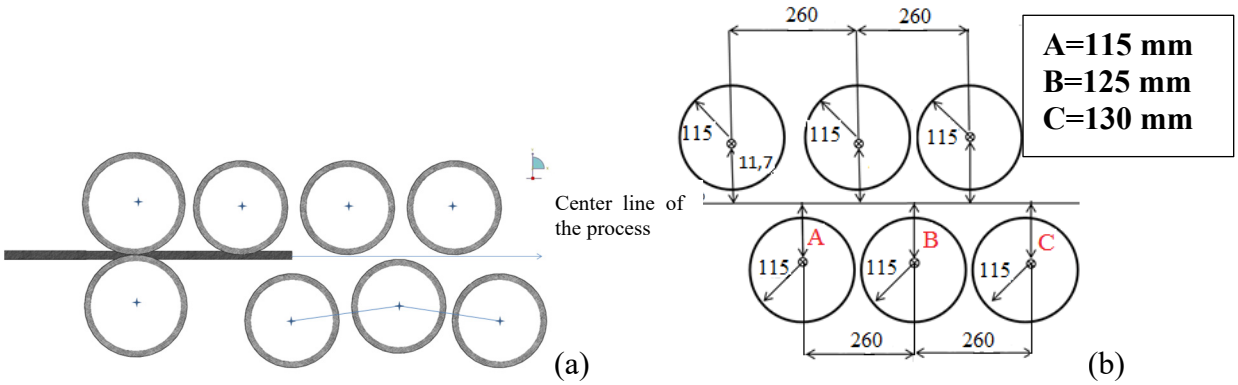

Figure 3.24: Setting 2: (a) new rolls layout and (b) dimension of the rolls and distances adopted between rolls

4 RESULTS

In this chapter, the results from the experimental measurements and simulations are presented in detail.

4.1 EXPERIMENTAL RESULTS

The experimental results are showed in this section, following the order of occurrence in the process chain. First, results obtained by metallography, hardness and X-Ray diffraction of the raw material samples are presented. In the sequence, results of the horizontal pre-straightening, vertical pre-straightening and wire drawing samples are shown. Finally, the aforementioned results are discussed.

4.1.1 Raw material

4.1.1.1 Microhardness and metallographic analysis

Figure 4.1 illustrates the Vickers microhardness distribution of the raw material, together with full width at half maximum (FWHM) measured by X-Ray diffraction at eight peripheral angular positions.

The hardness value corresponding to the angular position 0º/360º is equal to 188 $HV_{0.5}$, representing a deviation from the remaining angles, in which hardness is almost constant at 220 $HV_{0.5}$. Hardness at the 0º angular position was found to be 15% lower than that of the other seven measured angles as shown in Figure 4.1. The cold working of the raw material is due to the rolling of the manufacturing process and, for this reason, the FWHM has small variation among the angular positions of the raw material, ranging between 1.46º and 1.6º.

Micrographs from the center of two distinct sections of the raw material samples are shown in Figure 4.3. The displayed microstructure is composed of pearlite (dark areas) and ferrite (white areas). The raw material was found to have a banded microstructure, which is caused by the rolling process to which the raw material is submitted during the manufacturing process.

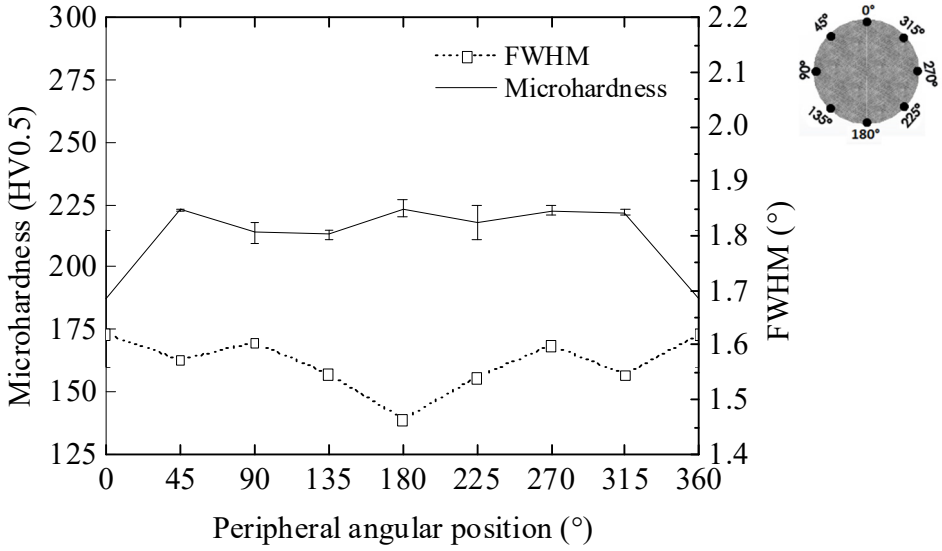

Figure 4.1: Microhardness and FWHM in the peripheral angular positions of the raw material

There are small variations of microhardness at the peripheral positions along an axial distance of 10 mm as shown in Figure 4.2. The maximum difference in the microhardness values is 25 HV0.5.

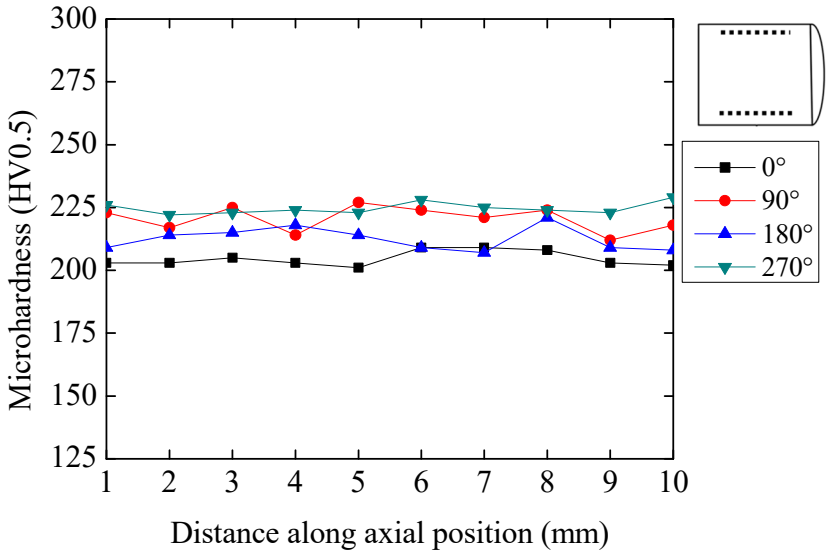

Figure 4.2: Hardness in the section 0º-180º and 90º-270º sections of the raw material.

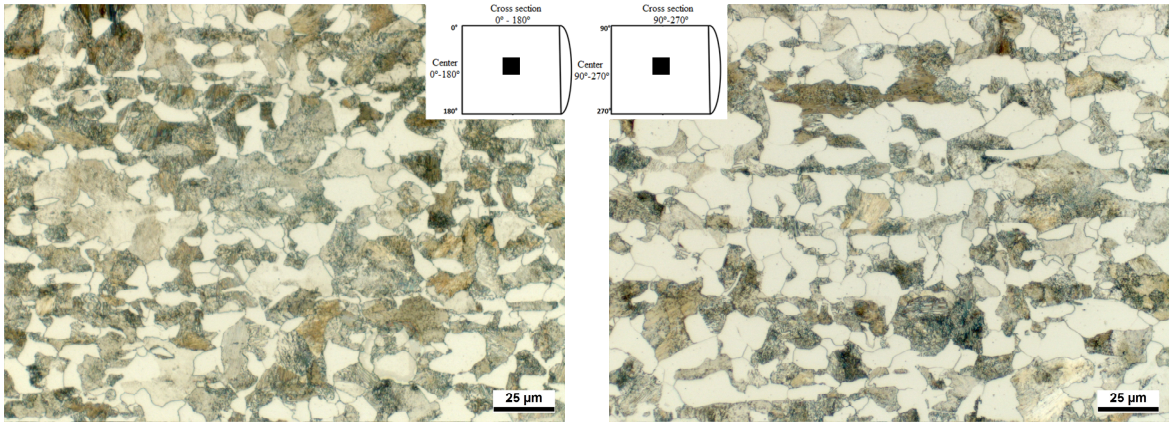

(a) (b)

Figure 4.3: Microstructure of the raw material in the center of (a) 0-180º and (b) 90-270º setion

4.1.1.2 Residual stresses in the raw material

Residual stresses are generated during the process of rolling and coiling to which the raw material is submitted in the final stages of the manufacturing process.

In Figure 4.4, the surface axial residual stresses, measured by X-Ray diffraction in the raw material with the removal of a 50 µm-thick layer, and the full width at half maximum – FWHM, are shown. The residual stresses were measured before the bar entering in the horizontal pre-straightening process.

As it can be observed in Figure 4.4 (a), the raw material experiences compressive residual stresses at the 90° position and tensile residual stresses at the 270° position. This asymmetry can be attributed to the strains arising from the shape of the raw material gained under the influence of the original coil's curvature, which implicates in the generation of residual stresses.

As exposed in Figure 4.4 (a), compressive residual stresses with values around -150 MPa are present at the angular positions ranging from 0° to 180°, whereas angular positions from 225° to 315° exhibit tensile stresses of around 100 MPa. The values of FWHM, plotted in Figure 4.4 (b), vary between 1.46° and 1.64°.

Axial surface residual stress profiles are illustrated in Figure 4.5 including multiple angular positions at two distinct distances from end of the bar, 150 mm (Figure 4.5 (a)) and 250 mm (Figure 4.5 (b)), and in six different depths, from 0 µm to 500 µm. The profiles at the two distinct distances have shown similar maximum and minimum values of residual stresses.

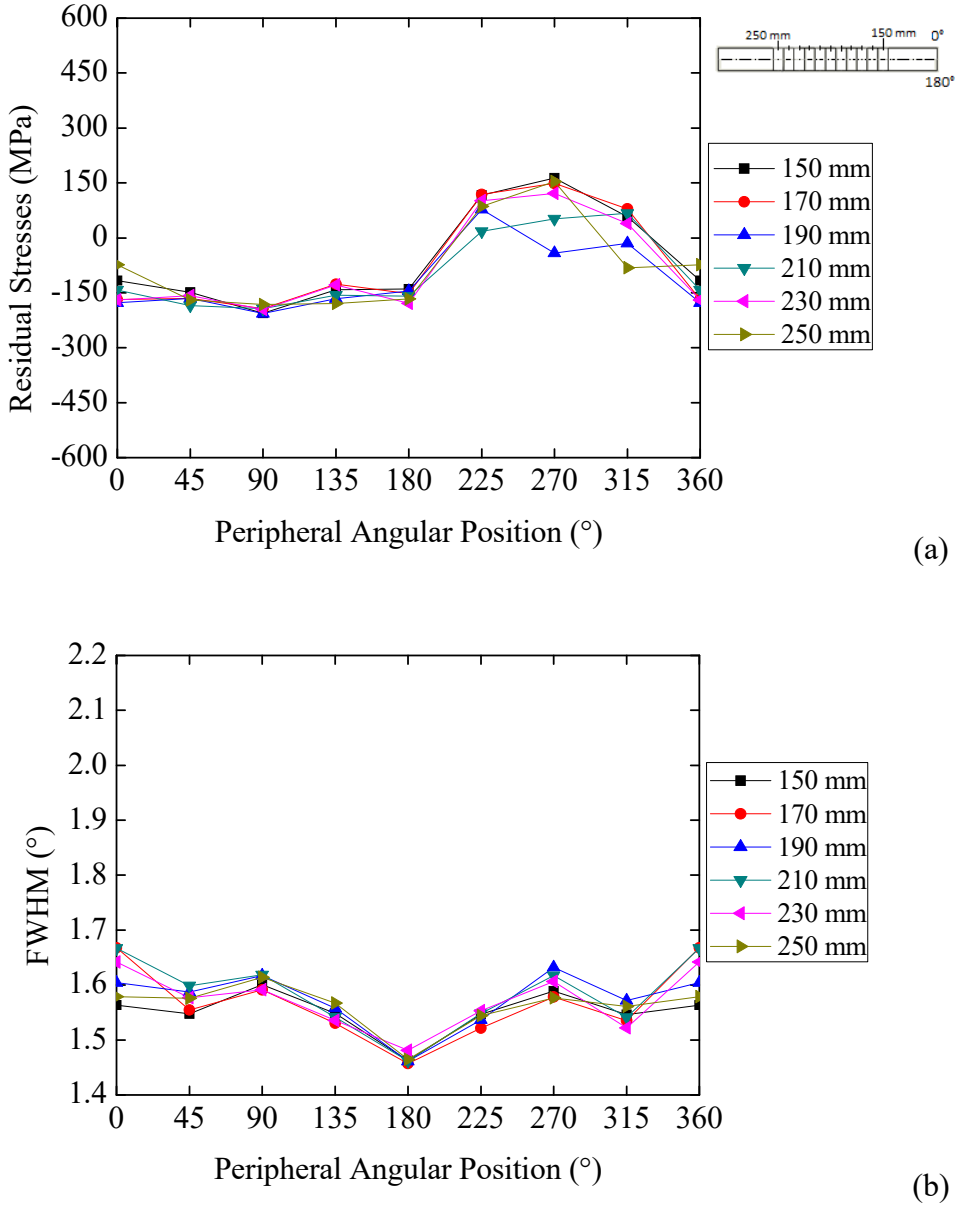

Figure 4.4: Residual Stresses on the surface of the raw material with 50 µm etching (a) and FWHM (b) for distances from 150 to 250 mm from end of the bar.

Residual stresses in 0 µm are compressive at all peripheral positions and at both distances from end (Figure 4.5). Beyond the depth of 50 µm, residual stresses become tensile at the peripheral positions of 225º and 270º, with a maximum tensile value of 200 MPa corresponding to the angle of 270º. On the other hand, the residual stress profile has a compressive behavior at the peripheral angles of 0º, 45º, 90º and 135º in every depth evaluated, with minimum compressive value of -200 MPa at the peripheral angle of 90º. The residual stress profiles exhibit unsteady behavior at the peripheral angles of 0º and 180º in all measured depths. This unsteady behavior can be due to the coiling process or the geometry of the raw material.

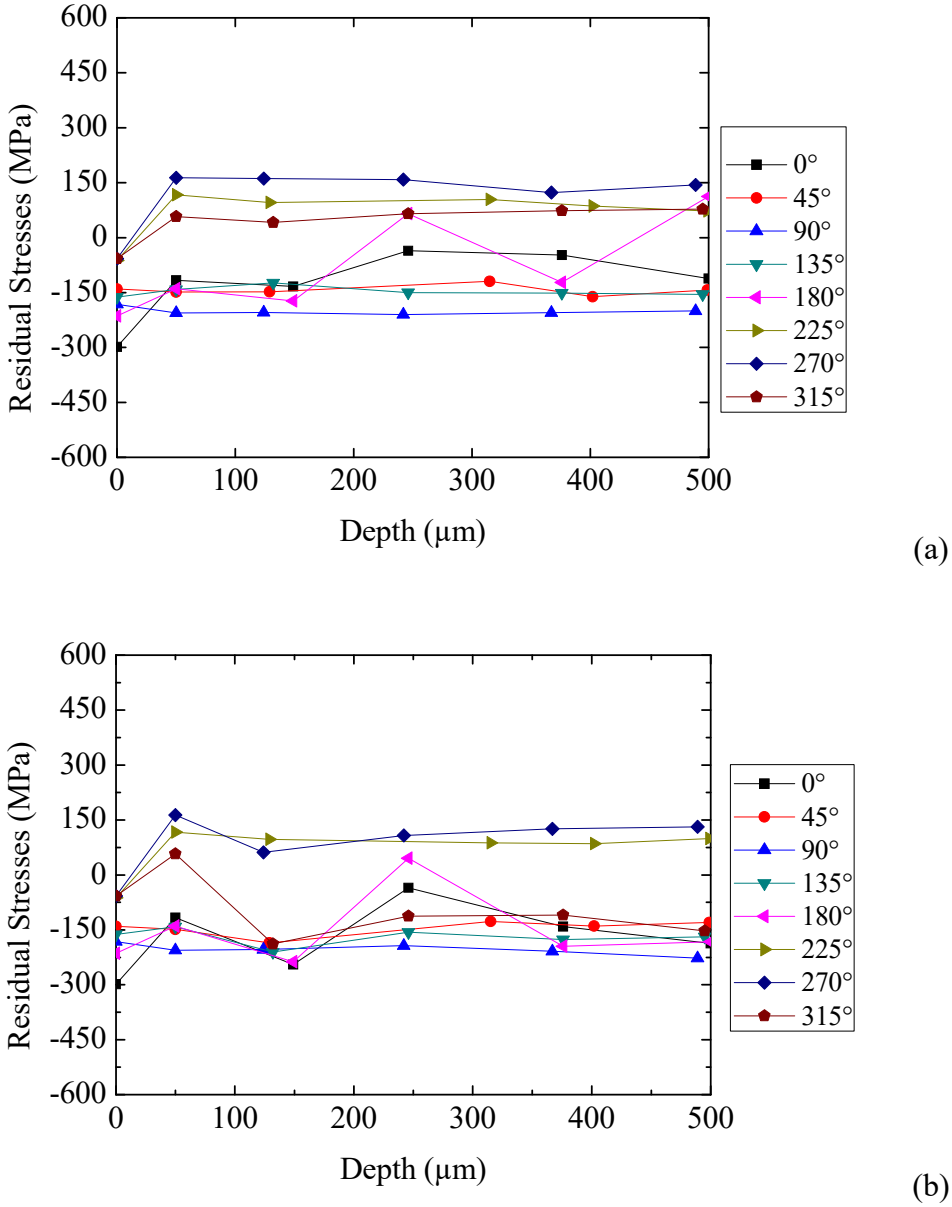

Figure 4.5: Raw material: residual stresses in terms of depth at (a) 150 mm and (b) 250 mm axial positions.

4.1.2 Horizontal pre-straightening

4.1.2.1 Microhardness and metallographic analysis

Hardness and FWHM measured at the peripheral angular positions of samples from the horizontal pre-straightening process are shown in Figure 4.6. The maximum hardness value (260 $HV_{0.5}$) corresponds to the 90º angular position, while the minimum hardness value (216 $HV_{0.5}$) is observed at the 180º position. FWHM peaks coincide with hardness peaks, as the maximum FWHM value (about 1.82º) was recorded at the 90º position and the minimum

(almost 1.55º) corresponded to the 0º. Samples from the raw material (Figure 4.1) experienced lower values of both hardness and FWHM compared to the samples from horizontal pre-straightening (Figure 4.6).

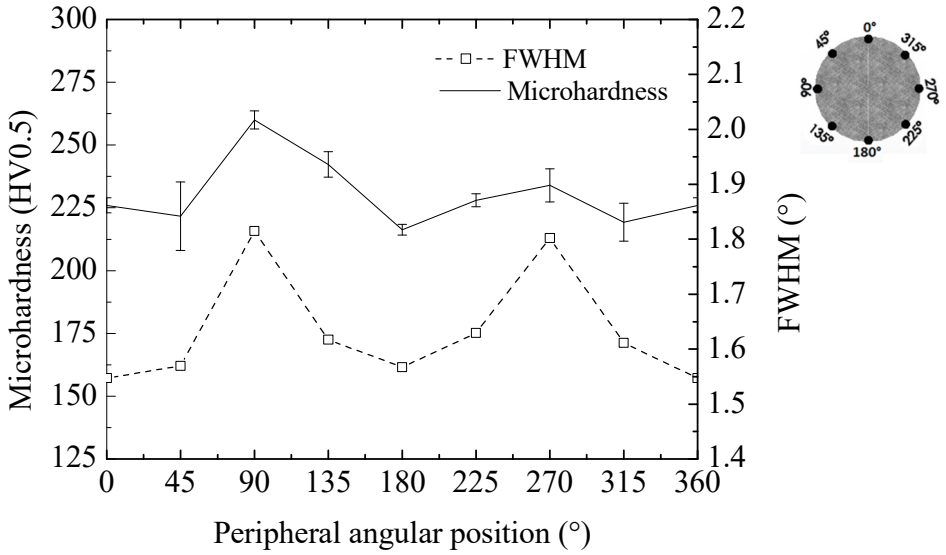

Figure 4.6: Hardness and FWHM at the peripheral angular positions of the horizontal pre-straightening bar.

Figure 4.7 show the micrographs of the horizontal pre-straightened bar at the angular positions of (a) 90º and (b) 270º. The micrographs show a homogeneous pearlitic and ferritic microstructure with a grain size slightly larger at the angular position 90º.

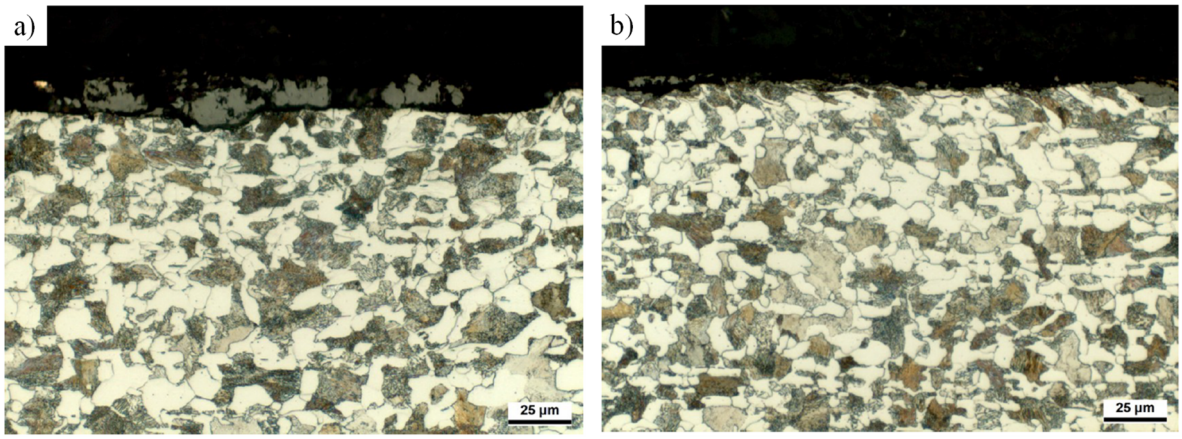

Figure 4.7: Micrograph of the horizontal pre-straightening bar at the angular positions (a) 90º and (b) 270º.

4.1.2.2 Residual stresses after horizontal pre-straightening

Residual stresses measured on the surface of samples from horizontal pre-straightening are plotted in Figure 4.8. The observed behavior of residual stresses diverges from the results in the raw material, previously presented in Figure 4.4.

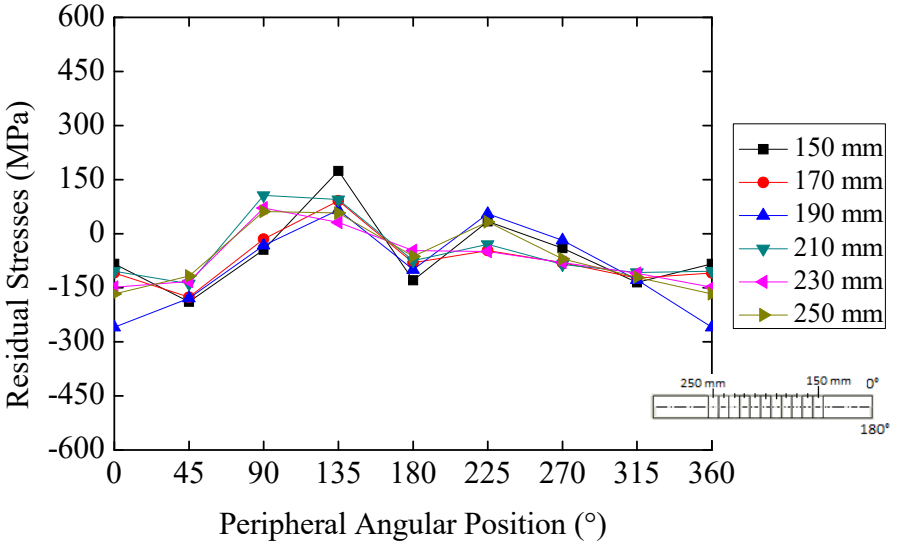

(a)

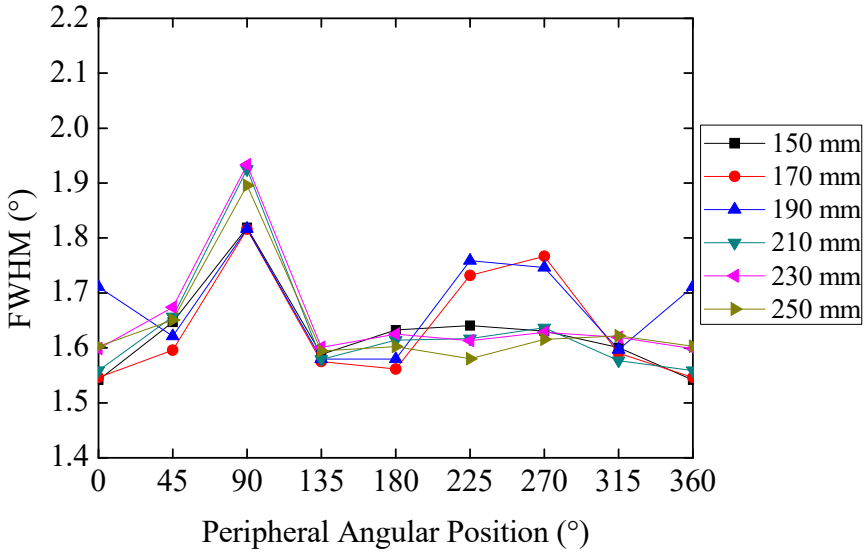

(b)

Figure 4.8: Residual Stresses on the surface of samples from the horizontal pre-straightening with 50 µm etching (a) and FWHM (b) for distances from 150 to 250 mm from end of the bar.

Figure 4.8 (a) shows that minimum and maximum values of residual stress are equal to -250 MPa and 180 MPa, respectively. The profile of residual stress exhibits a change, including the turn of compressive stresses illustrated in Figure 4.4 from raw material into tensile stresses presented in Figure 4.8 from horizontal pre-straightening at the 90º and 135º angular positions.

Comparing FWHM values obtained from samples taken after horizontal pre-straightening with that from the raw material, an increase in FWHM is noticeable at the 90º and the 270º positions, which correspond to the points where the pre-straightening rolls have contact with the bar. At these positions, FWHM reaches up to 1.9º compared with 1.6º in other regions.

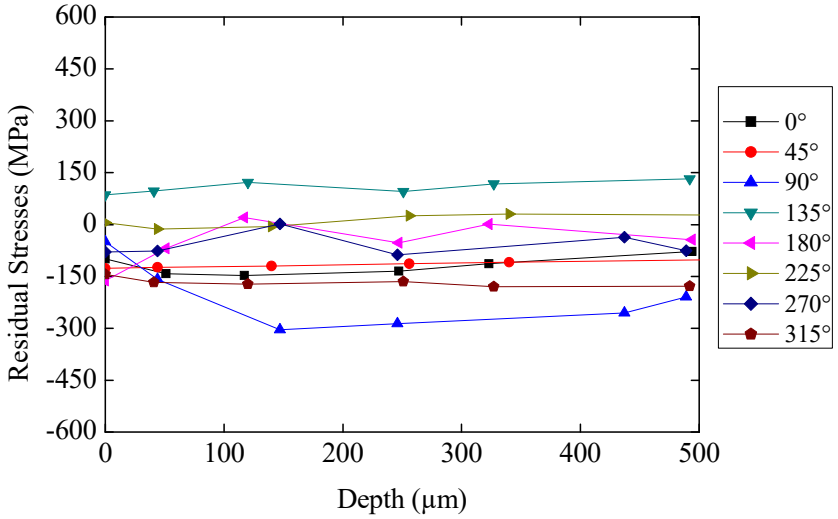

(a)

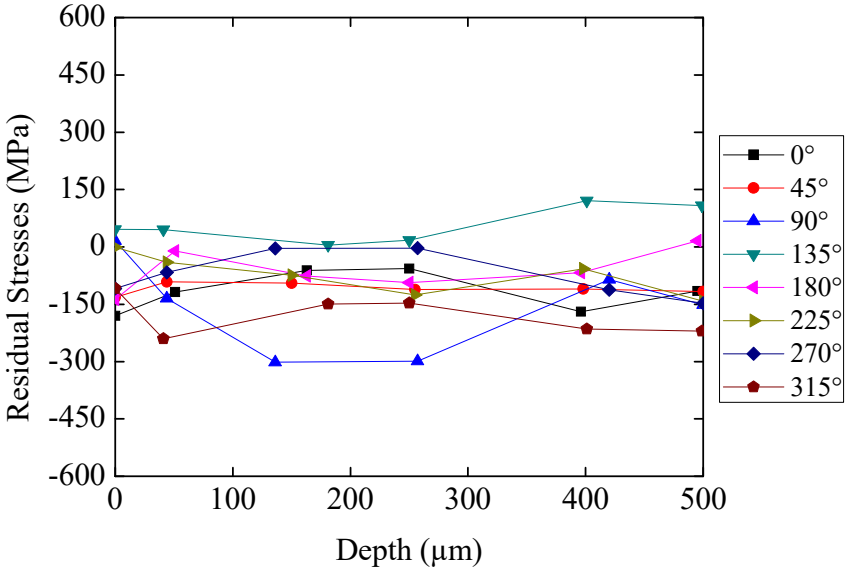

(b)

Figure 4.9: Horizontal pre-straightening: residual stresses in terms of depth at (a) 150 mm and (b) 250 mm axial positions.

Profiles of residual stress through the depth of the samples were also investigated (Figure 4.9). Residual stresses exposed in Figure 4.9 (a) indicate no significant variation with depth at the axial position of 150 mm from bar end, except at the peripheral angles of 90º and 180º, where variations of more than 200 MPa were registered at the 90º position and of almost

160 MPa at the 180º position. Conversely, residual stresses at the axial position of 250 mm from bar end are unsteady at almost all peripheral positions. The peripheral angular position of 270º has variations of 240 MPa and stresses with opposite signal to that of the 90º position, indicating that the 90º angular position has more contact with the rolls than the 270º.

In addition to the residual stresses measured by X-ray diffraction, a profile of residual stresses was determined by Neutron diffraction to investigate the behavior in the cross section of a horizontal pre-straightening sample. Resulting residual stresses and FWHM profiles for three directions (axial, radial and hoop) are depicted in Figure 4.10. The 10 mm and -10 mm values in the cross section of the bar correspond to the surfaces of the bar, whereas the zero is the center of the bar.

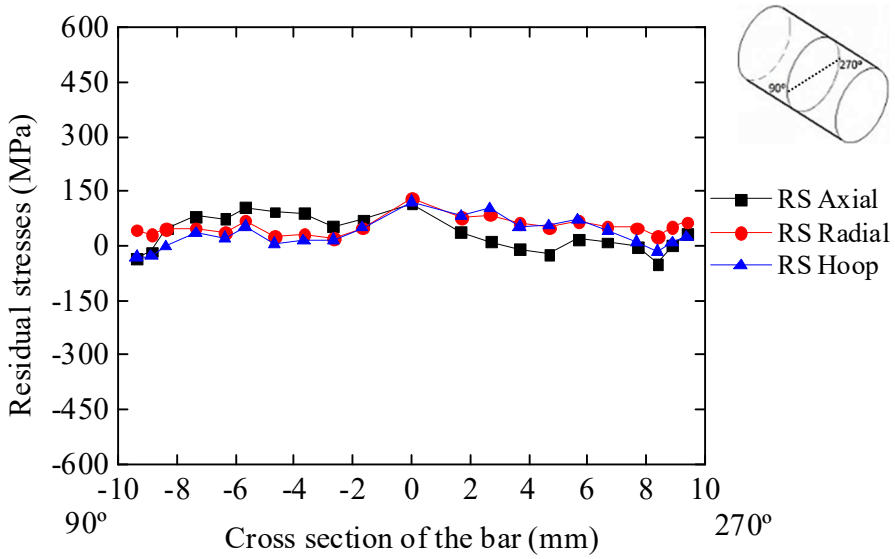

Figure 4.10: Residual stresses from Neutron diffraction at the 90º-270º section of a horizontal pre-straightening sample.

In the axial, hoop and radial directions, the maximum value of residual stresses was recorded at the center of the bar and corresponds to 140 MPa. Near the surface, residual stresses in all directions remain close to zero. Residual stresses are slightly compressive with prevalence of tensile values along the cross section of the bar in the hoop, axial and radial directions. In general, residual stresses on the surface measured by Neutron diffraction are confirmed by the results measured by X-Ray. In contrast, FWHM from Neutron diffraction has lower values, ranging from 0.42º to 0.46º, than that from X-Ray. The differences in the FWHM results are due to the use of different instrumentation and different wavelengths (CULLITY & STOCK, 2014), despite the use of the same sample.

4.1.3 Vertical pre-straightening

4.1.3.1 Microhardness and microstructure

Figure 4.11 (a) contains microhardness profiles recorded in two different cross sections of the vertical pre-straightening samples, 0º-180º and 90º-270º. The -10 mm represents the 0º and 90º side of the samples, while the 10 mm refers to the 180º and 270º side of the samples.

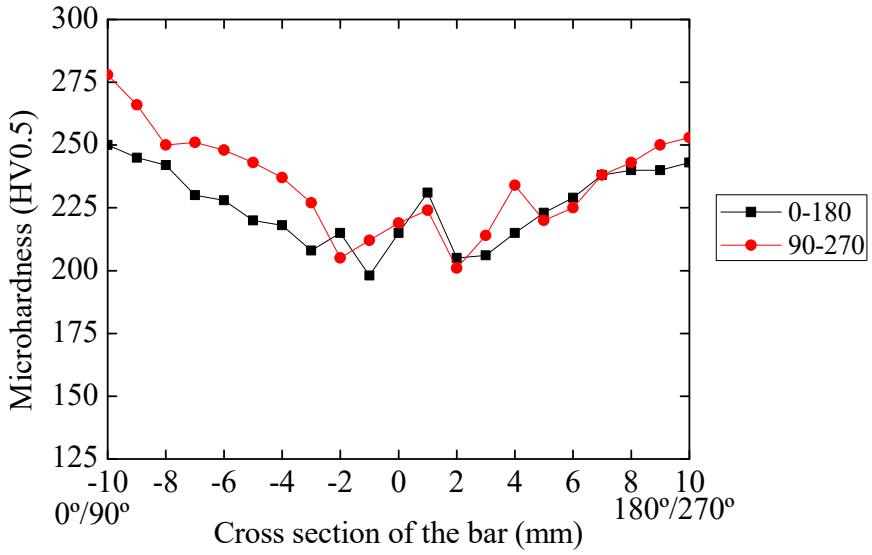

(a)

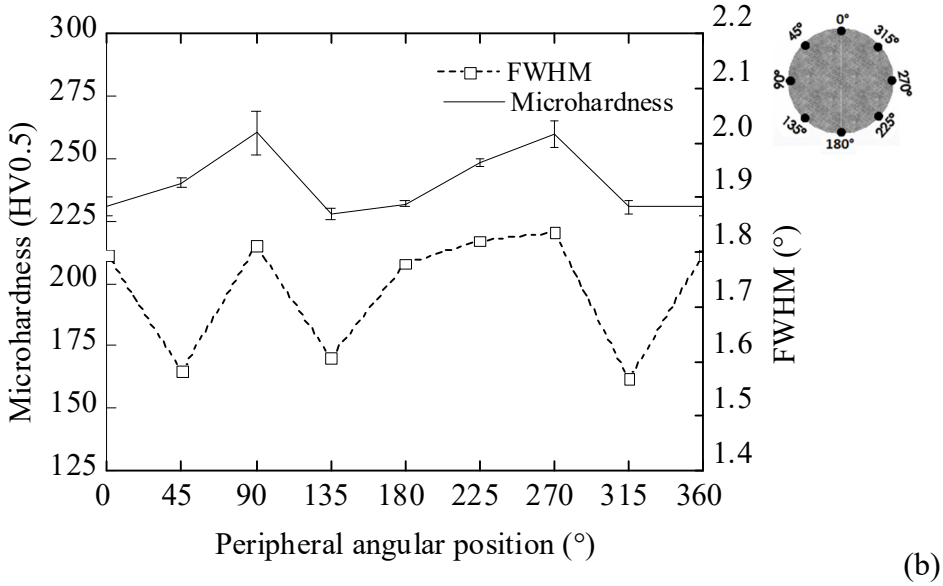

(b)

Figure 4.11: Microhardness in two different samples from vertical pre-straightening in (a) the 0º-180º and 90º-270º cross section and (b) at the peripheral angular positions, including FWHM.

Figure 4.11 (b) illustrates the microhardness at multiple peripheral angular positions. Variations in the hardness values around the bar can be observed. Hardness on the surface is equal to 278 $HV_{0.5}$ at 90º and 250 $HV_{0.5}$ at 0º. At 270º, hardness is equal to 253 $HV_{0.5}$, while the 180º angular position exhibits a value 10 $HV_{0.5}$ lower. Hardness decreases from the surface to the center in both profiles. However, there is an increase in hardness of about 30 $HV_{0.5}$ at the center in both profiles. Two peaks at 90º and 270º are evident, with an increase in the hardness values from 230 HV at 0º to about 260 HV at 90º. The discrepancy of the absolute values determined at the surface at 0º and 90º in (a) and (b) was caused using different samples for the measurement of each peripheral angular position.

Figure 4.12 depicts a micrograph analyzed by the ImageJ software developed by National Institutes of Health (a) and an Electron Backscatter Diffraction – EBSD phase analysis (b) to determine the material phase in the center of the vertical pre-straightening bar. The use of ImageJ provided the following results: for a magnification of 1000 times, the amount of pearlite is 44.78%, from which the amount of cementite (Fe_3C) is 5.56%, leading to a final amount of ferrite equal to 94.44%. On the other hand, the amount of ferrite obtained by using EBSD is 92.3%.

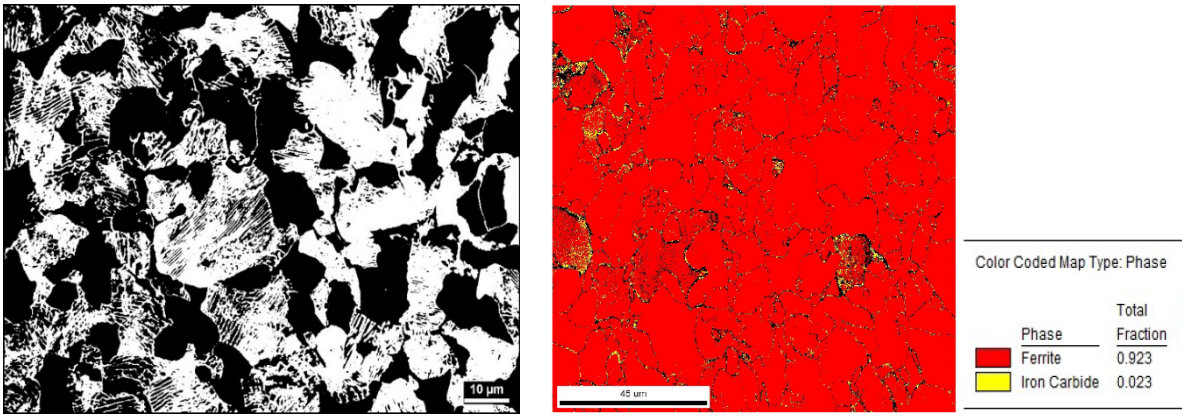

(a) (b)

Figure 4.12: Material phase analysis by (a) ImageJ and (b) EBSD phase map of the vertical pre-straightening sample.

4.1.3.2 Residual stresses after vertical pre-straightening

In Figure 4.13, residual stresses (a) and FWHM (b) in the vertical pre-straightening sample are shown. A large variation in the residual stresses at the 0° position is noticeable, with compressive values ranging from -60 MPa to -180 MPa. This heterogeneity is expected to be

caused by the contact between the bar and the vertical pre-straightening rolls' set. The FWHM values present four peaks that correspond to 0°, 90°, 180° and 270°, reaching maximum values of around 1.97°.

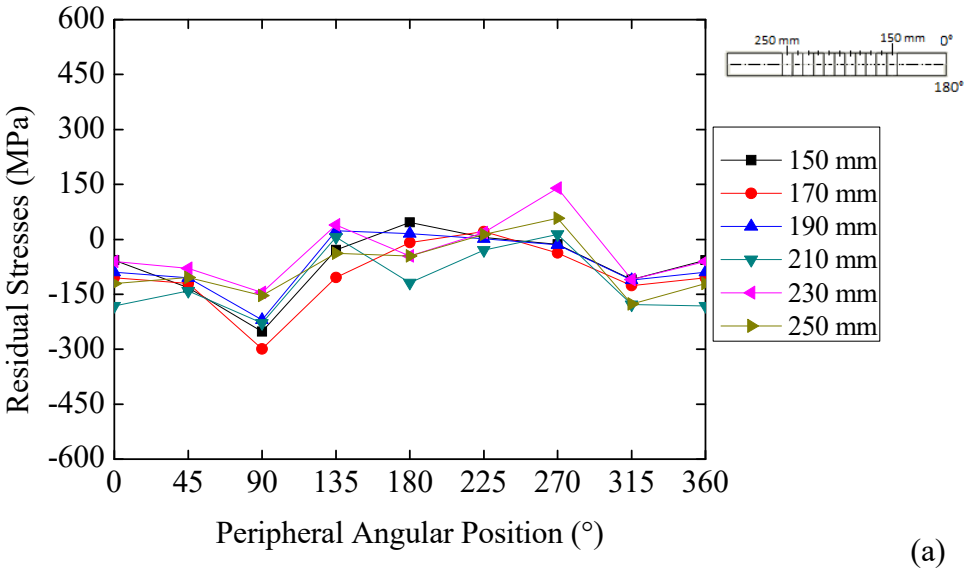

(a)

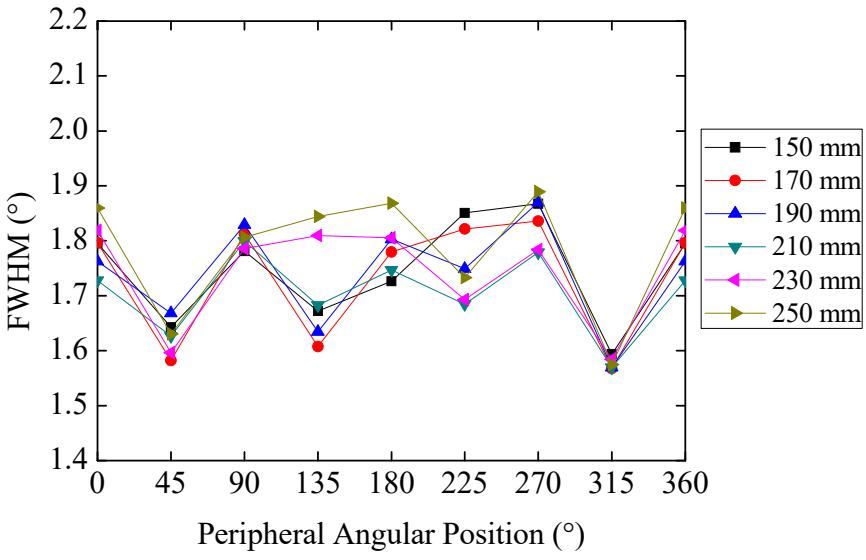

(b)

Figure 4.13: Residual Stresses on the surface of the vertical pre-straightening sample with 50 µm etching (a) and FWHM (b).

Figure 4.14 shows residual stress profiles, in terms of depth, at the 150 mm axial position (a) and at the axial position of 250 mm (b). Residual stresses at the 150 mm axial position do not show significant variations near the surface and at 500 µm depth. Conversely, the axial position of 250 mm shows non-homogeneous residual stresses near the surface, which stabilizes

beyond 150 µm depth. The angular positions of 90º and 180º show more pronounced variation in residual stresses than that of other angular positions.

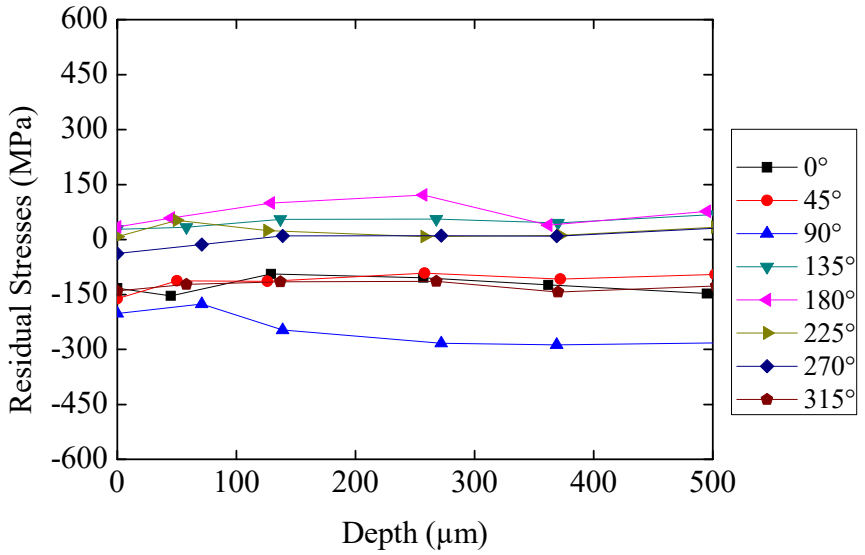

(a)

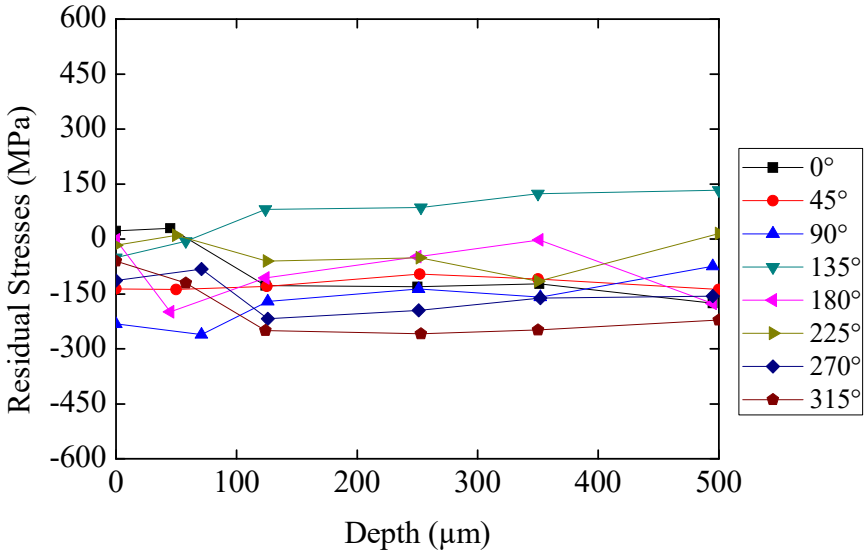

(b)

Figure 4.14: Vertical pre-straightening sample: residual stresses in terms of depth (a) 150 mm and (b) 250 mm axial positions.

Figure 4.15 shows the residual stresses of a vertical pre-straightening sample, measured by Neutron Diffraction in the cross sections 0°-180° (a) and 90°-270° (b).

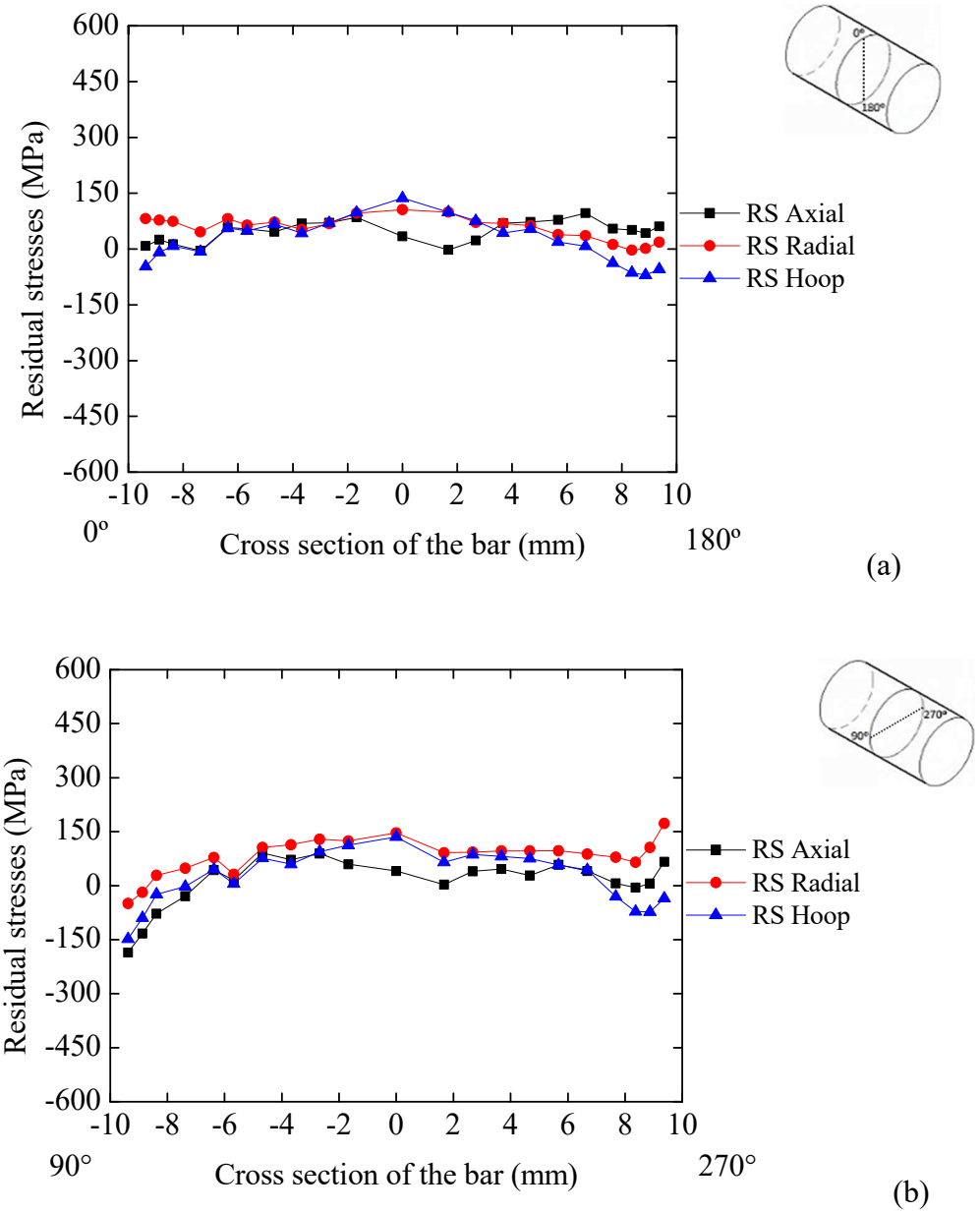

Figure 4.15: Residual stresses from Neutron diffraction in the sections (a) 0°-180° and (b) 90°-270° of the vertical pre-straightening sample.

In Figure 4.15 (a), residual stresses show heterogeneous behavior along the 0°-180° cross section, indicating an increase in the center, with a maximum value of 130 MPa corresponding to the hoop direction. The axial direction present residual stress values of 35 MPa relative to the center of the bar. The axial residual stress at 0º is close to zero, while the hoop residual stress value at 0º is equal to -50 MPa. In the 180º angle, the maximum value was found in the axial direction, which is equal to 40 MPa. A compressive residual stress of -50 MPa was found in the hoop direction.

In Figure 4.15 (b), axial residual stresses in the section 90º-270º reaches tensile value of 67 MPa in the 270º position and a compressive value of -186 MPa in the 90º, which results in a difference of over 250 MPa between the two sides of the bar. In the hoop direction, the difference between the 90º and 270º positions is 183 MPa.

4.1.4 Wire drawing

4.1.4.1 Hardness and metallographic analysis

Hardness results provided by samples from the wire drawing illustrated in Figure 4.16 show slightly differences in hardness along the cross section of the sample.

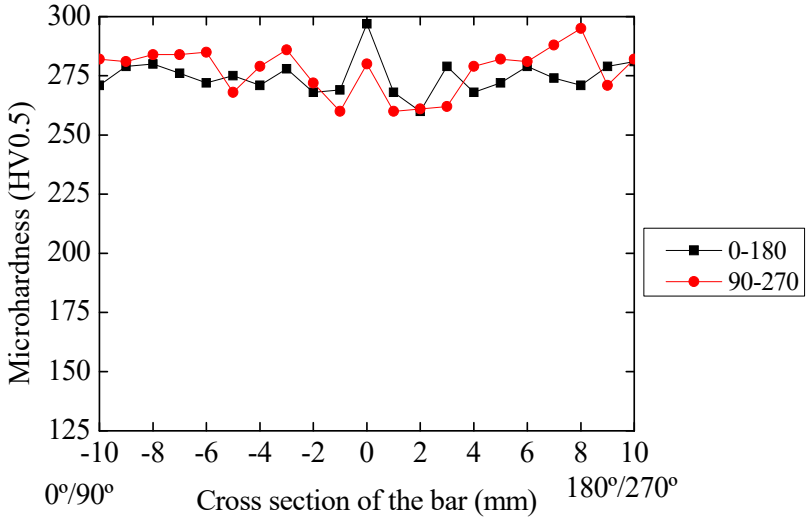

(a)

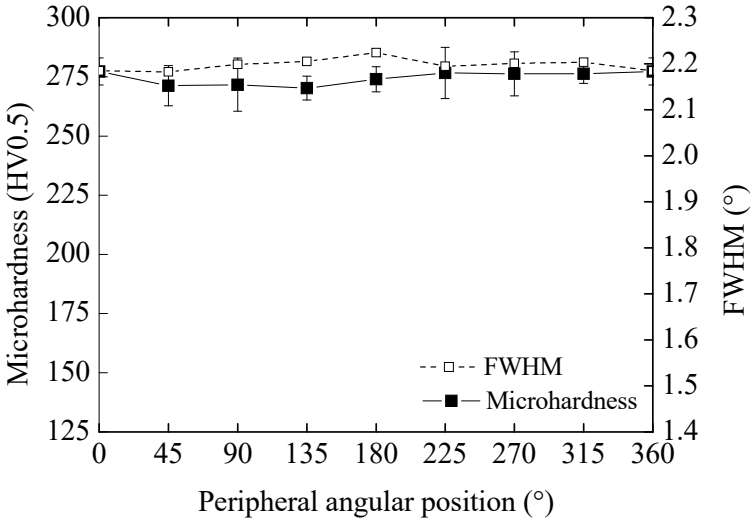

(b)

Figure 4.16: Hardness in (a) the cross section and (b) at the peripheral angular positions of the WD samples

Figure 4.16 (a) show higher hardness at the surface and a decrease towards the center. However, it is possible to notice a local increase at 0 mm in both samples. The 90º-270º profile exhibit 282 HV at the 90º position and 280 HV at the 270º position. In the center, the highest hardness was registered at the 0º-180º profile, which is equal to 297 HV. Microhardness is also shown in Figure 4.16 (b) for multiple peripheral angular positions of the wire drawing bar. At all angular positions, microhardness remains around 275 HV, while the FWHM remains constant at 2.2º.

Figure 4.17 shows micrographs from the wire drawing samples at the 0º, 90º, 180º and 270º positions. The micrographs display a typical pearlitic microstructure of the AISI 1045 and a deformation in the surface of the samples generated by the wire drawing process. The 0º and 180º positions ((a) and (b)) show higher grain elongation than that of the 90º and 270º positions ((c) and (d)).

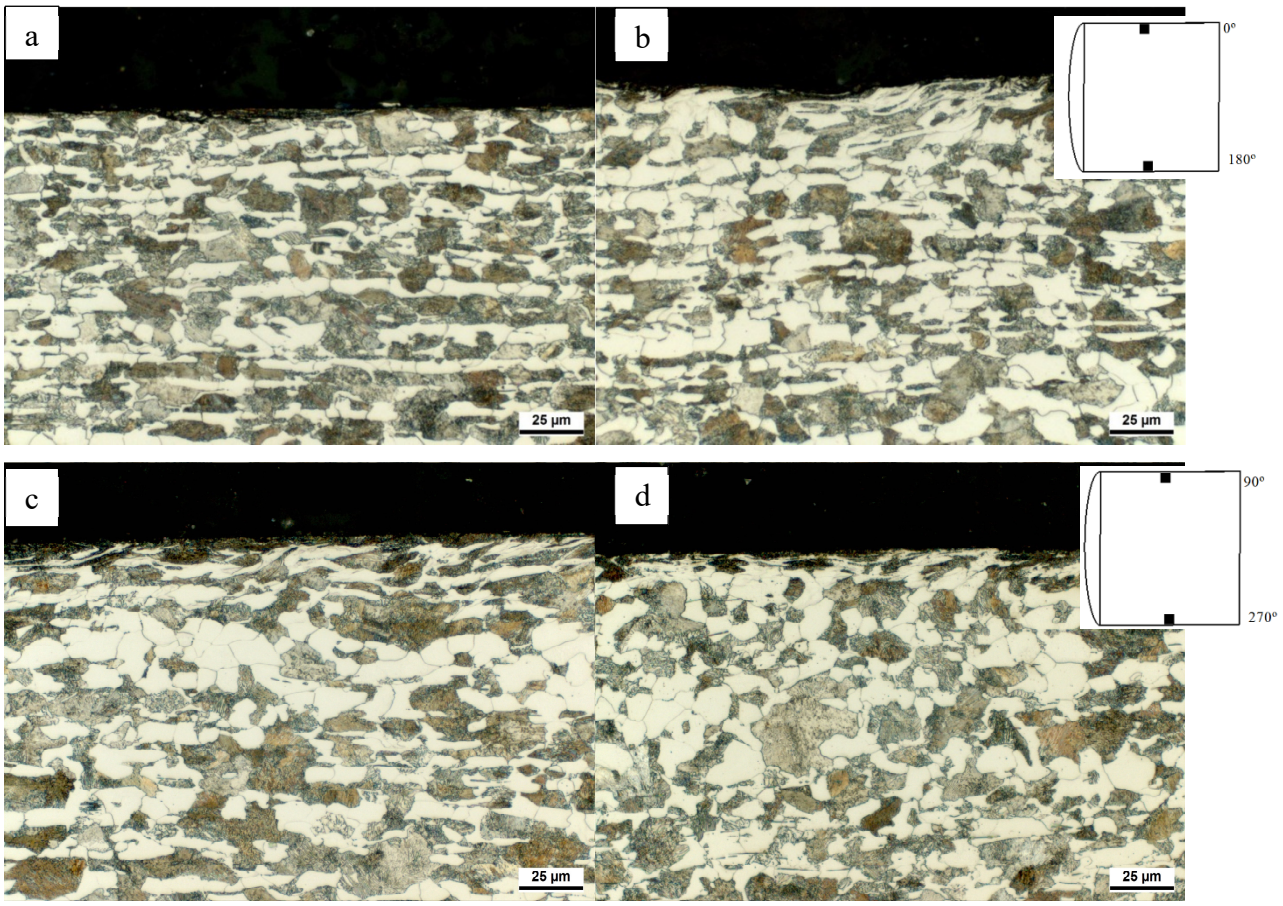

Figure 4.17: Metallography of the wire drawing samples at (a) 0º, (b) 180º, (c) 90º and (d) 270º

4.1.4.2 Residual stresses after wire drawing

Figure 4.18 (a) shows the profile of residual stresses obtained by X-ray diffraction at the surface of the samples. The respective FWHM are plotted in Figure 4.18 (b). In Figure 4.18 (a), the minimum compressive value of -30 MPa was recorded at the angular position 225º and the maximum tensile value of 330 MPa was noticed at the angular position of 135º.

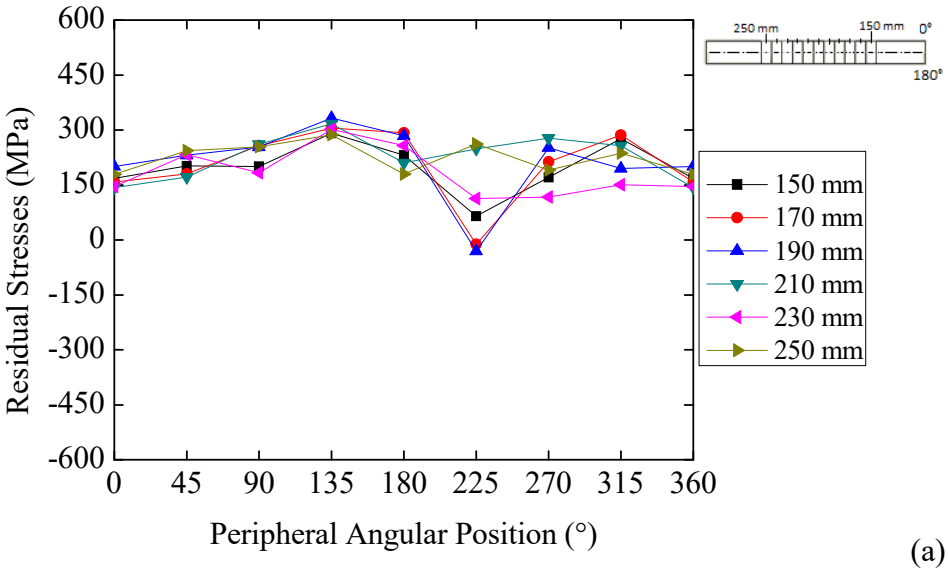

(a)

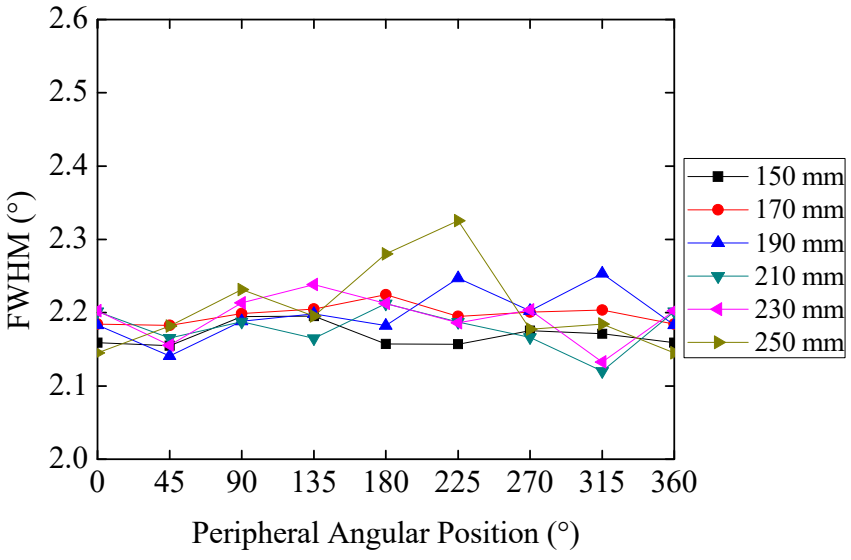

(b)

Figure 4.18: Residual stresses at peripheral angular positions (a) and FWHM (b) in the wire drawing sample with 50 µm etching for distances from 150 to 250 mm from end of the bar.

The FWHM showed in Figure 4.18 (b) has also shown a variation at the angular position 225º from 2.16º to 2.32º. As the variations at both residual stresses and FWHM were noticed

just at the angular position of 225º, could be due to local changes at the bar such as a shock between the bar and some component of the process chain.

Residual stress depth profiles in the wire drawing sample, presented in Figure 4.19, exhibit non-homogeneity near the surface, stabilizing after 50 µm depth for both axial positions, 150 mm and 250 mm. The greatest variation in residual stress is 250 MPa, which corresponds to the peripheral angular position of 225º at the axial position of 150 mm. In the 250 mm axial position, the greatest difference in residual stresses occurs at the peripheral angle of 315º, with a value of almost 270 MPa.

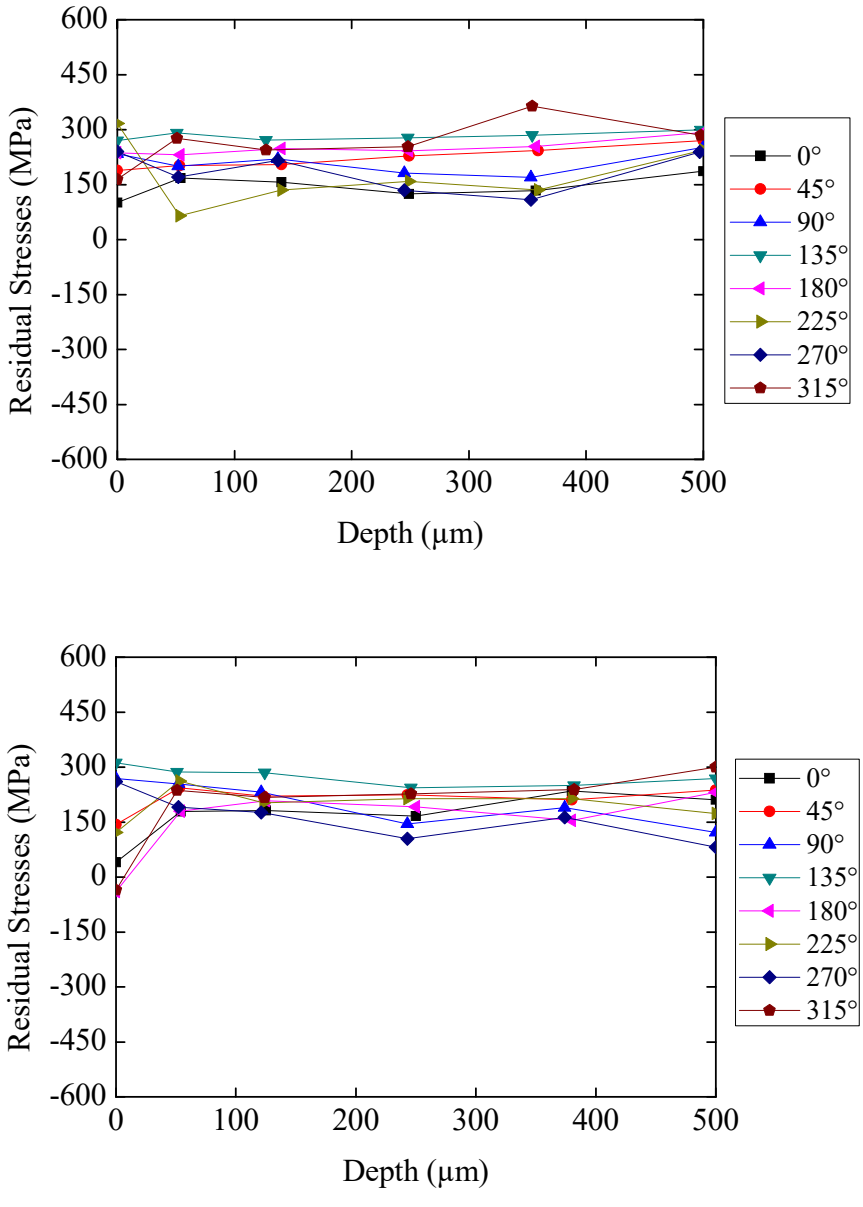

Figure 4.19: Wire drawing sample: Residual stress profiles in terms of depth at (a) 150 mm and (b) 250 mm axial positions.

The residual stress results, determined by Neutron Diffraction, in the cross section of samples from the wire drawing process were published in a previous work by Dias *et al.* (2017). The final residual stress distribution can be observed in Figure 4.20. A minimum value of -530 MPa compressive residual stress was recorded in axial direction near the center of the bar (position -1 mm), while the residual stress at the surface is about 400 MPa tensile in both sides (0º and 180º) of the bar. Hoop and radial residual stresses near the center have close values of about -240 MPa and near the surface, the radial residual stresses are close to zero while the hoop values are lower that the axial residual stresses values.

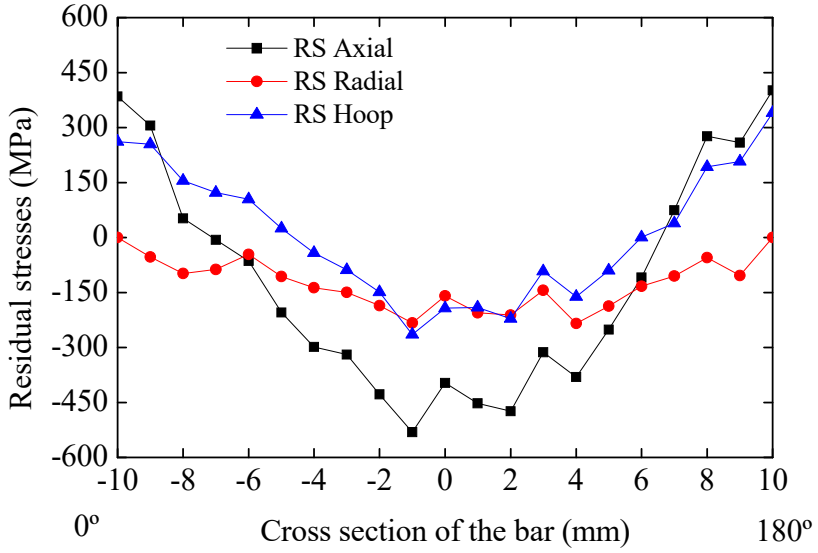

Figure 4.20: Wire drawing: Residual stresses in the cross section (0º-180º) by Neutron diffraction. Source: own work and Dias (2017).

4.2 SIMULATION RESULTS

4.2.1 Comparison between hardness and strain

To allow the comparison between the hardness values from experimental tests and the simulated strains, the method to convert strains into hardness proposed by Tabor (1948) was applied. The resulting hardness vs. strain calibration curve is plotted in Figure 4.21, which shows the experimental data and the analytical results that were calculated using theoretical equations described in the state of the art.

Variation between the two curves reaches 10% in the average values obtained from four samples with 60% reduction. The analyzed SAE 1045 raw material follows the hardness behavior calculated by Equation 4.1, adjusted for the SAE 1045 material when submitted to a simple upsetting test.

$$HV = 302.9\ (\varepsilon_0 + 0.08)^{0.1079} \qquad \text{Equation 4.1}$$

Where ε_o is the von Mises strain. The correlations proposed by Equation 4.1 and Figure 4.21 are valid solely for the SAE 1045 material, to which they may be used to evaluate strains obtained in simulation of the wire drawing process chain.

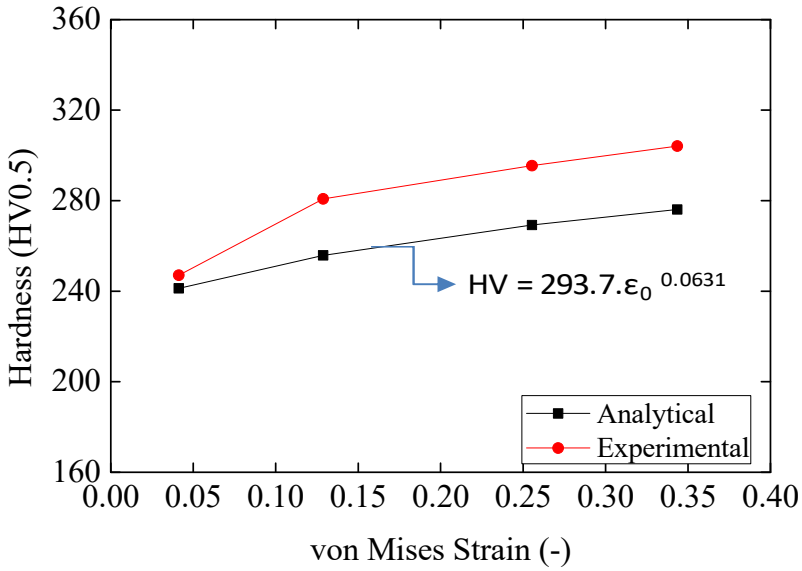

Figure 4.21: Hardness vs. Strain curve.

4.2.2 Stress development during the pre-straightening process

Figure 4.22 shows the evaluation of stresses (Frame 8 to 16) and residual stresses (Frame 19 and 20) on the surface of the bar during the pre-straightening process. Frames 8 and 9 represent the moment when the bar goes through the guide rolls. Frame 10 contains the stress upon entry into the horizontal straightening process and the activity at the 90º and 270º positions due to the action of the horizontal rolls. In frames 10 to 13, the bar is going through the horizontal process. After frame 14, the bar enters the vertical process, where activity at the 0º and 180º angles begins. After Frame 16 the bar exit the vertical process. At the Frames 19 and 20 the bar has already left the set of rolls and thus the frames portraits the residual stress distribution in the bar after vertical pre-straightening.

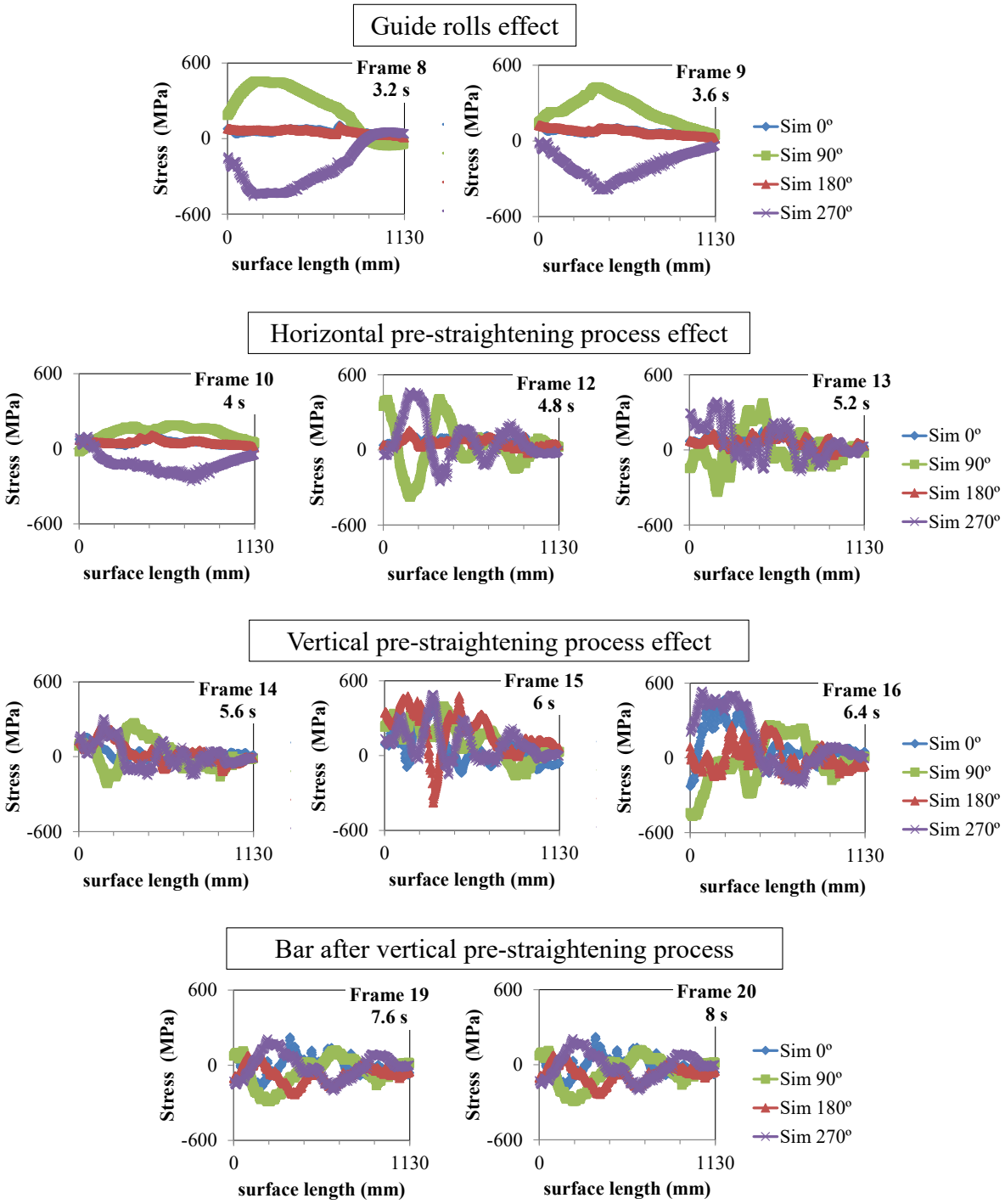

Figure 4.22: Evolution of stress during the pre-straightening process.

4.2.3 Horizontal pre-straightening

Simulation of the horizontal pre-straightening process was initially performed with the same configuration followed by the manufacturing process of the shafts. Figure 4.23 shows the axial residual stresses along the surface of the bar and the variations at the peripheral angles of

the bar. In the axial position at 0 mm is the initial part of the bar and the position 800 mm is the end of the bar. Results at the 0º and 180º peripheral positions indicate relatively the same behavior along the axial surface direction, with some minor deviations. Maximum tensile and minimum compressive residual stresses were both found at the 180º position, with values of 160 MPa and -150 MPa, respectively. The 90º and the 270º positions present opposite behavior along the axial direction, with residual stresses alternating between compressive and tensile nature. Residual stresses found at the 90º and the 270º peripheral angular positions are higher than that of the 0º and the 180º positions due to the action of the straightening rolls. The maximum value of tensile stress was identified at the 90º surface position (400 MPa). For the 270º position, a minimum compressive stress of -600 MPa was noted.

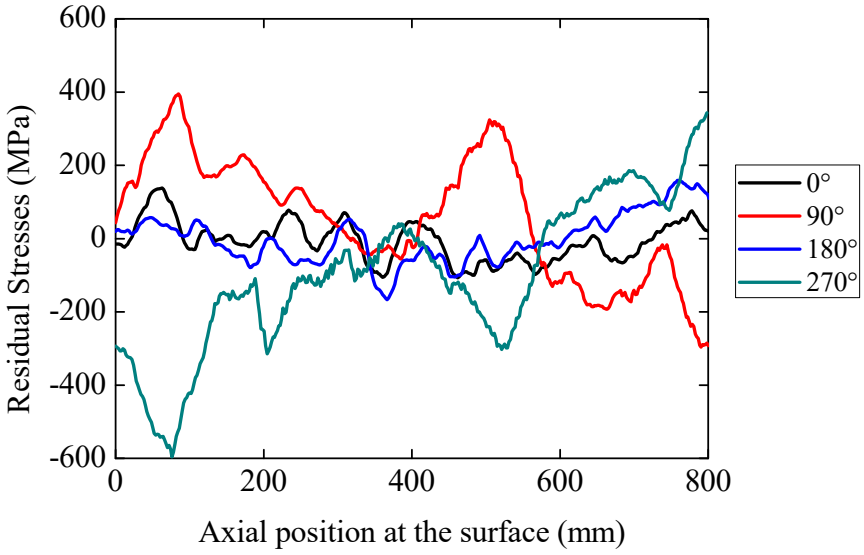

Figure 4.23: Residual stresses from simulation of bar after horizontal pre-straightening.

The simulated equivalent plastic strain profile at peripheral angular positions (0º, 90º, 180º and 270º) is presented in Figure 4.24 (a), while the maximum principal plastic strain profile at peripheral angular positions is shown in Figure 4.24 (b). Non-homogeneity in the periphery is indicated by the distinct values found for equivalent plastic strains at the 90º and the 270º angular positions. Conversely, the 0º and the 180º positions exhibit homogeneous low strain along the axial position. Residual stresses (Figure 4.23) and strains (Figure 4.24) are not significantly affected by the rolls at the 0º and the 180º peripheral angular positions. In contrast, the 90º and the 270º peripheral positions show expressive variation of the residual stresses and equivalent plastic strains.

A discrepancy in strains can be noticed in Figure 4.24 (a) from 100 mm to 400 mm surface length of the bar, where the strains at the 270º position are 50% greater than that of the 90º peripheral position.

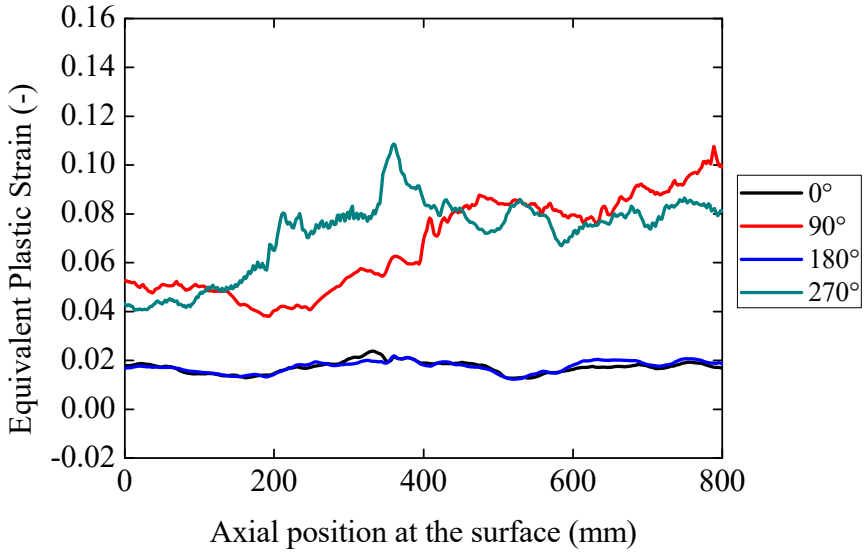

(a)

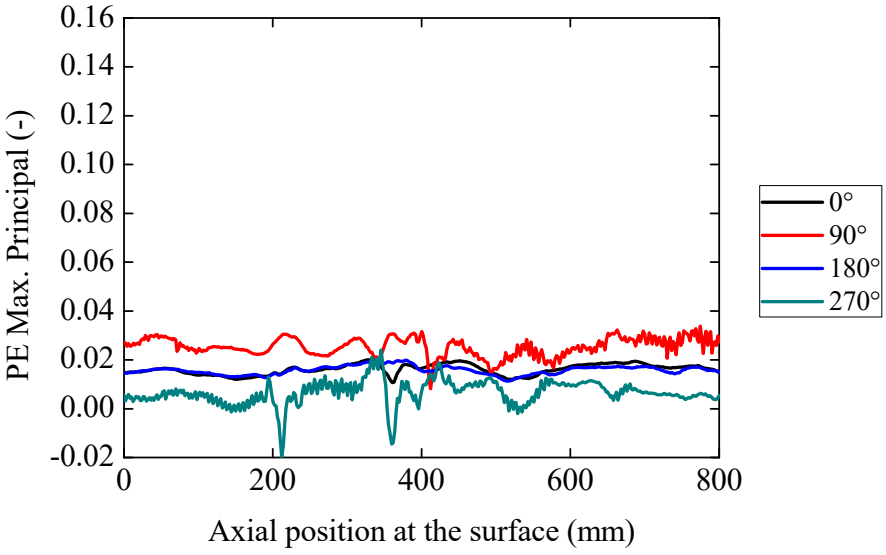

(b)

Figure 4.24: Equivalent plastic strain (a) and maximum principal plastic strain (b).

Hardness at the four main positions on the surface of the bars, calculated from the simulation data using the hardness versus von Mises strain curve, are plotted in Figure 4.25. The average hardness is equal to 226 HV at the 0º and the 180º positions. On the other hand, greater hardness is resulting at the 90º and the 270º positions, which reach 265 HV and 255

HV, respectively. In general, hardness values calculated using Equation 4.1 are in good agreement with the hardness calculated from the experimental data.

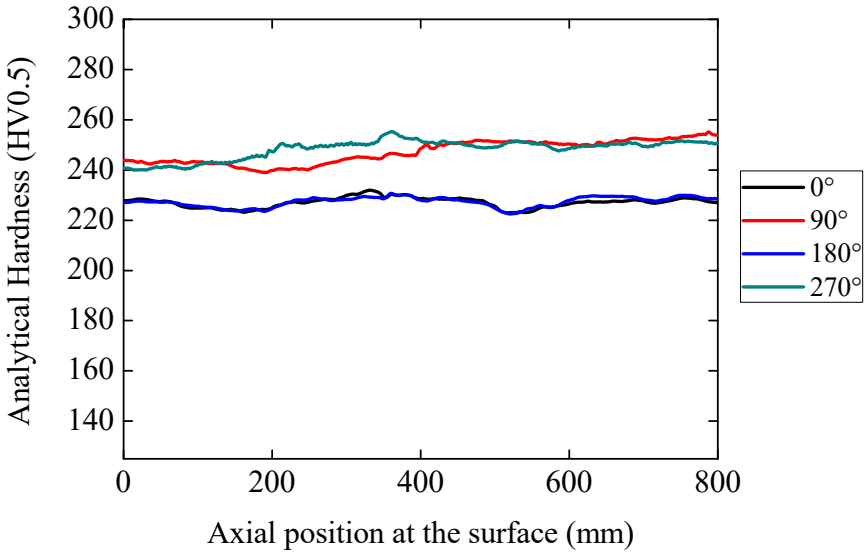

Figure 4.25: Hardness from simulation considering the experimental hardness versus strain curve of the horizontal pre-straightening process.

Figure 4.26 illustrates the simulated residual stresses and equivalent plastic strains at peripheral angular positions of the horizontal pre-straightening process two distinct portions of the simulated bar were analyzed, namely bar 1 and bar 2 as described in Figure 3.18.

The maximum residual stress corresponds to the 90º peripheral position on the surface of bar 1 (220 MPa), as shown in Figure 4.26 (a). Bar 2 (Figure 4.26 (b)) experiences stresses of compressive nature at the 90º position (-180 MPa) at five points along the bar. The minimum residual stress recorded on the surface of bar 1 is -300 MPa, which is respective to the 270º peripheral angular position. Bar 2 exhibits significant non-homogeneity at the 90º and 270º angles along the surface, as it can be observed in Figure 4.26 (b). At the 90º angular position, most points along the bar present residual stresses of compressive nature, as opposed to that observed in bar 1. Similar behavior was found at the 270º angular position, in which residual stresses are tensile at most points. Bar 2 also experienced residual stresses that are closer to zero when compared to that of bar 1.

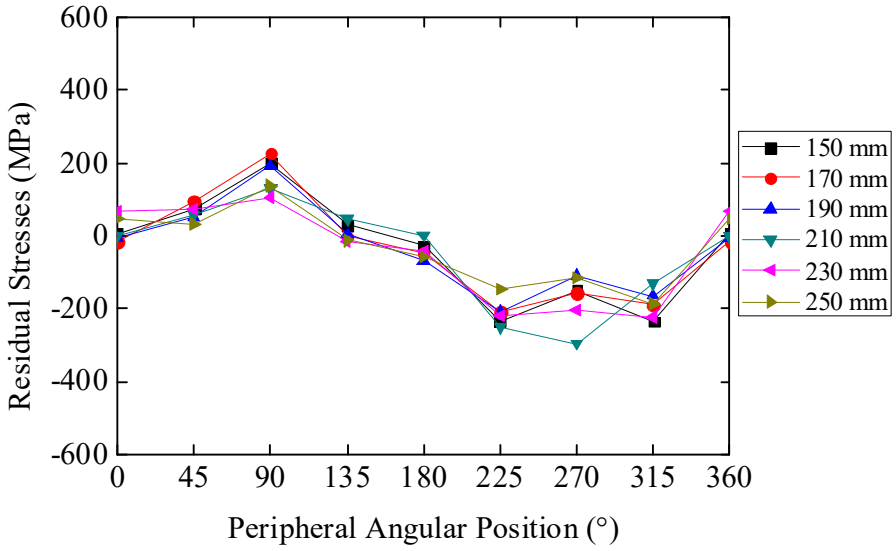

(a)

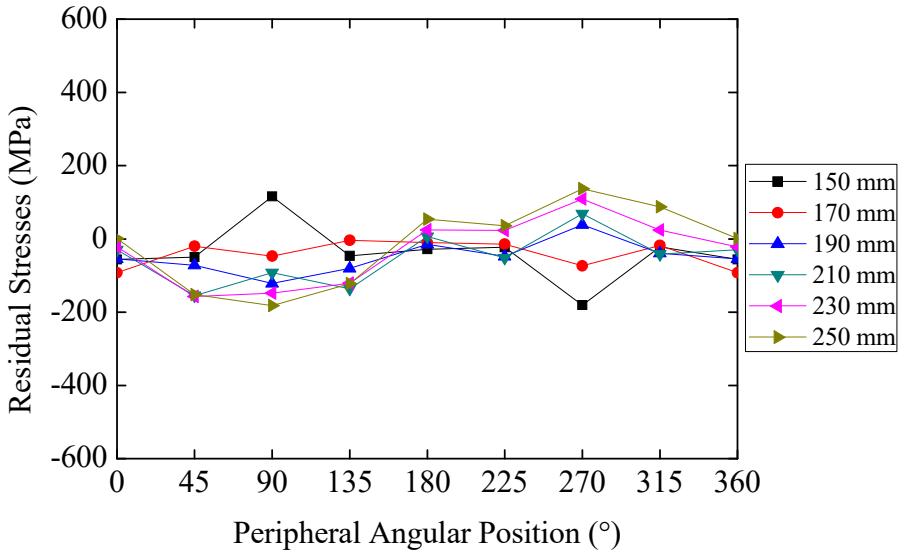

(b)

Figure 4.26: Horizontal pre-straightening simulation: Residual stresses in bar 1 (a) and bar 2 (b); equivalent plastic strains in bar 1 (c) and bar 2 (d).

Profiles of equivalent plastic strains on the surface are depicted in Figure 4.27 (a) and (b). Both bar 1 and 2 show increased values of equivalent plastic strains at the peripheral angular positions of 90º and 270º. Larger plastic strains were recorded in bar 2 with values higher than 0.08 for both 90º and 270º peripheral angles.

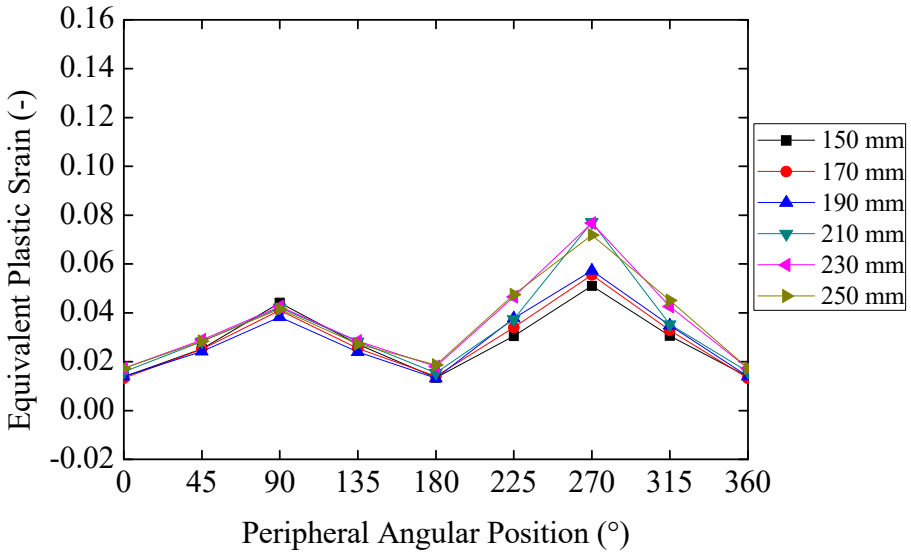

(a)

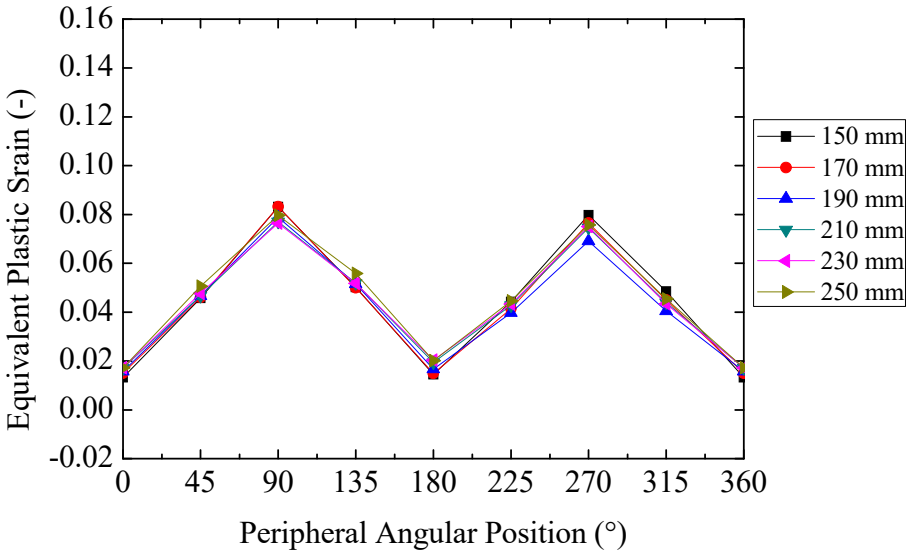

(b)

Figure 4.27: Horizontal pre-straightening simulation: equivalent plastic strains in bar 1 (a) and bar 2 (b).

In addition, residual stress profiles at the 90º-270º section were recorded in the simulated bar at a distance of 200 mm from the bar end in order to compare with the experimental data that had the neutron measurement performed at the position 200 mm. The residual stress profiles are illustrated in Figure 4.28. Residual stresses remain close to 50 MPa in the center of both sections and present varying values on the surface. At the 90º surface position, residual stress is equal to -120 MPa, while stress assumes a value of 65 MPa at the 180º surface position. For the 0º-180º section, residual stress at the 0º position is -54 MPa, which is similar to that recorded at the opposite position (180º).

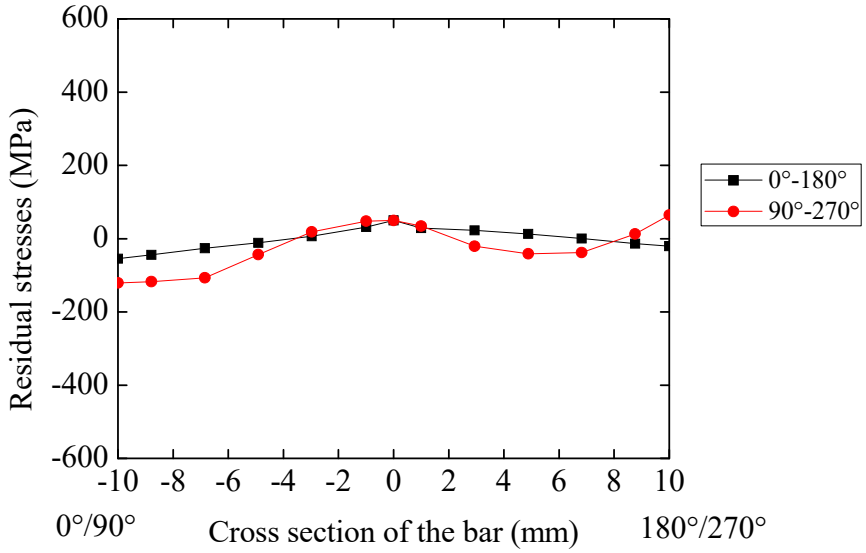

Figure 4.28: Residual stresses profiles in the cross section of the bar.

4.2.4 Vertical pre-straightening

Figure 4.29 presents the simulated surface residual stress in samples from pre-straightening, on the surface at 0º, 90º, 180º and 270º angular positions along the bar length. An increase in the magnitude of residual stresses along the surface length is noticeable. The maximum residual stress is equal to 500 MPa, which corresponded to the 270º position. On the other hand, the minimum value was found as -450 MPa at the middle length of the 90º position. This indicates a behavior that is opposite to that found in the horizontal process, in which residual stresses at the initial portion of the bar manifested tensile behavior.

The equivalent plastic strains in terms of surface length of the bar are depicted in Figure 4.30. The 0º and the 180º positions exhibit similar behavior along the entire length of the bar, as it can be observed in Figure 4.30. In contrast, the 90º and the 270º peripheral positions show a divergence in strain distribution that is almost 33% greater than the divergence between the values at the 0º and the 180º position.

In addition, surface residual stresses were generated by numerical simulation at eight peripheral angular positions on the surface of the simulated bar, at six different point along the length. Figure 4.31 presents the residual stresses in the simulated bar 1 (a) and bar 2 (b) and the equivalent plastic strains are shown in Figure 4.32 in bar 1 (a) and bar 2 (b) at each peripheral angular position.

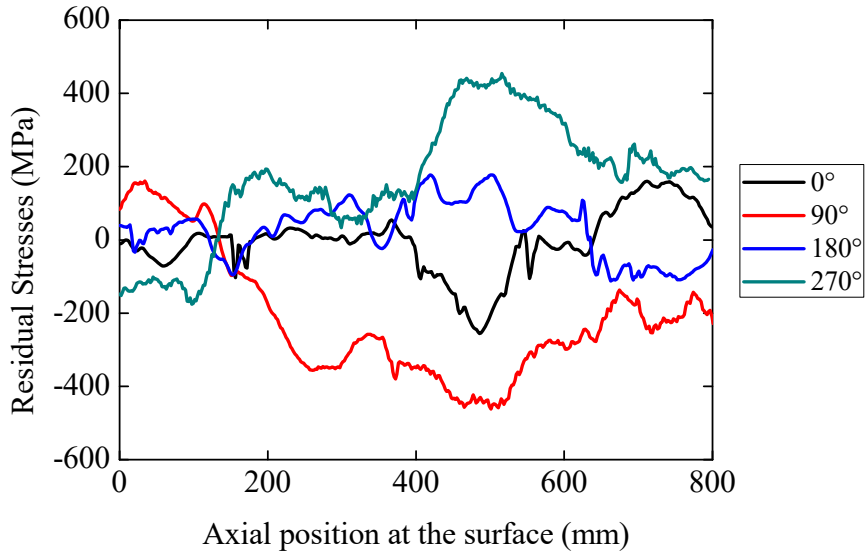

Figure 4.29: Residual stresses from simulation on the surface of the bar

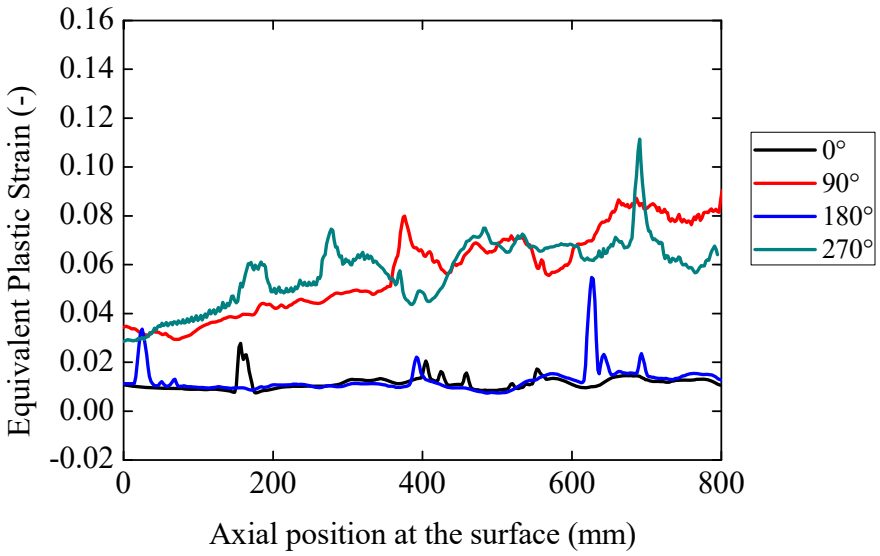

Figure 4.30: Equivalent plastic strain distribution.

Residual stress results from simulation of bar 1 reach 200 MPa at the angular position of 315°, and -350 MPa at the 90° peripheral angle, as shown in Figure 4.31 (a). Bar 2 exhibits similar compressive residual stresses at the 90º position, and the maximum tensile stress is equal to 400 MPa relative to the 270º position. In terms of equivalent plastic strains, after vertical pre-straightening, like after horizontal pre-straightening, bar 2 has greater strains when compared to bar 1, and increased strain values at the 90º and the 270º peripheral positions. As it was

previously presented in Figure 4.29, the residual stress values have a large variation along the surface length at all peripheral angles.

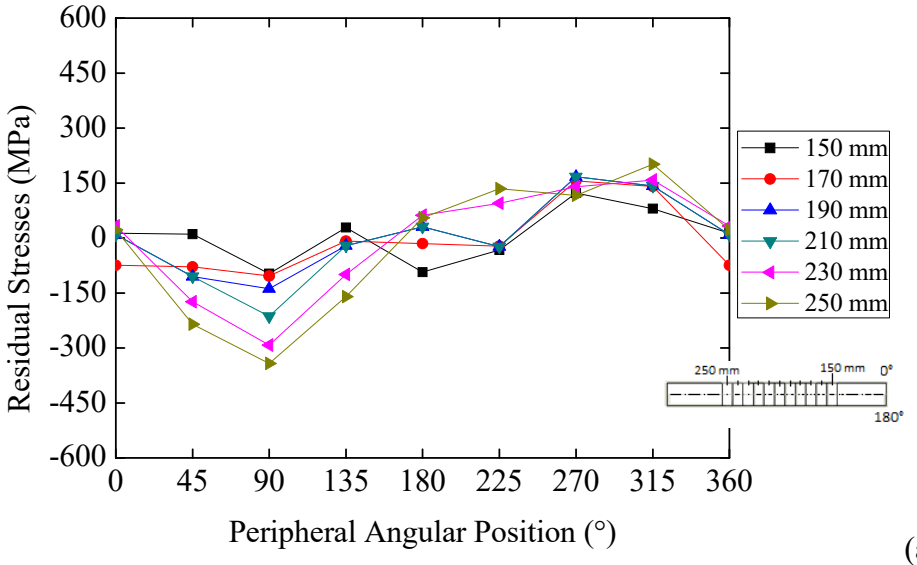

(a)

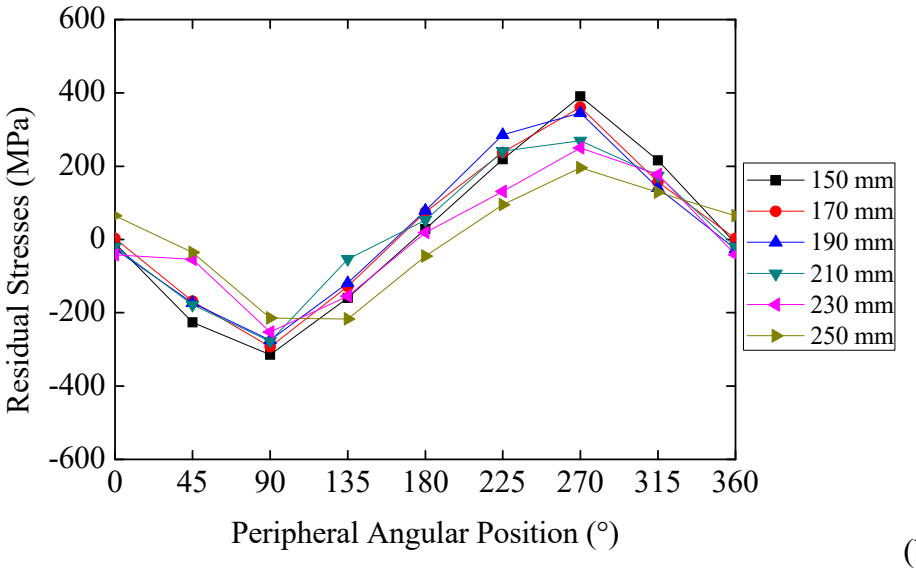

(b)

Figure 4.31: Vertical pre-straightening simulation: Residual stresses in bar 1 (a) and bar 2 (b) as a function of angular positions for different distances.

Profiles of equivalent plastic strains are depicted in Figure 4.32(a) and (b) and show for both bar 1 and 2 increased values of equivalent plastic strains at the peripheral angular positions of 90º and 270º. Larger plastic strains were recorded in bar 2 at the peripheral position 90º with a maximum value close to 0.08.

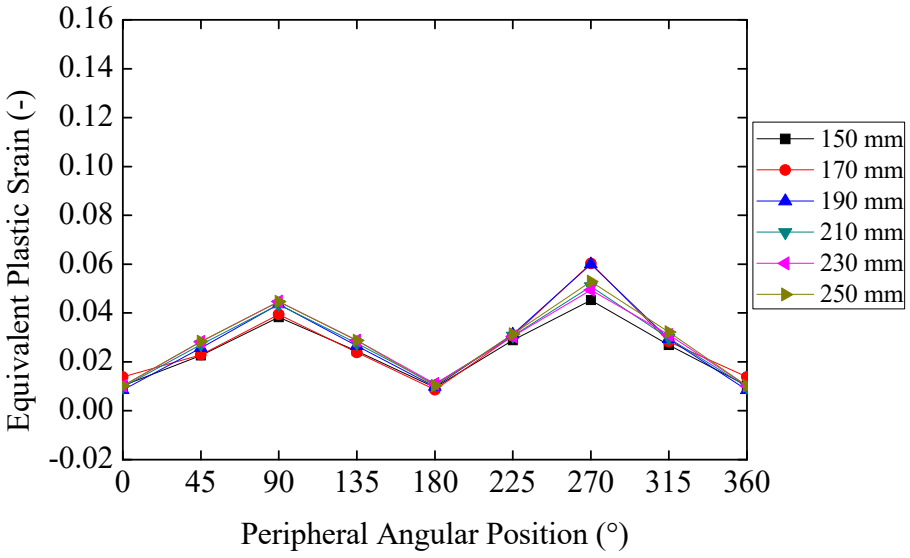

(a)

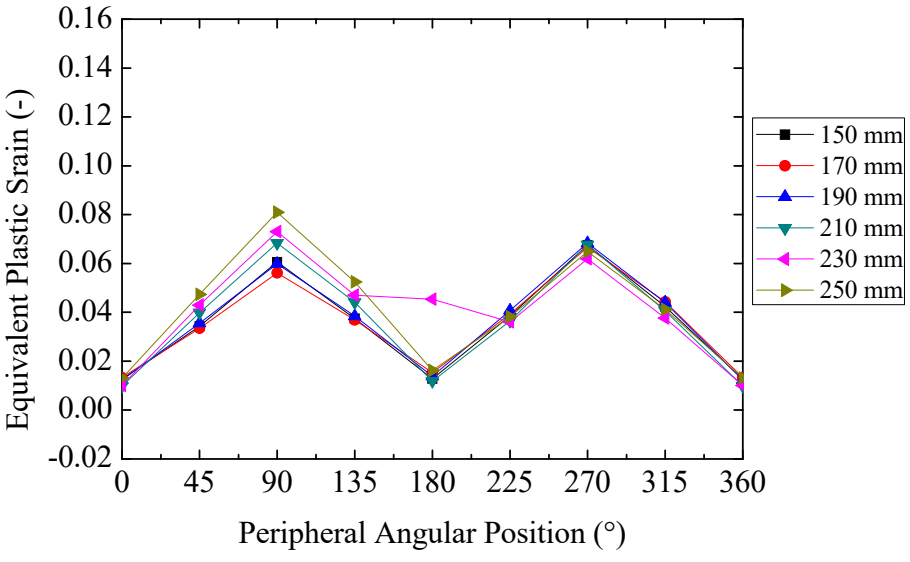

(b)

Figure 4.32: Vertical pre-straightening simulation: Equivalent plastic strains in bar 1 (a) and bar 2 (b) as a function of angular positions for different distances.

Figure 4.33 depicts the average hardness values obtained from the calibration curve, from Equation 4.1 and from the experimental measurements. Values of calculated hardness are similar to that of experimental measurements. The greatest deviation was noticed at the peripheral angles of 0º and 180º, which is about 10%.

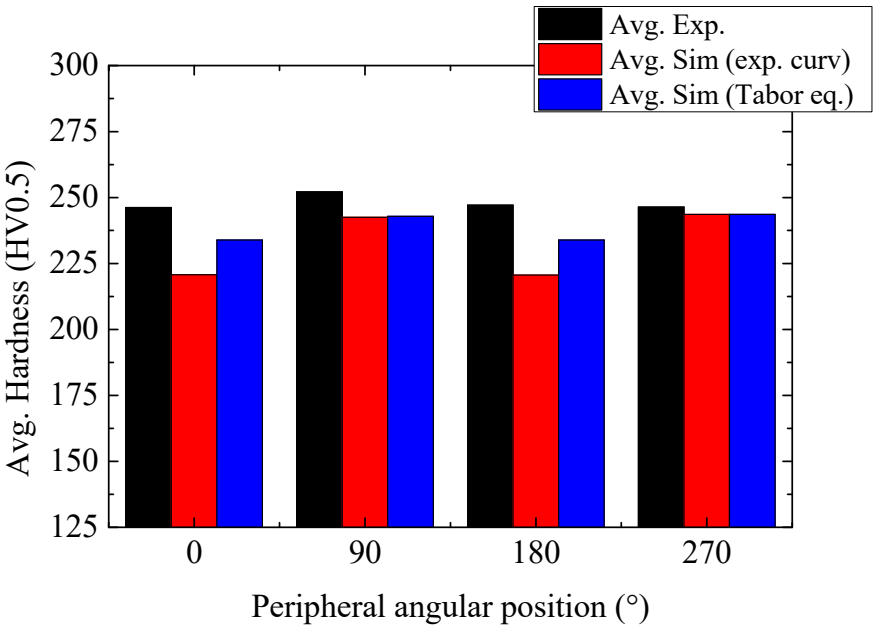

Figure 4.33: Hardness in the vertical pre-straightened bar by experimental measurements and simulation.

4.2.5 Wire drawing

Figure 4.34 shows the residual stresses at the peripheral angular surface positions of the simulated wire drawing step at two different portions of the simulated bar (named bar 1 and bar 2). As already described in the numerical simulation procedure, resulting stresses and strains from the pre-straightening process were considered in the simulation of the wire drawing process. Results from the wire drawing step show different residual stress values around the surface of bar 1 and bar 2, with the majority being of tensile nature. In contrast, the peripheral angle 270º has compressive residual stresses.

In Figure 4.34 (a), it is possible to note that residual stresses at the 270º angular position of bar 1 are of compressive nature, with a minimum value that is lower than -200 MPa. The maximum residual stress value in bar 1 was found at the 45º peripheral position, which is a tensile stress of 500 MPa. Bar 2 (Figure 4.34 (b)) exhibits more homogeneous values of residual stresses than bar 1, with the 315º peripheral position showing the minimum stress value of 45 MPa and the 135º angular position showing the maximum tensile stress value of 400 MPa. Residual stresses illustrated in Figure 4.34 exhibit variations along the bar length, which are further detailed in Figure 4.35. It is worth mentioning that residual stresses were taken at a stable portion of the bar, which had no influence from the ends of the bar.

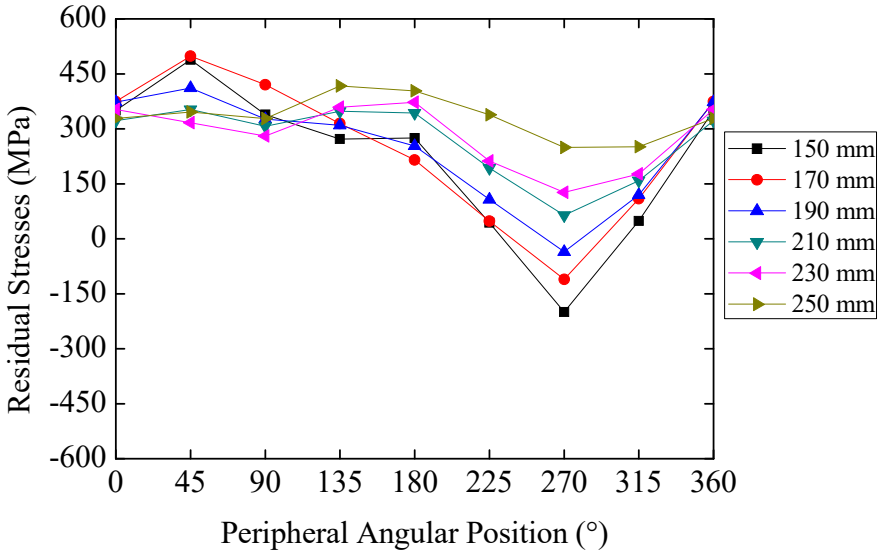

(a)

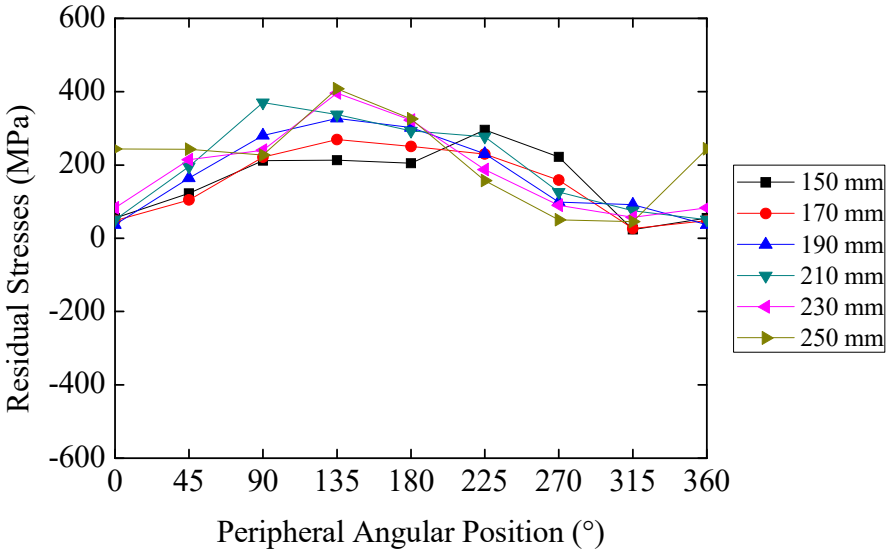

(b)

Figure 4.34: Wire drawing simulation: Surface residual stresses in bar 1 (a) and bar 2 (b).

Figure 4.35 depicts the simulated residual stresses along the surface of the drawn bar. A significant variation in the residual stress values in bar 1 is evident if the angles are evaluated separately. After the axial position of 300 mm, the residual stresses become more homogeneous. Compressive stresses appear just at the 270º angular position. The maximum and minimum values of residual stress were recorded at the 90º and 270º angular positions, respectively.

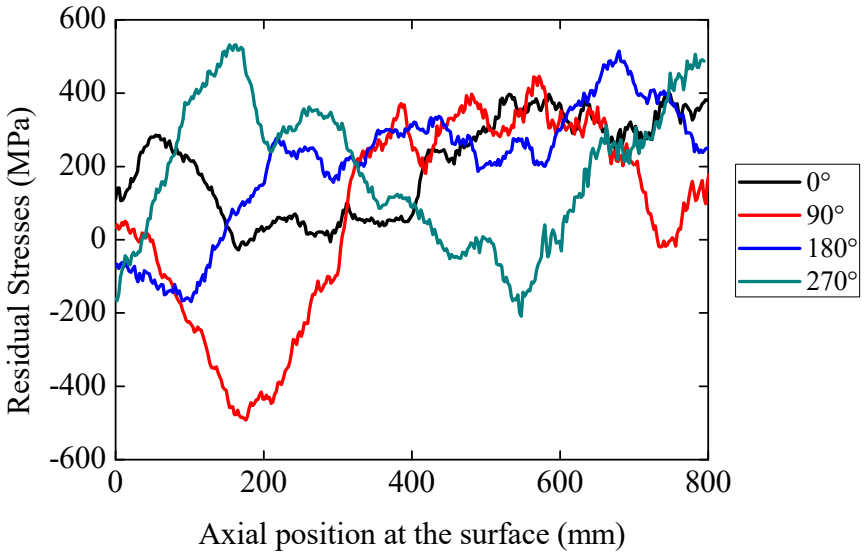

Figure 4.35: Residual stresses along the surface length of the bar in the wire drawing process.

Figure 4.36 presents residual stresses at two distinct cross sections (0º-180º and 90º-270º) of the simulated drawn bar after wire drawing. Given the large variations found in the values relative to the ends of the bar, the two presented profiles were taken from the region where residual stresses are stable. Variations on the surface of the bar, depicted in Figure 4.36, between the 0º and the 90º angular positions can be estimated at around 280 MPa, while variations between the 180º and the 270º angular positions are around 180 MPa. In the middle of the bar, the variation is reduced to 50 MPa at the -2 mm position.

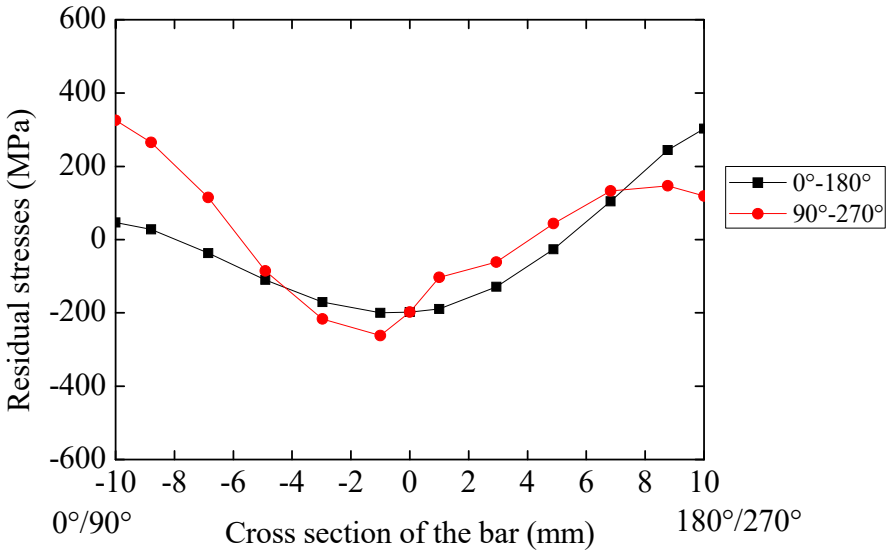

Figure 4.36: Residual stresses in the cross sections of the simulated bar of the wire drawing process.

5 DISCUSSION

In this section a discussion of the experimental and simulation results of hardness, strains distribution and residual stresses is performed. In addition, the new configuration of the horizontal pre-straightening rolls is shown.

5.1 EVALUATION OF EXPERIMENTAL RESULTS

5.1.1 Hardness and metallographic analysis

Hardness values measured at the peripheral angular positions of raw material, vertical and horizontal pre-straightening, and wire drawing samples are plotted in Figure 5.1 (a). An increase in hardness from one step to next in the process chain is evident. The vertical pre-straightening process shows greater influence in the global increase of hardness. Significant variations are noticeable at the peripheral positions of 90° and 270° among the samples, which surfaced due to the contact of these points with the rolls from horizontal pre-straightening. In contrast, no variations are noticed in the drawn sample. The wire drawing sample exhibits a high Vickers hardness at all peripheral position, with an average of 275 $HV_{0.5}$, which is 22.7 % higher than the average hardness of the raw material. This increase in the hardness values is due to the strain hardening that occurs from one step to another.

Generated strains and resulting work hardening can be analyzed by the full width at half maximum (FWHM) measurements shown in Figure 5.1 (b). Horizontal pre-straightening step presented greater values than that in the vertical step, which is attributed to the bending present in the raw material, acquired during storage. For this reason, higher residual stresses are observed in the contact points with the pre-straightening rolls. In fact, the influence of this initial bending in generating higher residual stresses and work hardening at specific points is still noticeable after the vertical step. Figure 5.1 shows evidence of this phenomenon, where it can be observed that these two peripheral angles (90º and 270º) have 16% increase in FWHM values in relation to the previous angles (45º and 225º) in the horizontal pre-straightening. Such evidence shows that the horizontal pre-straightening has a great influence in the homogeneous strain profile and should be carefully controlled.

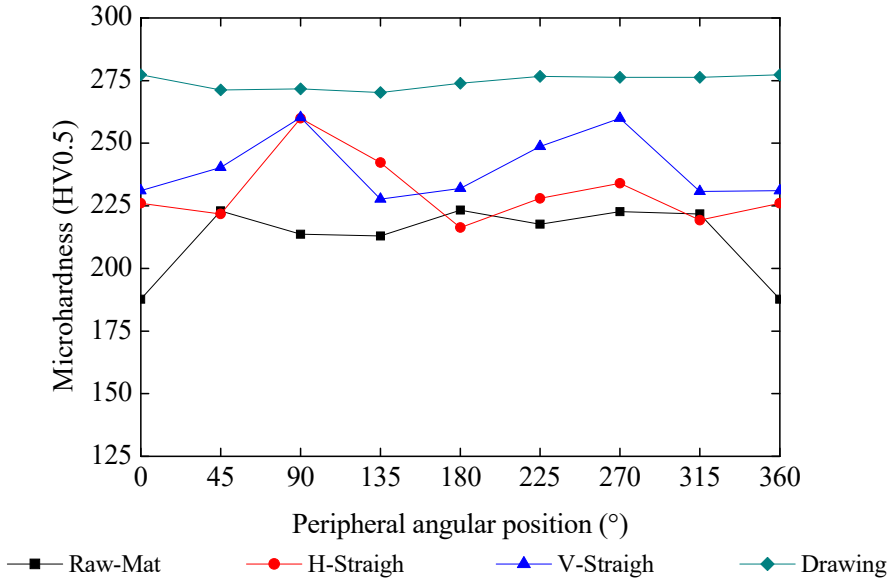

(a)

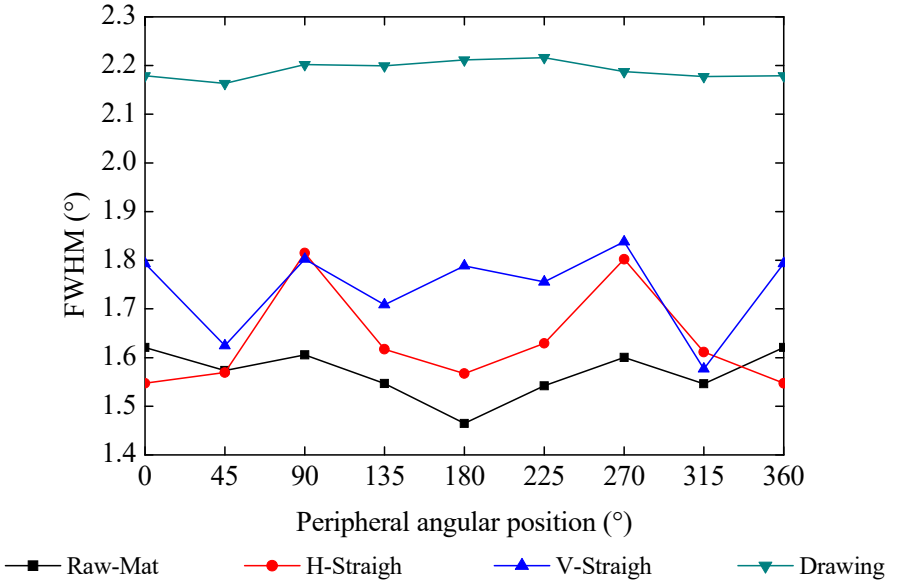

(b)

Figure 5.1: (a) Experimental hardness (HV0.5) and (b) full width at half maximum (FWHM) at the peripheral positions of the raw material, after horizontal (HPS) and vertical (VPS) pre-straightening and wire drawing.

Hardness obtained in the cross section of the raw material (RM), horizontal pre-straightening (HPS) and vertical pre-straightening (VPS) samples are compared and plotted in Figure 5.2. The center point of sample VPS for both profiles (0-180º and 90-270º) exhibits increase peaks in hardness values (0 to 6 in the cross section), which is due to segregation in the central area of the material. Segregation is an accumulated alloying element with different

chemical composition that can be generated during the solidification of melt steel. Dias *et al.* (2015) and Dias (2018) have showed that segregations alter the mechanical properties of the affected area due to their higher carbon content and could be a cause of final distortion behavior. In addition, the segregation described by Dias (2018) was present in the center and in the surroundings of the sample. With regard to residual stresses, the segregation provides an increase in the value of residual stresses in the places where it is present as well as in hardness.

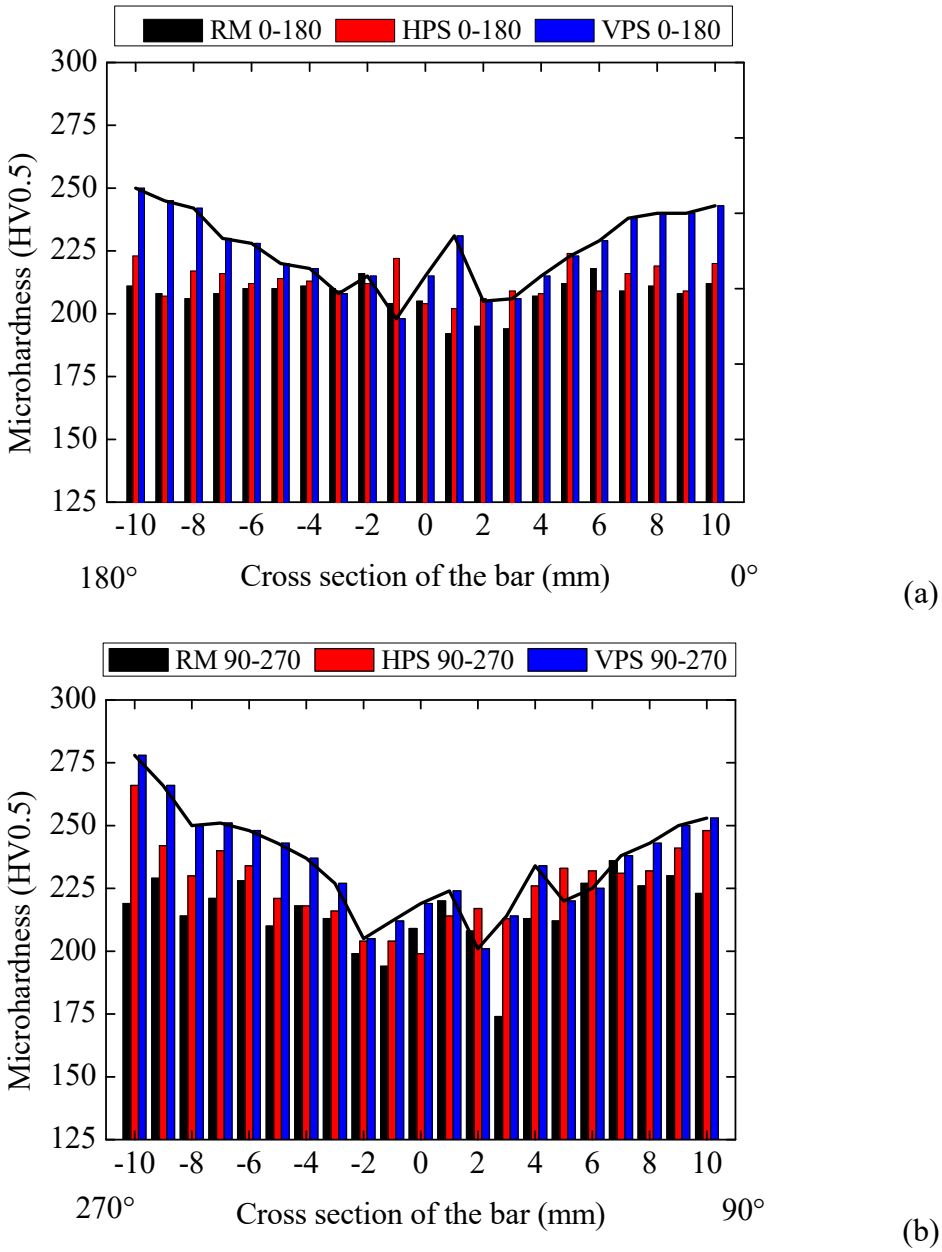

Figure 5.2: Experimental hardness (HV0.5) in the cross sections of RM, HPS and VPS samples: (a) 0°-180° and (b) 90°-270°.

Figure 5.3 illustrates the hardness values measured at the four principal peripheral angular positions of samples RM, HPS and VPS. Significant variation is present around the bar, among the four analyzed positions of the samples, which might be a possible distortion potential.

Heterogeneous hardness values can be observed at peripheral positions from the raw material, what is carried to the pre-straightening steps. It is important to notice that this is a continuous process where the bar can present a rotational movement, which will have influence on the hardness profile.

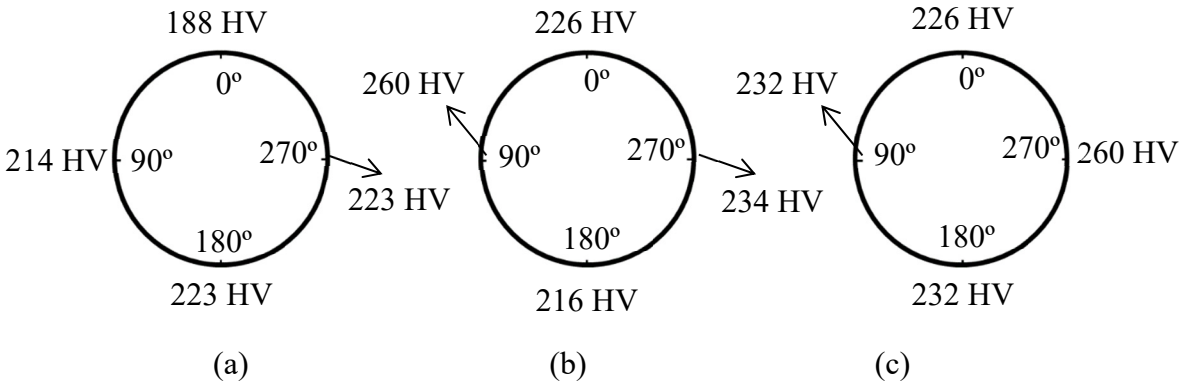

Figure 5.3: Hardness at four principal angular positions of the (a) RM, (b) HPS and (c) VPS samples.

Figure 5.4 presents hardness results after wire drawing, and Figure 5.5 presents a micrograph at the cross section with the core segregation in a drawn sample.

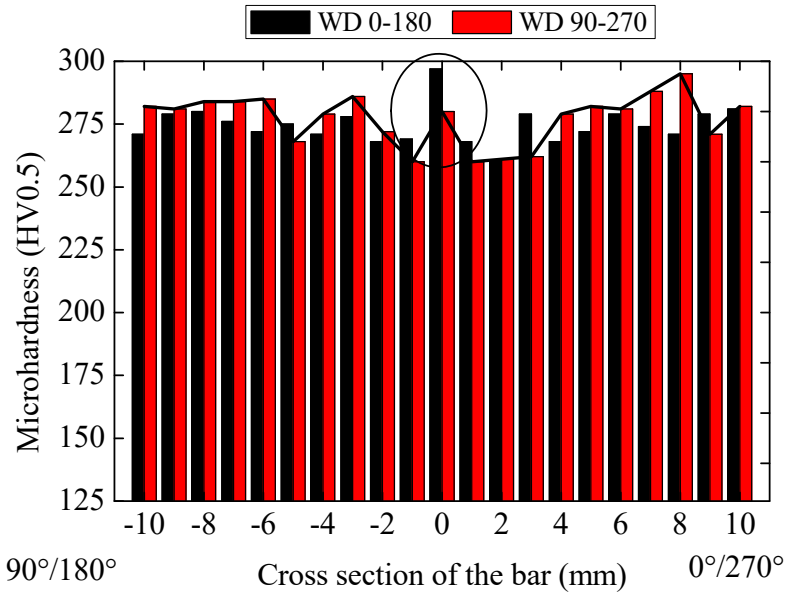

Figure 5.4: Hardness in the cross sections of the wire drawing samples.

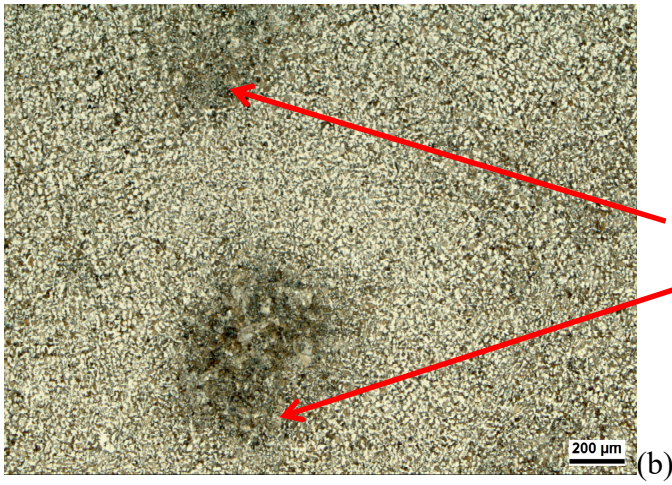

Figure 5.5: Optical micrograph at the cross section of a wire drawing sample with a core segregation.

Along the cross section of the drawn bar, hardness is expected to be higher near the surface and to decrease towards the center. However, in Figure 5.4, one peak can be observed, at which hardness is increasing near the center of the sample. This abnormality is explained by the segregation band present in the sample, as mentioned before, which is depicted in Figure 5.5. It is worth remembering that the segregation band is not exactly distributed along the center line of the bar but rather in the surroundings at the center of the bar as explained by Dias *et al.* (2015) and Dias (2018).

5.1.2 Residual stresses

Regarding the evaluation of residual stresses, experimental results revealed significant evolution in the stress values at the different peripheral angular positions in samples from all steps of the process chain that should be discussed in this section. This development was also observed by Hirsch *et al.* (2014) when evaluating residual stresses after wire drawing at different peripheral angular positions.

In the raw material, the residual stresses measured by X-Ray diffraction on the surface of the bar at the 90º angular position, which has contact with the coil, present a compressive behavior (Figure 4.4a), while the stresses at the 270° angular position have a tensile behavior. These residual stresses on the surface of the raw material are caused by rolling and coiling of the material in the final stages of the manufacturing process. According to Nunes (2012), the coiled raw material passes through air cooling and for this reason the external part of the bar has lower levels of temperature than the core of the material causing different levels of

volumetric dilatation. This temperature gradient that arises during cooling generate residual stresses (LU, 2002) with higher values on the surface than in the core. In addition, manufacturing processes such as rolling and straightening also generate residual stresses due to mechanical loads that cause heterogeneous plastic strains between the core and surface of the bar. Besides, the FWHM of the diffraction peak has shown differences between the angular positions of the raw material. This behavior of the FWHM shows the different plastic deformations generated by the thermal stresses suffered by the material during the non-homogeneous cooling.

After horizontal pre-straightening, compressive residual stresses tend to invert values, as it can be observed comparing Figure 4.4a and Figure 4.8a. In other words, Wang & Gong (2002) state that the portion of the bar that has an initial plastic compression produces a tensile yield stress lower than the original compression yield stress. The same phenomenon occurs in the vertical step of pre-straightening wherein the residual stresses are opposite or lower than that of the horizontal step at all peripheral angles. Development of residual stresses and their distribution at the peripheral angular positions of the bar in samples from the three evaluated steps is illustrated in Figure 5.6.

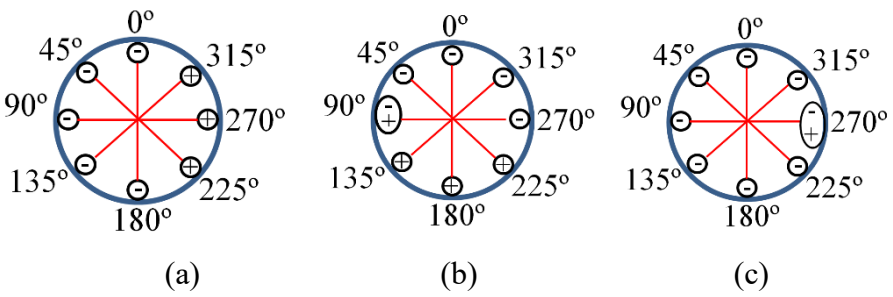

Figure 5.6: Schematic distribution of surface residual stresses at the peripheral angular positions: (a) in the raw material, (b) after horizontal and (c) vertical pre-straightening.

Pre-straightening is a continuous process that occurs with varying loads, consequently inducing non-homogeneous residual stresses due to different plastic strain along the axis of the bar, as seen in Figure 4.15 that shows residual stresses distribution over the cross section of the bar. The variation in residual stresses, measured by Neutron diffraction in the two cross sections of the vertical pre-straightening sample, expose the influence of the horizontal process in the residual stresses after the vertical step. Near the surface of the samples, large gradients of residual stress are present in the 90°-270° section, meanwhile the stresses in the center of the bar remain close to zero. As observed by Hirsch *et al.* (2013) and Dong *et al.* (2016), stress

variations like the difference between stresses at the 90º and 270º angular positions will generate distortions after heat treatment.

Besides, the non-homogeneities in the residual stresses at the peripheral angular positions and consequently from one side to the other of the bar, imposes to the pre-straightening sample a “high distortion potential” as explained by Nunes (2012).

The observed gradients of residual stresses, which reach almost 4 mm in depth, as seen in Figure 4.15 (b), can be attributed to a remaining bending from the raw material and to the contact of the bar with the horizontal rolls at the peripheral angles (90º and 270º). Furthermore, because of the plastic strains generated in the process, cold working leads to an increase in hardness and in FWHM measured values at the 90º and 270º surface peripheral angular positions, as shown in Figure 5.1. These facts reveal that the residual stresses generated in the process chain are more influenced by horizontal pre-straightening than by vertical pre-straightening, which is expected giving the original curvature of the coil in the horizontal plane.

The raw material, the horizontal pre-straightening bar, the vertical pre-straightening bar and wire drawing bar show non-homogeneous residual stresses near the surface, as it can be observed in Figure 4.5, Figure 4.9, Figure 4.14 and Figure 4.19 respectively. The instability in residual stress near the surface is more evident at the peripheral angles of 0º, 90º, 180º and 270º due to the higher demand imposed by the processes at those angular positions. Figure 5.7 (a) shows the average residual stresses of raw material (RM), after horizontal pre-straightening (HPS), vertical pre-straightening (VPS) and wire drawing (WD) compared with the residual stresses measured by Krause *et al.* (1978) showed in Figure 5.7 (b). Krause *et al.* show non-symmetric values of residual stresses with tensile and compressive stress at the peripheral angles. When the gradients of experimental residual stresses (Figure 5.7 (a)) are calculated, it is evident the differences between the peripheral angles. The gradient of the stress values were calculated subtracting the stress value from the angle pairs in each process and the results are shown in Table 5.1. A difference of more than 200 MPa is found in the raw material if the gradient of stress (Table 5.1) is evaluated. This difference in the stress between the opposite angles on the surface is carried in the following process and reaches more than 100 MPa at wire drawing process. This influence of the stress gradient shows that the stress is not superimposed from one process to another having, thus, a “memory effect” discussed by Nunes (2012). This “memory effect” is related to the amount of deformation to which the material is submitted during the process chain and this fact leads to distortions in the final product.

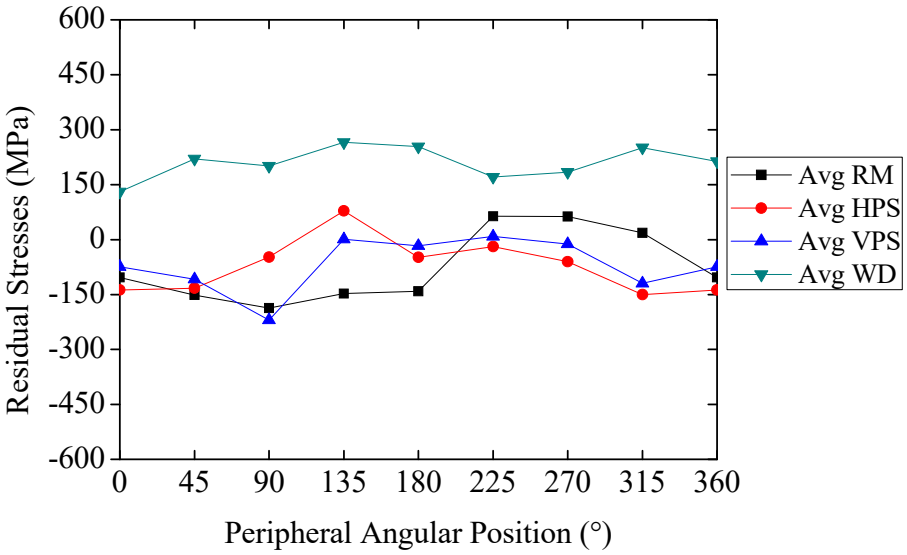

(a)

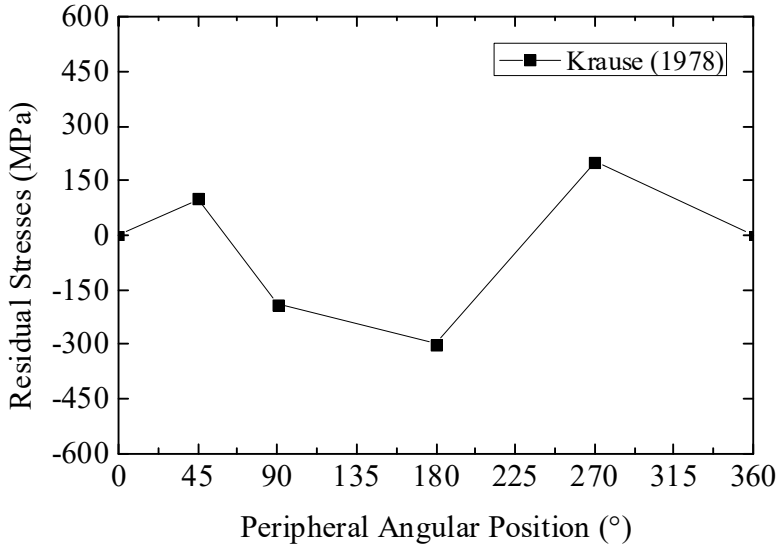

(b)

Figure 5.7: (a) Average of residual stresses measured by X-ray diffraction at surface peripheral angular positions and (b) residual stresses from roller straightening by Krause *et al.* (1978). Source: (a) Own; (b) adapted from Krause *et al.* (1978).

Table 5.1: Gradient of residual stresses of process chain at peripheral angular positions

Angle	**RM (Δσ)**	**HPS (Δσ)**	**VPS (Δσ)**	**WD (Δσ)**
0-180	37.4 MPa	-88.9MPa	-56.9 MPa	-123.2 MPa
90-270	-249.5 MPa	12.6 MPa	-207.9 MPa	16.4 MPa

5.2 COMPARISON BETWEEN EXPERIMENTAL AND NUMERICAL RESULTS

In this section a comparison between the experimental and simulation results concerning to strains, hardness and residual stresses are shown.

5.2.1 Strains and hardness

Strain distribution on the surface of the simulated horizontal pre-straightened bar (Figure 4.24) shows disparity from one side to the other along the length of the bar. The disparity between different sides of the bar leads to a distortion potential at the end of the process (ATIENZA *et al.*, 2005).

In Figure 5.8, it is possible to compare experimental values of hardness, FWHM and simulated equivalent plastic strains relative to samples from different steps of the process chain at each peripheral position of the bars. Samples subjected to experimental measurements are from the raw material (RM), after horizontal pre-straightening (HPS) and after vertical pre-straightening (VPS). The varying values of hardness and FWHM at each peripheral angle of the bar are associated with the interaction between the bar and the rollers during each process.

FWHM values, showed in Figure 5.8 (a), are a function of the distribution of the randomly oriented lattice plane distances due to 3rd order residual stresses, as well as of the size of coherently diffracted domain (HAUK, 1997). FWHM values can be used to characterize work hardening in the material and to make correlations with hardness measurements (HAUK, 1997; NALLA *et al*., 2003).

A 10% increase in hardness was recorded at the 270º peripheral angular position when the material was submitted to the vertical straightening process, as shown in Figure 5.8 (a). In contrast, hardness between horizontal and vertical pre-straightening processes remains the same at the 90º angular position in the vertical process. The increase in hardness at the peripheral angles of 90° and 270° is due to the contact of the bar with the rolls during the horizontal pre-straightening process. For the RM state, the bar touches the coil at 90° during uncoiling, while the 270° position is under tension load, which explains the higher value of FWHM at these two peripheral angles.

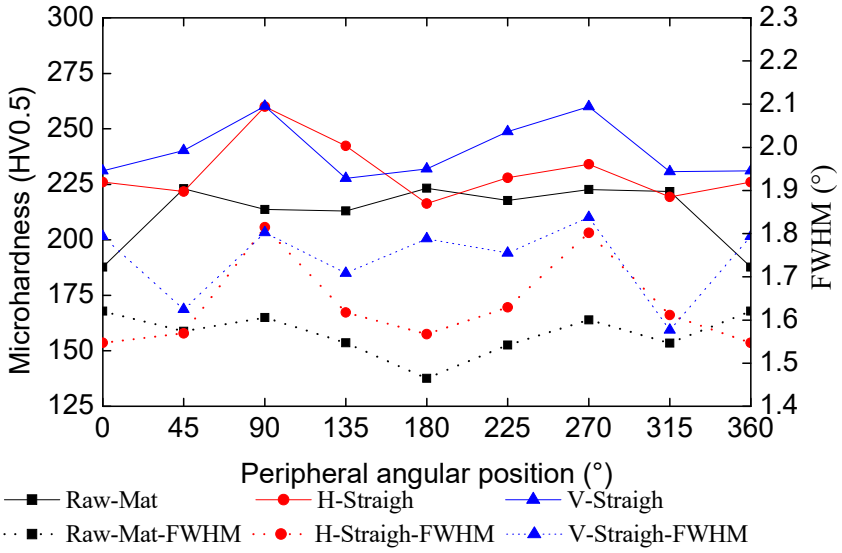

(a)

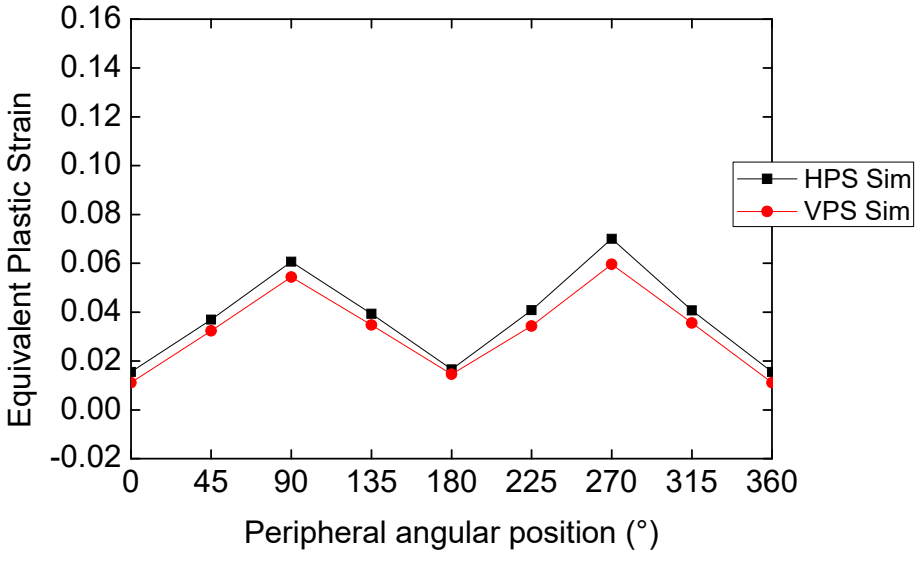

(b)

Figure 5.8: (a) Experimental hardness and FWHM and (b) equivalent plastic strains.

Data for the equivalent plastic strains plotted in Figure 5.8 (b) were collected after the bar exits the rolls set of each process. At the angular positions of 90° and 270°, strains are more than 25% greater than that at other angles. This indicates that the horizontal set of rolls, which touches the bar at the 90º and 270º positions, is more severe related to the strains in those angles. As the processes generate compressive and tensile strains in the same time in different peripheral angles, the differences seen in Figure 5.8 (b) are the real strain due to the vertical process. The equivalent plastic strains are referent to the sum of strains from both horizontal pre-straightening and vertical pre-straightening.

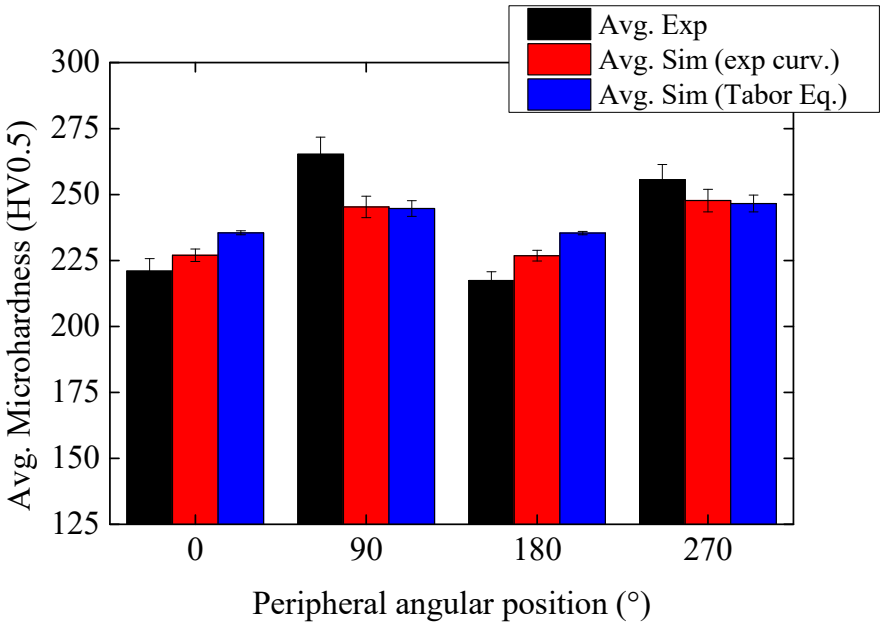

Figure 5.9: Experimental hardness compared to hardness determined from simulated equivalent plastic strains after horizontal pre-straightening.

Figure 5.9 presents the average Vickers Hardness from experimental and numerical results, in which the equivalent plastic strains were converted into hardness values by using the experimental curve to convert strain in hardness and the Tabor equation (Equation 4.1). As it can be observed, the deviation in hardness at the angles of 90º and 270º with respect to that at other angles is also noticeable in the numerical results. Hardness at the 90º and 270º positions are 10% higher than that at the 0º and 180º positions. The maximum variation between experimental and calculated hardness does not exceed 10%. This difference can be explained due to numerical model simplification, as well as the material segregation that was not considered into the modelling.

5.2.2 Residual stresses

The average values of experimental measurements of residual stresses after horizontal pre-straightening are plotted in Figure 5.10 together with the average of numerical results. Shape and amplitude of the curves were similar between experimental and numerical results. The maximum residual stress was recorded at the 135º peripheral angular position during the experimental test, whereas the maximum residual stress corresponded to the 90º position in the simulation. Meanwhile, the minimum residual stress was associated with the 315º and the 270º positions in the experimental test and simulation, respectively. The discrepancy between

positions corresponding to peak values could be due to the restraints imposed to the bar as boundary conditions in the simulation. As a result, the bar could not move freely as in the real process due to the movement of the elements in the beginning of the bar that were restricted to one axis in order to drive the bar from one process to another. In addition, the simulation model did not consider a continuous process with a completely coiled initial raw material. All this factors in the input of simulation parameters influence in the final results of residual stresses and strains in the simulated bar.

Differences between simulated and experimental residual stresses can be further attributed to irregularity in geometry along the raw material, which cross section does not follow a perfect circular shape (HIRSCH *et al.*, 2014; de SOUZA, 2017).

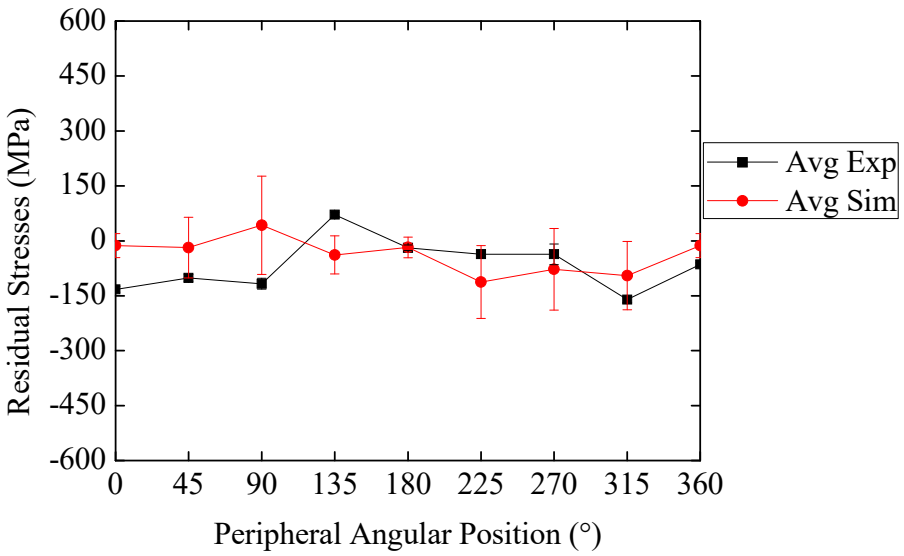

Figure 5.10: Residual stresses on the surface of the horizontal pre-straightening bar by experimental measurements and simulation.

Figure 5.11 shows the variations in the diameter of the raw material measured in different positions along the longitudinal axis. The diameter of the bar is not constant if the angular positions such as 0º-180º are evaluated in different position in the length. For this reason, for the simulation the geometry of the bar was modelled as circular.

Figure 5.12 illustrates the residual stresses obtained by Neutron Diffraction and that from simulation in the 90º-270º cross section of the horizontal pre-straightening bar, where a similar behavior can be observed.

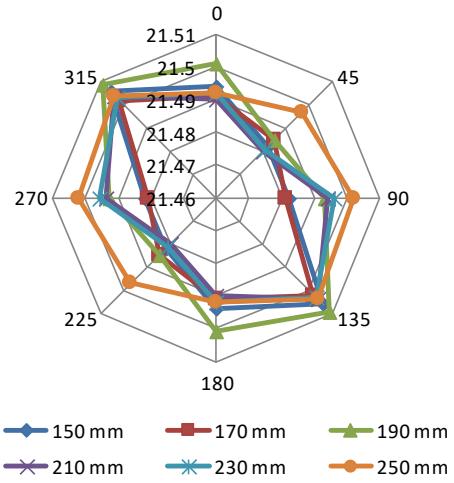

Figure 5.11: Variation in diameter of the raw material bar along the length.

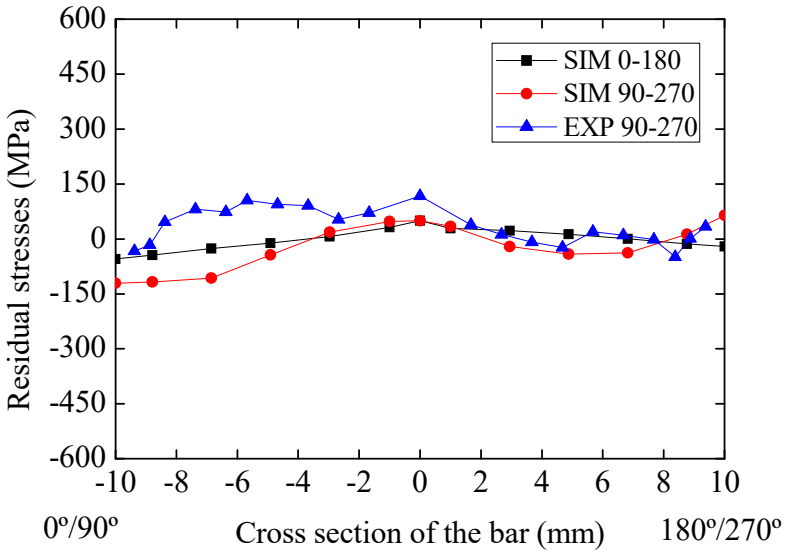

Figure 5.12: Experimental residual stresses plotted against simulation results in the cross sections of the horizontal pre-straightened bar.

The simulated profile of residual stresses in the 0º-180º cross section is depicted in Figure 5.12 as well. The stress values in this section are close to zero near the center of the bar and assume a compressive magnitude of around -50 MPa near the edges on both sides (0º and 180º peripheral angular positions). When the bar cross through a bending process, basically there is a formation of two zones: a plastic zone in the surface layers of the bar and an elastic zone in the core of the bar. The plastic zone influences directly the formation of residual stresses at the surface and it is possible to explain the differences found in the experimental profile of residual stresses shown in Figure 5.11. On the other hand, at the elastic zone there is no

generation of plastic deformation, however, the residual stresses at this zone might be redistributed (YOSHIDA *et al.*, 2010 *apud* NUNES, 2012).

Besides, it is worth keeping in mind that the bar was modelled as perfectly round and perfectly positioned, restrained against rotation and against out-of-plane translation, and that these assumptions could alter the resulting residual stresses in particular peripheral angular positions. Furthermore, the distance between the coil and the guide rolls was reproduced in the model with a reduced scale in order to minimize the required computational time.

In Figure 5.13, it is possible to compare the FWHM and the axial plastic strains (PE) in the 90º-270º cross section taken at the 200 mm axial position of the horizontal pre-straightened bar. A non-homogeneous curve characterizes the FWHM with higher values near the surface than in the core of the bar indicating that the strains are also higher on the surface and this fact is seen in the simulated plastic strain curve. On the other hand, the resultant simulated plastic strain has a homogeneous profile.

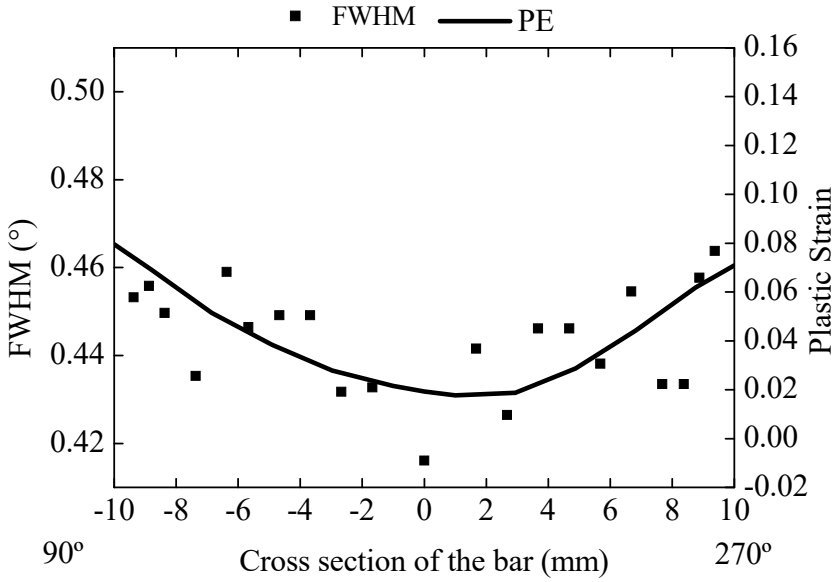

Figure 5.13: FWHM by Neutron diffraction and simulated plastic strains (PE) in the cross section of the horizontal pre-straightened bar.

Figure 5.14 presents the average values of residual stress evaluated after vertical pre-straightening, according to simulation and to experimental measurements by X-Ray diffraction. In the numerical model, part of the observed residual stresses is generated by uncoiling at the beginning of the two consecutive straightening processes. The maximum difference found between experimental and simulation was found at the peripheral angle 270º (273 MPa). On the other hand, the peripheral angular position 90º shows no difference between experimental

and simulation. The simulation procedure involves the input of as many parameters from the real process as possible. Among these parameters are the microstructure data, stress v. strain curve considering the anisotropy of the material and previous wire rod manufacturing process information such as the state of deformations of the wire rod. The data used in the simulation of the current study has considered the informations of the process chain after uncoiling with a material free of initial stresses. Besides that, it has not considered the Bauschinger effect, which according to Toribio *et al.* (2020) can lead to variations on the effective stress of the material. Thus, the simulated residual stresses shown in Figure 5.14 are due to an almost perfect condition of the material and for this reason, there is no variation ($\Delta\sigma$) between the opposite angles as 0º and 180º and 90º and 270º. On the other hand, this almost perfect condition does not happen at the experimental procedure, where there are microstructure variations and a previous state of residual stresses. Moreover, according to Dagnese (2012) the Bauschinger effect cannot be neglected.

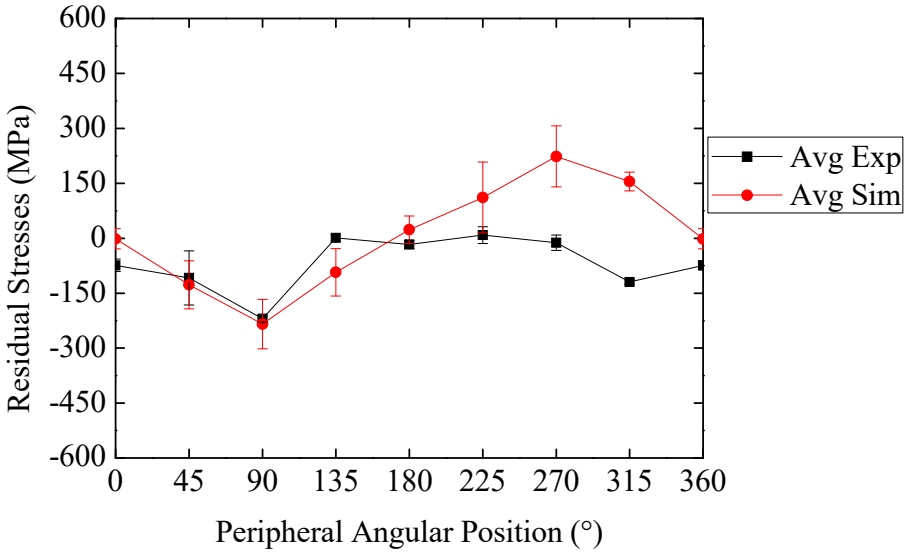

Figure 5.14: Residual stresses on the surface of the vertical pre-straightened bar by experimental measurements and simulation.

In the horizontal pre-straightening process, the regions from 45° to 90° and from 225° to 270° of the bar are in contact with the rolls. According to Das Talukder & Singh (1991), the main mechanisms of residual stress generation in the pre-straightening process are associated to the moment applied to the component and the contact between the bar and the tool. Thereby, the observed behavior of the residual stresses at the mentioned regions shows the influence of the coil shape on the distribution of surface residual stresses.

Figure 5.15 illustrates the variation in diameter at the angular peripheral positions along the length of the horizontal pre-straightening bar. A variation of 0.65 % in the diameter is exhibited in the 90º-270º section if compared with the 0º-180º section due to the acting of the horizontal pre-straightening rolls. This variation should be analyzed keeping in mind that the reduction in the drawing process is 10% (about 1.15 mm). The variations in the bar diameter, according to Hirsch *et al.* (2014), cannot be disregarded as a potential modifier of residual stresses. Parameters such as material manufacturing, initial peripheral shape containing considerable discrepancies in diameter among the angular positions and along the length of the bar, and position along the bar relative to the coil can alter the final residual stresses (WANG & GONG, 2002; RUUD, 2002; FISCHER & SCHLEINZER, 2002). The influence of these factors on the residual stresses still requires a deeper investigation, which could improve the accuracy of the simulation proposed herein.

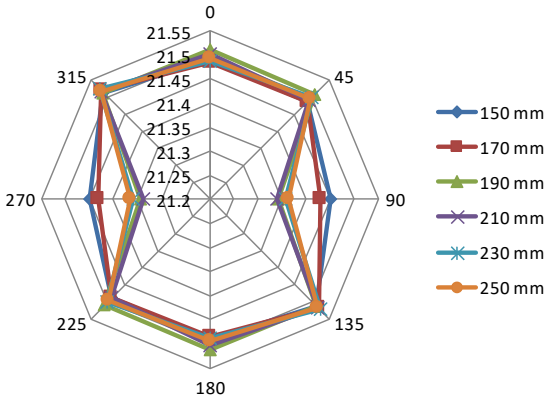

Figure 5.15: Variation in the diameter of the horizontal pre-straightening bar along the length.

Figure 5.16 shows the residual stress profiles measured by Neutron Diffraction and simulated in the 0º-180º and 90º-270º cross sections of the vertical pre-straightened bar. Residual stresses in the 0º-180º section are similar between the experimental and numerical results. There are some differences between the experimental profile and the simulated profile in the core due to the influence of the material segregation, not simulated in this work.

In contrast, differing values of residual stresses can be observed in the 90º-270º section. Although the 90º angle exhibits the same value of stress (-200 MPa compressive), the numerical results at the 270º angle show a stress value that is three times greater than that from the experimental results.

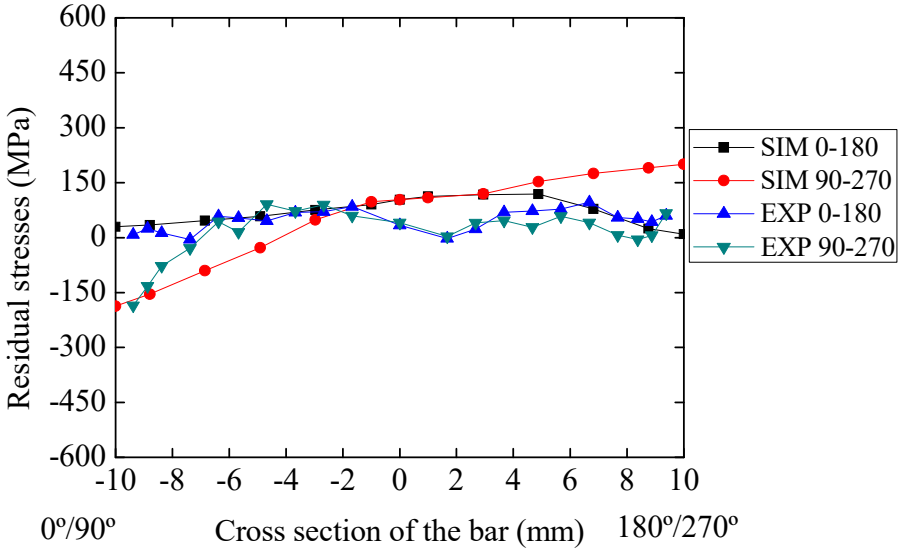

Figure 5.16: Residual stress profiles in the cross sections of the vertical pre-straightening bar from experimental test and simulation.

The average of residual stresses measured by X-ray diffraction and recorded in the simulation of the wire drawing process are shown in Figure 5.17. The amplitude of the residual stresses in the profile varies from simulation to the experimental measurements.

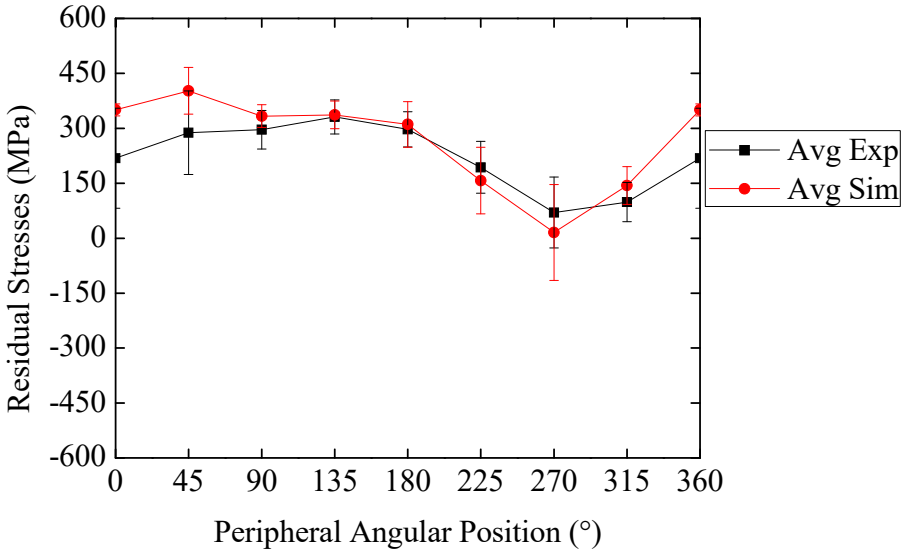

Figure 5.17: Surface residual stresses after wire drawing process from experimental measurements and simulation.

The greater difference in residual stresses between experimental and numerical results after wire drawing process at the peripheral angular positions was found at the peripheral angle of 0º (132MPa) as shown in Figure 5.17. According to Nunes (2012) the non-homogeneous

stresses generated in the pre-straightening process are maintained throughout the process chain. Thus, this difference noticed after wire drawing might be due to the influence of the vertical pre-straightening, where the rolls touch the bar at 0º angular position.

Figure 5.18 shows a comparison between a profile of an experimental residual stresses by Neutron Diffraction (DIAS *et al*, 2017) measured only in the 0º-180º section and four profiles of simulated residual stresses in the cross section of the drawn bar. Two profiles are from numerical results performed considering the first part of the process chain contemplating uncoiling and the subsequent processes of the chain, *i.e.*, horizontal and vertical pre-straightening, in two cross section: 0º-180º and 90º-270º. Furthermore, two more curves are shown in Figure 5.18 from previous simulations of the wire drawing process, without the consideration of preceding processes, performed by Soares (2012), considering the isotropic and the anisotropic data for the simulation.

Analogously to the residual stresses on the axial surface of the drawn bar, the stresses in the cross-section exhibit variations along the depth. The deviation of residual stresses in the center of the bar from the experimental test from the results of the simulation considering the preceding process (referred to as “SIM 0-180” and “SIM 90-270” curves in Figure 5.18) is about 200 MPa for both curves. If the experimental profile is compared with the profile of residual stresses from the previous isotropic simulation of drawing process (SIM-Drawn Isotropic), without the consideration of preceding processes, the differences in the core are even higher reaching 660 MPa. If the anisotropic simulation of the wire drawing (SIM-Drawn Anisotropic) is compared with the experimental, the difference reaches 500 MPa in the core of the bar.

According to Zottis (2013) material characteristics such as flow curve, anisotropy indices and kinematic hardening have strong influence on the magnitude of the simulated residual stresses after wire drawing. Besides, Zottis also highlighted the importance of the pre-straightening process in the simulation of the wire drawing. A curved bar increases the drawing force and the non-homogeneity in the distribution of residual stresses is increased as well. Thereby, the results shown in Figure 5.18 confirm the strong influence of the pre-straightened process in the residual stresses after wire drawing. Thereby, the results in Figure 5.18 shows that the consideration of the preceding processes combined with the use of an anisotropic material in the analysis yields a better match between simulated and experimental residual stresses.

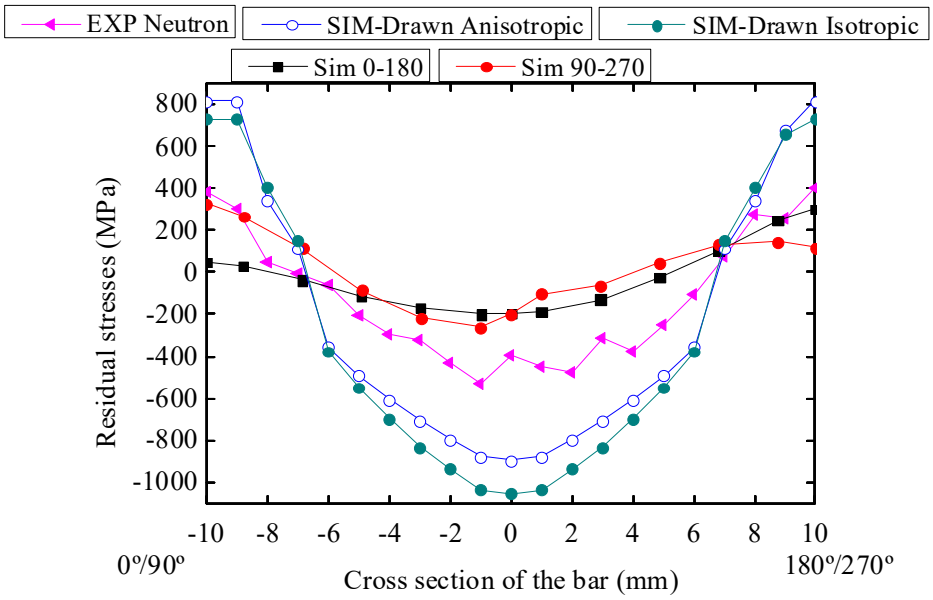

Figure 5.18: Experimental and simulated residual stresses in the cross sections of the drawn bar. Source: Adapted from Soares (2012), Dias *et al*. (2014)

5.3 ROLLS SETTINGS FOR PROCESSING IMPROVEMENT

Based on the experimental and after validating the numerical results through the comparison between experimental and simulation, a new positioning of the horizontal pre-straightening rolls was proposed. According to Hutton (2004) after a validation of the model, the process could be tested using simulation without the use of prototypes of experimental tests. In this section, two new arrangements named as Setting 1 and Setting 2 for the horizontal pre-straightening rolls are presented. Besides, the residual stresses and strains after horizontal pre-straightening, vertical pre-straightening and wire drawing are evaluated.

5.3.1 Horizontal + vertical pre-straightening: Setting 1

Figure 5.19 illustrates the residual stresses along the length of the bar obtained from simulation of Setting 1, which is the set of rolls shown in Figure 3.23. As it can be observed, the values of residual stresses varied significantly with the angular position.

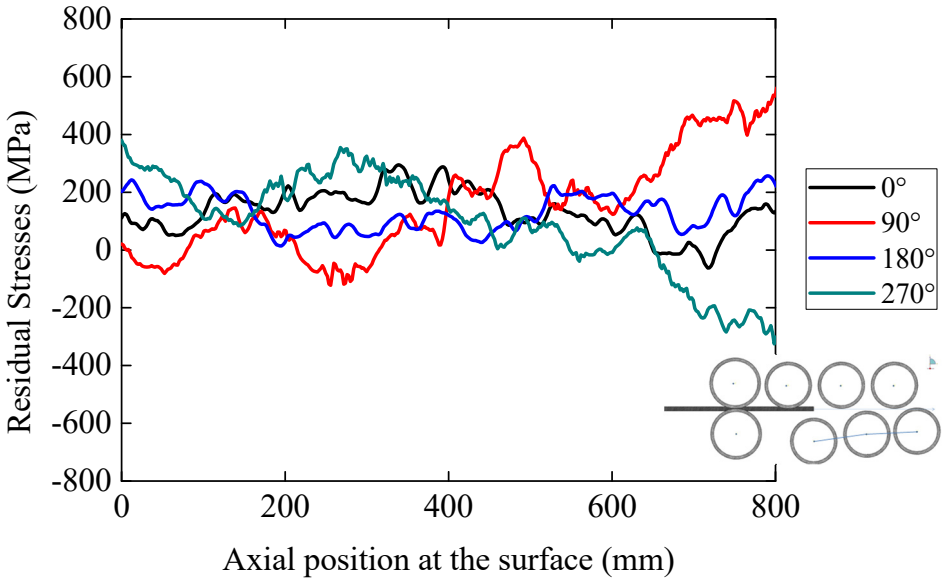

Figure 5.19: Residual stresses along the length after horizontal pre-straightened bar from simulation using Setting 1.

At the 90º position in Figure 5.19, the bar experienced a high tensile stress of 510 MPa corresponding to 800 mm axial position. The lowest compressive stress value was found in the 750 mm axial position at the 270º angular position (-325 MPa). The curves corresponding to

the 0º and 180º angular positions also presented considerable variation of stress along the length of the bar. The 180º curve reached the maximum value at the end of the bar, with a value of 220 MPa. On the other hand, the maximum value at the 0º angular position corresponded to the middle of the surface length and to a tensile stress of 250 MPa.

Figure 5.20 shows the equivalent plastic strain and maximum plastic strains along the length after horizontal pre-straightened bar for setting 1.

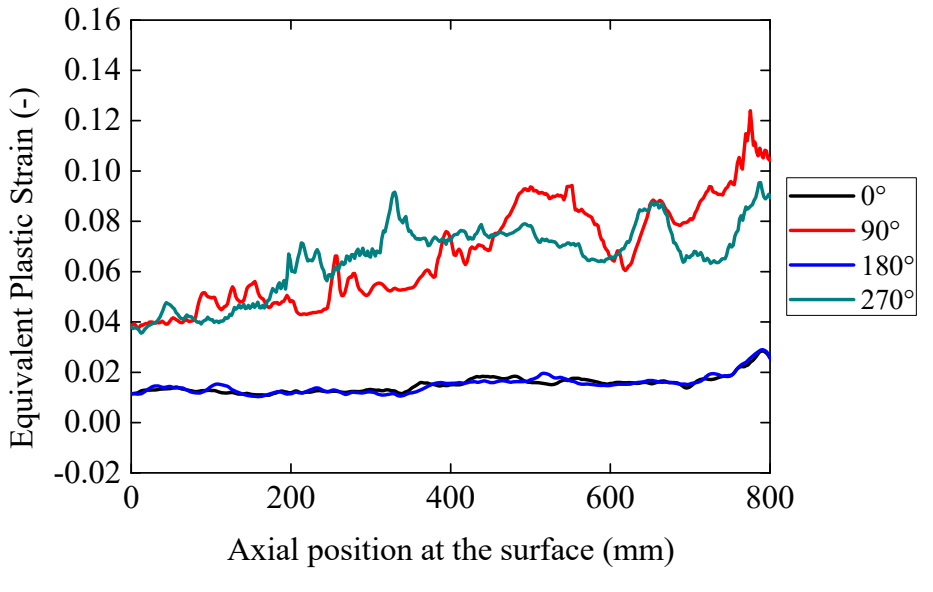

(a)

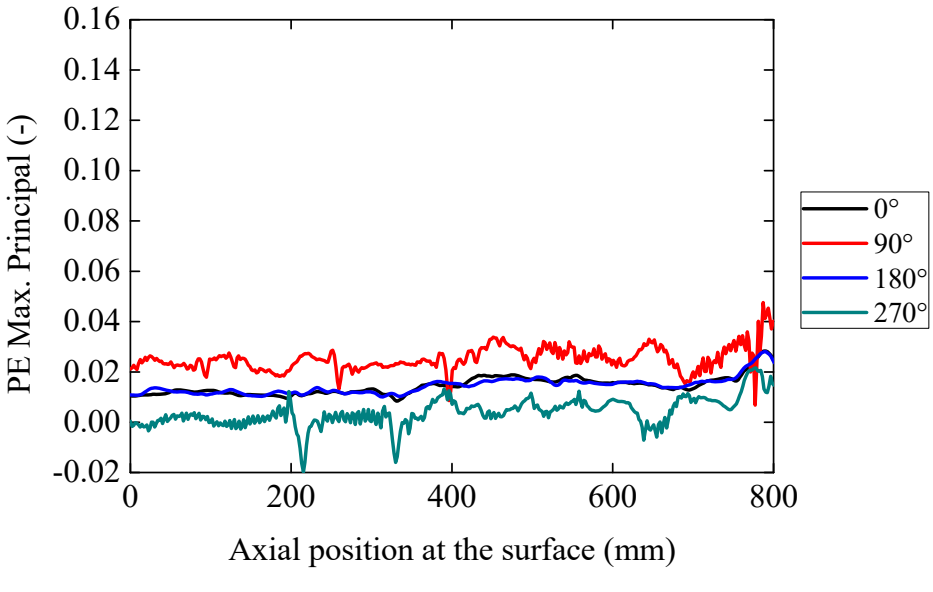

(b)

Figure 5.20: Simulation using Setting 1: (a) Equivalent plastic strains distribution and (b) maximum plastic strains along the length after horizontal pre-straightened bar.

In addition to residual stresses, the evaluation of using Setting 1 involved assessment of strain distribution at the main peripheral angular positions along the surface length of the bar. Figure 5.20 (a) shows the equivalent plastic strains along the surface, where higher strains can be observed in the 90º and the 270º curves, which are attributed to the contact of these angular positions of the bar with the horizontal rolls. The equivalent plastic strains on the surface of the straightened bar reach 0.124 at the 90º position in the final portion of the bar. Given the low action of the horizontal rolls at the 0º and 180º positions, strains at these positions remain lower than 0.026 along the entire length of the bar. Figure 5.20 (b) illustrates the principal maximum plastic strains along the length of the bar, which has homogeneous behavior than the equivalent plastic strains, with lower values registered along the surface.

Figure 5.21 illustrates the simulated surface residual stresses along the surface length after vertical pre-straightening. The maximum and minimum stress values were both found at 270º, equal to 600 MPa at 200 mm and to -530 MPa at 600 mm.

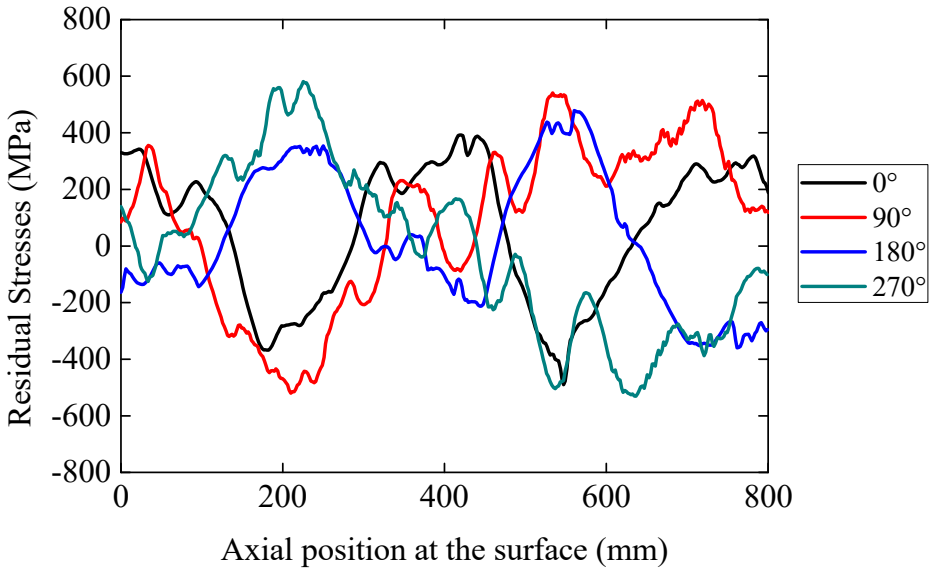

Figure 5.21: Residual stresses along the length of the bar after vertical pre-straightening.

Figure 5.22 shows strain profiles resulting from simulation after vertical pre-straightening. The equivalent plastic strain distribution (Figure 5.22 (a)) has shown similar behavior for the 90º and 270º angles, and same behavior and magnitude of strains for the 0º and 180º curves. The maximum value of equivalent plastic strain was found at the 90º angular position, equal to 0.11. The principal strains, presented in Figure 5.22 (b), are close to zero, with the maximum value of 0.032 achieved at the 90º position.

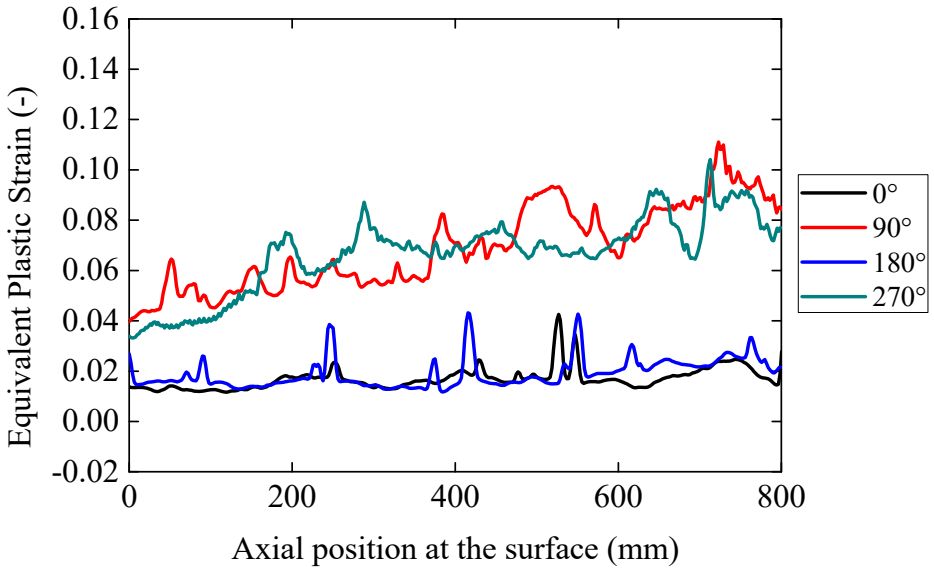

(a)

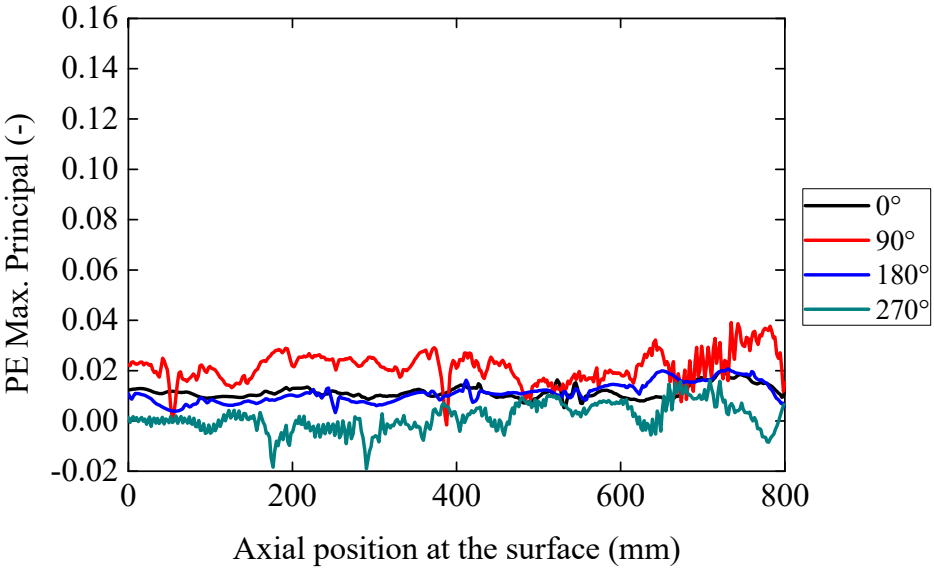

(b)

Figure 5.22: (a) Equivalent plastic strains distribution and (b) maximum plastic strains from simulation after vertical pre-straightening.

5.3.2 Horizontal + vertical pre-straightening: Setting 2

Figure 5.23 shows the profile of residual stresses at the main peripheral angles along the surface of the bar, obtained from simulation considering Setting 2 for the layout of horizontal pre-straightening rolls shown in Figure 3.24.

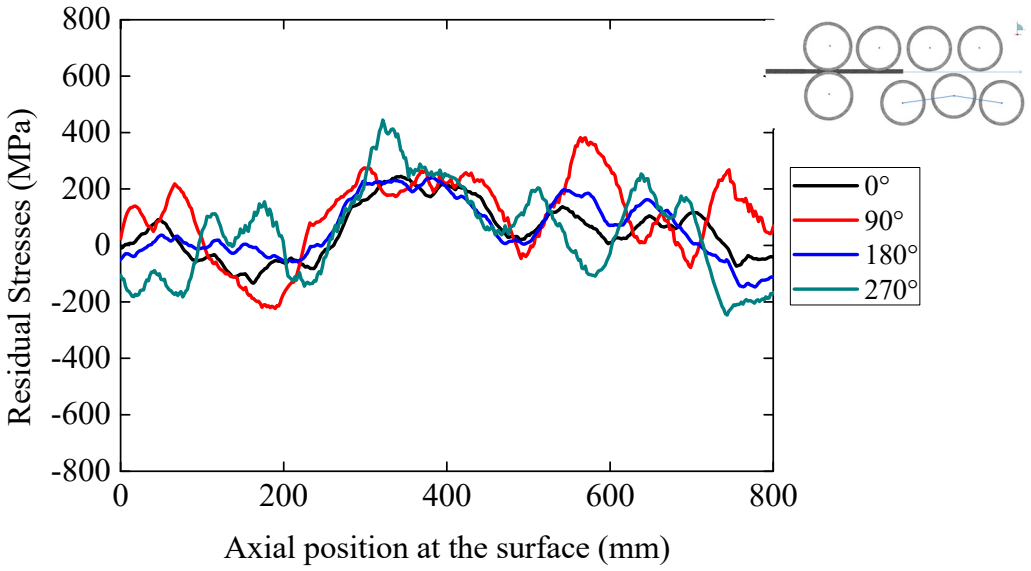

Figure 5.23: Residual stresses along the length after horizontal pre-straightened bar from simulation using Setting 2.

No significant variation was observed in Figure 5.23 between the pairs of opposite angles (0º-180º and 90º-270º). Residual stresses at all peripheral angles and along the entire length of the bar range from 200 MPa and -200 MPa, with the exception of the interval 300-600 mm, where residual stresses reach 420 MPa tensile at 270º and 360 MPa tensile at 90º.

When comparing the residual stresses along the surface of the horizontal pre-straightened bar resulting from employing Setting 2 (Figure 5.23) to that obtained when using Setting 1 (Figure 5.19), opposite behavior between the two can be observed. At the initial portion of the bar, Setting 2 shows compressive stresses up to almost half of the surface length, while Setting 1 shows tensile residual stresses in the same region. Residual stresses were compressive along almost the entire surface length of the bar when Setting 2 was used, which does not occur in Setting 1.

Figure 5.24 (a) shows the equivalent plastic strains along the surface length at the four main angular positions. The 90º and the 270º curves show higher strain values when compared to that of Setting 1 due to the contact with the horizontal rolls.

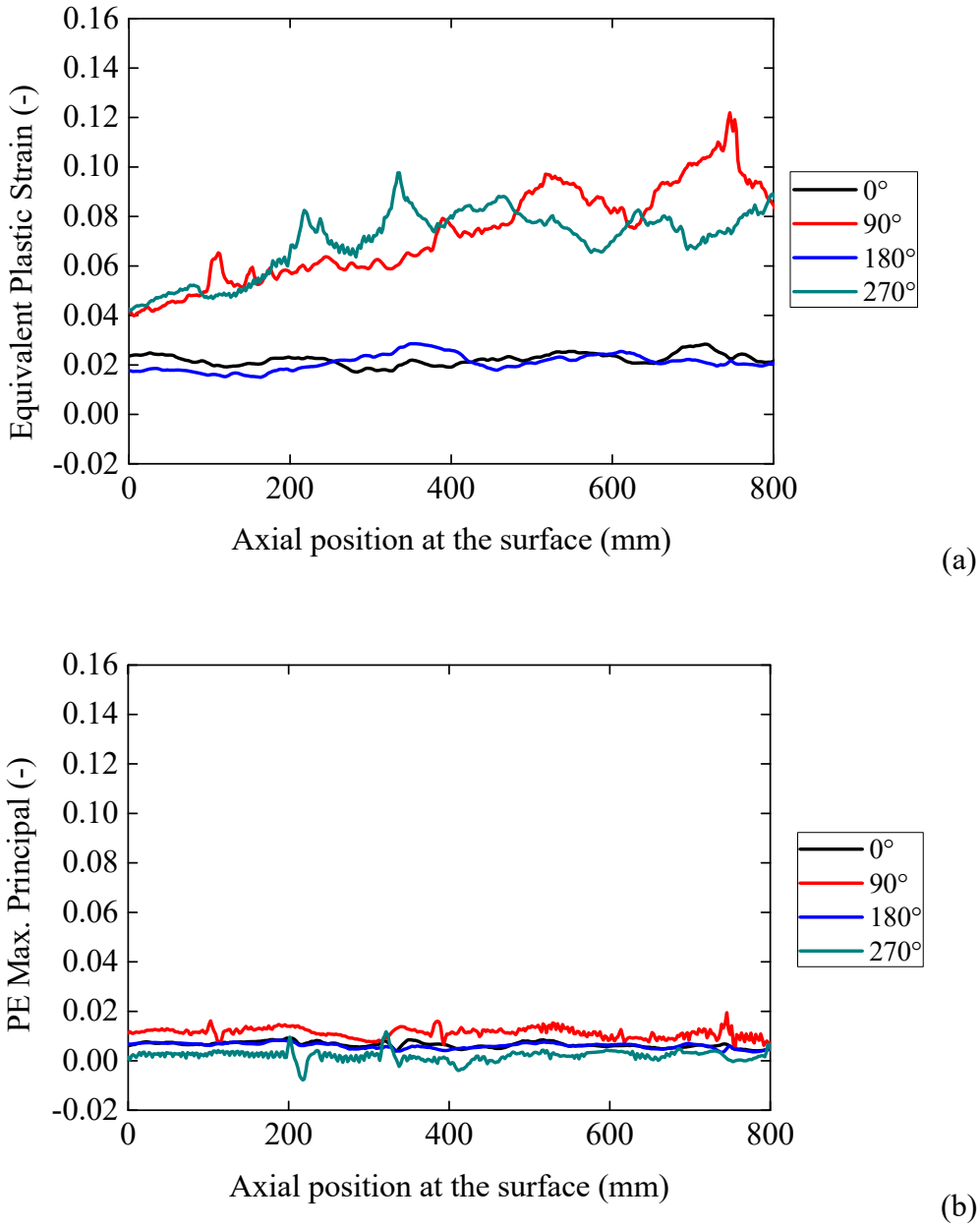

Figure 5.24: Simulation using Setting 2: (a) Equivalent plastic strains distribution and (b) maximum plastic strains along the length after horizontal pre-straightened bar.

The equivalent plastic strains reach 0.12 at the 90º position in the final portion of the bar, which is 3% lower than the strain found in the simulation of Setting 1. Strains at the 0º and 180º angles remain lower than that recorded at 90º and 270º along the entire surface, not exceeding 0.028. The principal maximum plastic strains, presented in Figure 5.24 (b), has shown a homogeneous behavior along the entire surface of the bar, contrasting with the ascending curves of equivalent plastic strains recorded at the 90º and 270º peripheral positions. This fact also happened in the simulation of the real process.

Figure 5.25 shows the residual stresses at the four main peripheral positions along the surface length of the bar from simulation employing Setting 2. Residual stresses remain compressive along the entire bar surface, with a minimum value of -600 MPa at the 90º peripheral angular position right at the beginning of the bar. The maximum stress corresponds to the angular position of 270º and is approximately -150 MPa. Same behavior, similar to that of a wave, can be observed at all main peripheral positions.

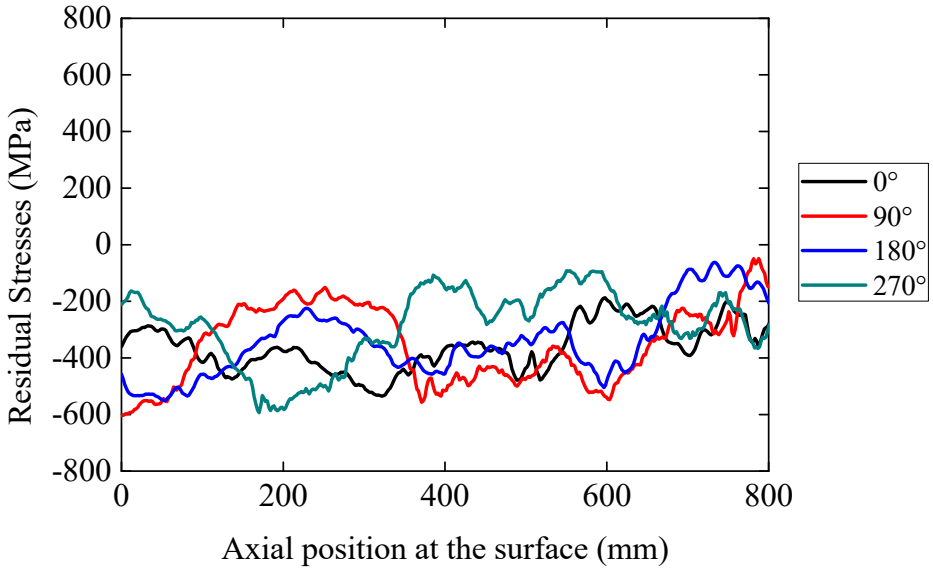

Figure 5.25: Residual stresses along the length of the bar after vertical pre-straightening from simulation.

The equivalent plastic strains resulting from Setting 2, plotted in Figure 5.26 (a), form more stable, linear curves than that of Setting 1, however with higher variation of strains between 90º and 270º. The maximum value of equivalent plastic strain (0.118) is reached by a single peak at the end of the bar. The principal maximum plastic strains, illustrated in Figure 5.26 (b), presented the same behavior as that of Setting 1.

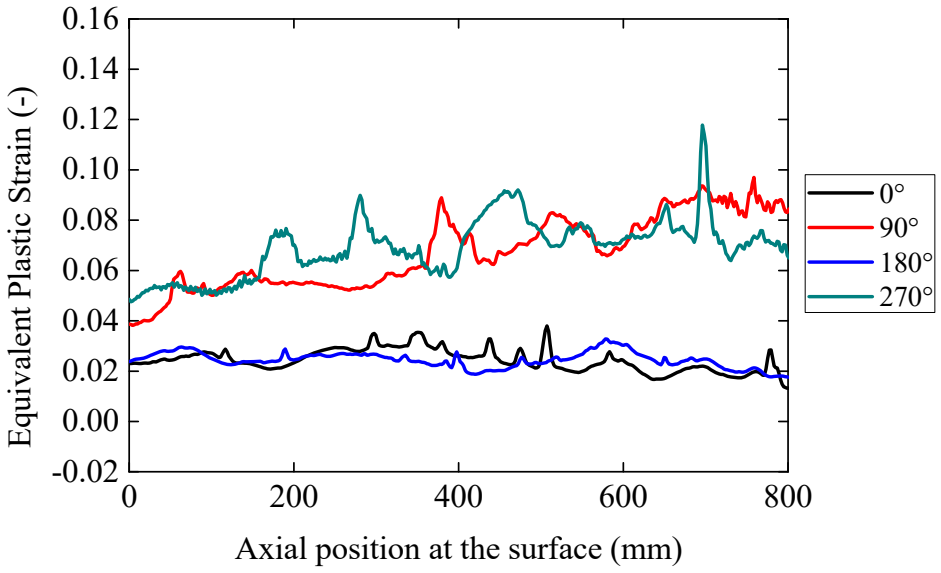

(a)

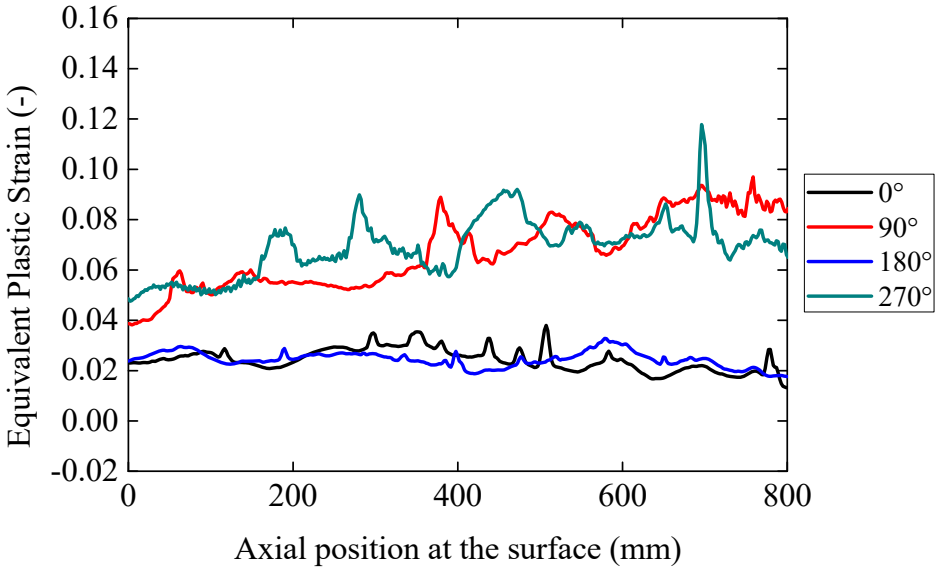

(b)

Figure 5.26: (a) Equivalent plastic strains distribution and (b) maximum plastic strains after vertical pre-straightening.

5.3.3 Comparison between Setting 1 and 2 after wire drawing

The altered positioning of the horizontal set of rolls were implemented in the analytical model and the final results from simulations are discussed in this section. Figure 5.27 shows the residual stresses at different angular positions on the surface along 800 mm length of the bar obtained from simulations considering Setting 1 (a) and Setting 2 (b).

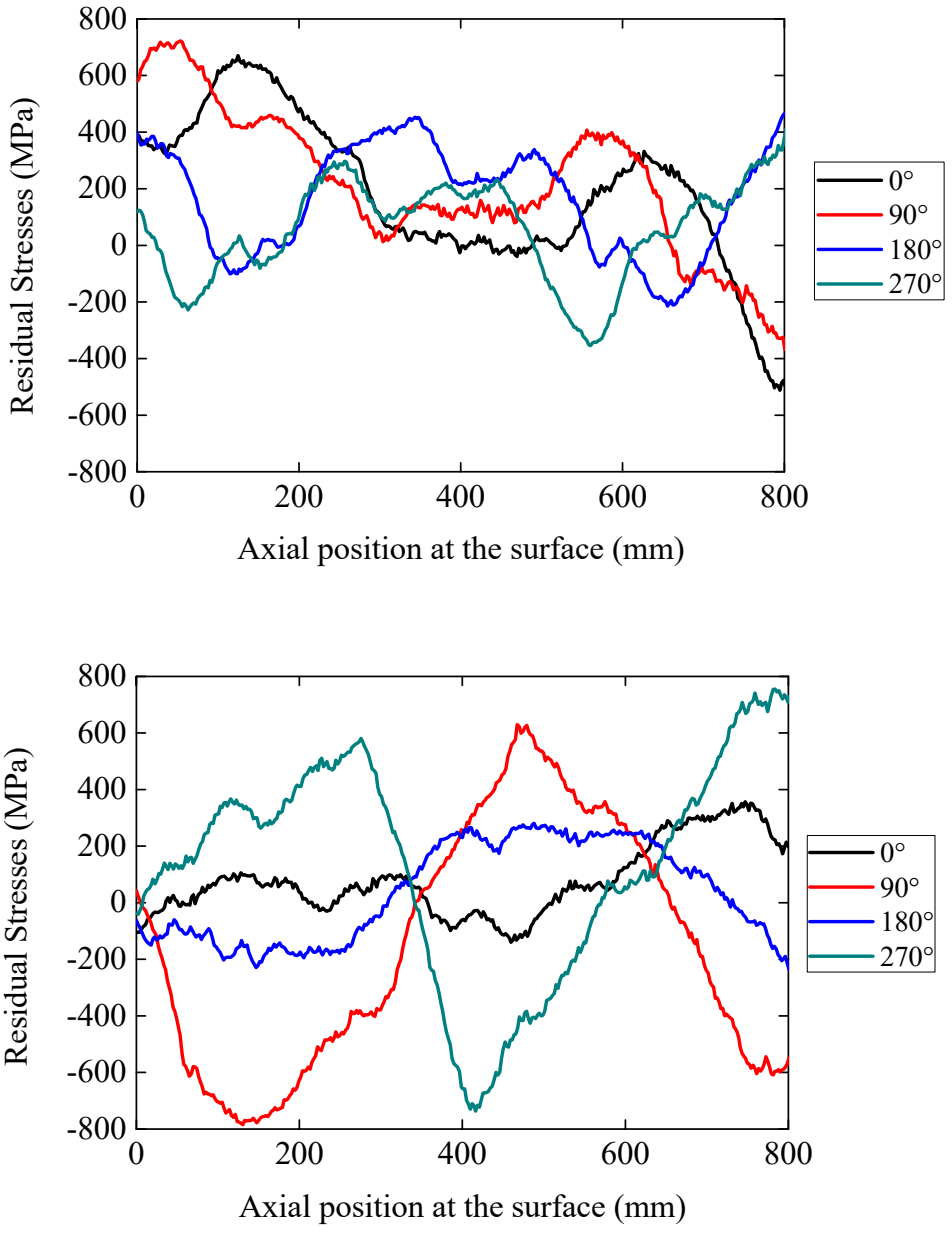

Figure 5.27: Residual stresses along the length of the bar after wire drawing from simulation using (a) Setting 1 and (b) Setting 2.

Residual stresses are non-homogeneous along the surface in both settings. Setting 1 (Figure 5.27 (a)) has shown a maximum residual stress of almost 800 MPa tensile at the 90º peripheral angular position and a minimum stress at the 0º peripheral angular position of -600 MPa compressive. Distinct behavior was observed in Setting 2 due to the change in the rolls positioning. In Setting 2, the minimum stress was equal to -800 MPa compressive, corresponding to the peripheral angular position of 90º, and the maximum stress was found at the peripheral angular position of 270º, with a value close to 800 MPa tensile.

Equivalent plastic strains are plotted in Figure 5.28 in terms of axial and peripheral positions. Strains are homogeneous along the initial 400 mm in Setting 1 Figure 5.28 (a)). Along the remaining 400 mm, strains show a variation at 90°, which goes from 0.19 to 0.29. On the other hand, Setting 2 (Figure 5.28 (b)) shows homogeneity of strains among the three peripheral angles and disparity at the 90º angle, where strains increase from 0.2 over the other angles to 0.24.

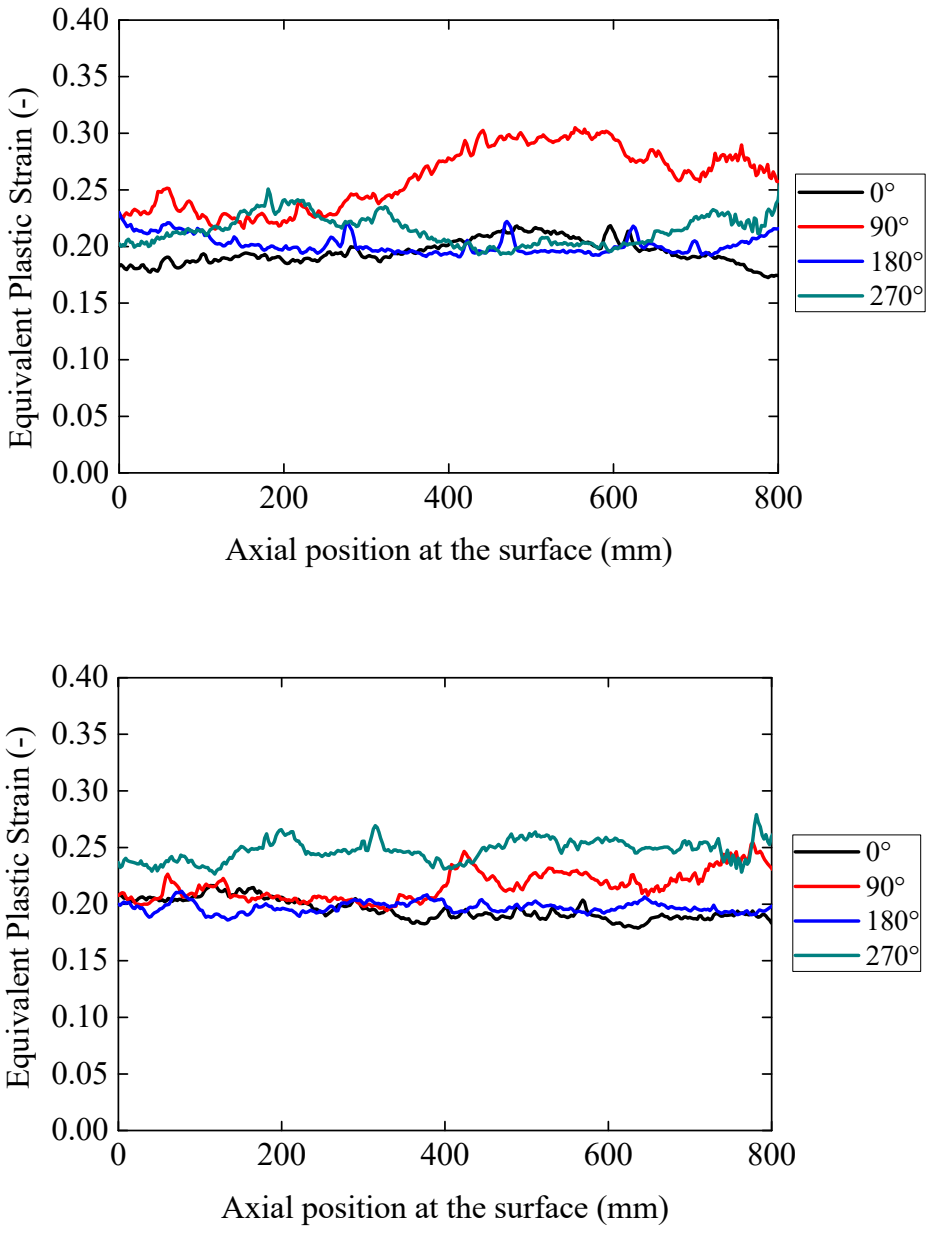

Figure 5.28: Equivalent plastic strains distribution from simulation after wire drawing using (a) Setting 1 and (b) Setting 2.

Equivalent plastic strains were, in all cases, greater in Setting 1 than in the original setting of horizontal pre-straightening rolls, reaching 76% higher strains at 0º. The smallest variation was found at the 270º position, where strains in the original setting were 40% lower than that of Setting 1. At the others peripheral positions, strains of Setting 1 were 65% and 71% greater than that of the original setting at 90º and 180º, respectively.

Same behavior was observed between the equivalent plastic strain curves of Setting 2 (Figure 5.24 (a)) and the original setting, showed in Figure 4.24a. In terms of magnitude of strains, 74% larger strains were recorded at the 0º peripheral position of Setting 2 when compared to the original setting. The discrepancy between the two setting is smaller at the other peripheral angles, corresponding to 63% larger strains of Setting 2 at 90º, 69% larger strains at 180º, and 41% larger strains at 270º, the smallest among all angles, when compared to the strains of the original setting.

The equivalent plastic strains recorded in the simulation, considering Setting 1, of vertical pre-straightening reached a maximum value 12% lower than that recorded in the simulation of the horizontal process.

The Figure 5.29 shows the distribution of equivalent plastic strain along the bar surface for the original configuration and the new configuration named setting 2. The setting 2 has shown homogeneous strain long the surface if compared with the setting 1 (Figure 5.28) and with the original configuration (Figure 5.29 (a)), turning the setting 2 the ideal to apply for the manufacturing of round bars.

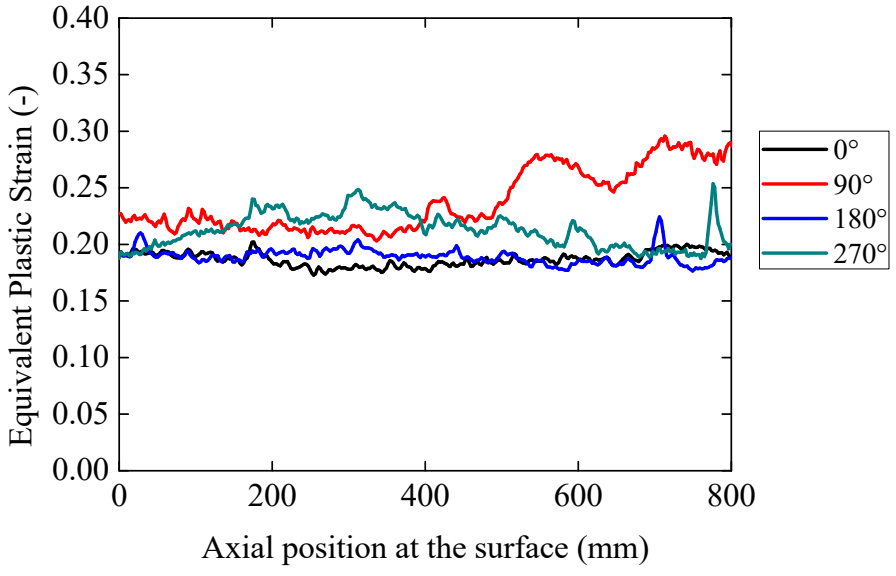

(a)

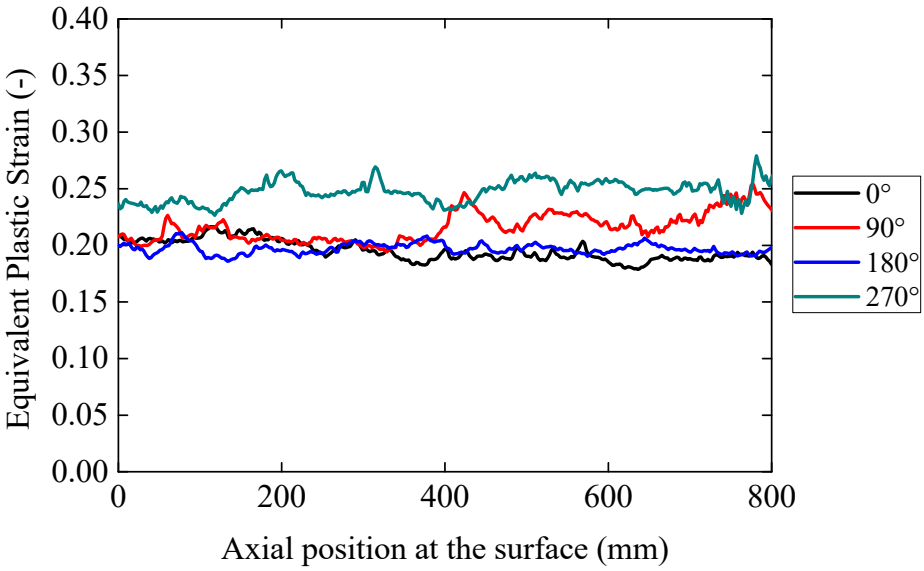

(b)

Figure 5.29: Equivalent plastic strains distribution from simulation using (a) real wire drawing process and (b) setting 2 after wire drawing.

6 CONCLUSIONS

The study presented herein characterized and simulated the industrial wire drawing process. The use of numerical simulation permitted the evaluation of residual stresses and strains along the bar surface resulting from new rolls configurations, which would not be economically feasible if experimental procedures were used. The analytical models employed in the study satisfactorily reproduced the material behavior captured during experimental tests, and the methodology used was proven to be an efficient tool for the analysis of the wire drawing process chain. The main conclusions of this study are listed below:

- The segregation in the central region of the bar directly influences the residual stresses and constitutes to a distortion potential on the bar;
- The residual stresses showed significant non-homogeneity at the peripheral positions on the surface of the bar in all steps including wire drawing;
- The strains generated in the bar were more influenced by the horizontal pre-straightening process than by the vertical step given the raw material curvature and the contact between the bar and the rolls;
- The strains recorded at the 90º and the 270º peripheral angular positions on the surface of the bar were more pronounced after horizontal pre-straightening and remained this way after the vertical straightening process;
- Residual stresses measurements have shown that the stresses are not superimposed by subsequent processes;
- Residual stresses generated at the horizontal pre-straightening are not equalized by subsequent processes and this characterizes the “memory effect” at the process;
- The strain vs. hardness response from the numerical analysis was in good agreement with that recorded during the experimental tests;
- The FWHM, hardness and simulated strain values have the same behavior in terms of peripheral angular positions;
- The residual stresses along the bar length from simulation of all evaluated steps of the process chain had non-homogeneous profiles in different peripheral angular positions;

- The simulation of distinct settings of rolls in the horizontal pre-straightening process yielded completely distinct residual stress surface profiles;
- The bending of the first couple of horizontal rolls influences the strain distribution after wire drawing. As the distance between the rolls decrease, more homogeneous is the distribution of strains;
- The control of the pre-straightening parameters assists the reduction of shape distortion;

Through the study, some influence factors of the pre-straightening and drawing processes were identified as:

- The geometry of both the wire rod section and the coil dimension has a direct influence on the heterogeneous strains and stresses generated in the peripheral region of the rod;
- The wire rod has movement restrictions along the chain that also influences the intensity of the stresses on the peripheral angular positions.

7 OUTLOOK

- Perform experimental tests using the proposed improvement positioning of pre-straightening;
- Simulate the wire drawing process chain considering the shot peening process in order to verify the influence of residual stress after wire drawing;
- Simulate the straightening process without the vertical pre-straightening process;
- Evaluate the influence of the number of rolls by using numerical simulation;
- Improve the storage of the bar by changing the shape of the coil.
- Consider Bauschinger effect in the simulations.

8 REFERENCES

ABAQUS/Standard User's Manual, Version 6.13. Providence, RI: Dassault Systèmes Simulia Corp, 2013.

ALTAN, T; VELAZQUEZ, V. "Numerical Process Simulation for Tool and Process Design in Bulk Metal Forming." *In* Annals of the ClRP, p. 599-615. Columbus, 1996.

APONTE, C. F. C. Utilização do Método dos Elementos Finitos no Desenvolvimento de Modelos de Corte de Material. Master dissertation. PUC-Rio, 2011.

ARAÚJO, A. C. "Análise Da Formação De Bandas De Cisalhamento Por Meio De Corpos De Prova De Tração Especiais". Master dissertation. UFMG, 2009.

ARBAK, E. *et al*. "Forging Simulation at Izeltas." *In*: 4th International Conference and Exhibition on Design and Production of Machines and Dies/Molds – CESME, 4. Turkey, 2007.

ASTM International. E92-16 Standard Test Methods for Vickers Hardness and Knoop Hardness of Metallic Materials. West Conshohocken, PA; ASTM International, 2016. doi: https://doi.org/10.1520/E0092-16

ATIENZA, J. M. "Tensiones Residuales En Alambres De Acero Trefilados". Tesis Doctoral. Universidad Politécnica de Madrid, 2001.

ATIENZA, J. M. *et al*. "Residual Stresses in Cold-Drawn Pearlitic Rods." Scripta Materialia 52, no. 12 (2005): p. 1223-28.

ATIENZA, J. M.; RUIZ-HERVIAS, J.; ELICES, M. The Role of Residual Stresses in the performance and Durability of Prestressing Steel Wires. Experimental Mechanics, v. 52, 2012, p. 881–893. doi 10.1007/s11340-012-9597-1.

BANABIC, D.; BUNGE, H. J.; PÖHLANDT, K.; TEKKAYA, A. E. Formability of Metallic Materials: Plastic Anisotropy, Formability Testing and Forming Limits. Berlin: Springer, 2000.

BHADESHIA, H. K. D. H. Material Factors. " *In*: Handbook of Residual Stress and Deformation of Steel. Canada: ASM International, 2002.

BÖLLINGHAUS, T. *et al*. Manufacturing Engineering. *In*: "Handbook of mechanical Engineering". p. 523-785, Springers, 2009.

BRUNDLE, C. R., EVANS Jr., C. A., WILSON, S., Encyclopedia of materials characterization: surfaces, interfaces, thin films. USA: Butterworth-Heinemann, 1992.

CARLSSON, B.; HUML, P. "Determination of the Material Properties of an Anisotropic Metal Wire." In Annals of the CIRP, p. 231-33, 1996.

CHEN, L. Numerical Analysis and Simulation of Stress Evolution in the Straightening Process of Different Heavy Rails. *Journal of Metallurgical Engineering (ME)*. V. 3, Issue 1, 2014, p. 43-47. doi: 10.14355/me.2014.0301.05

CULLITY, B. D.; STOCK, S. R. Elements of X-Ray Diffraction. 3ed. Edinburgh: Pearson, 2014.

DAGNESE, J. Análise do Comportamento Elasto-plástico de um Aço AISI 1045 em Baixas Deformações. Master dissertation: PPGE3M/UFRGS, 2012.

DAS TALUKDER, N.K.; SINGH, A.N. Mechanics of Bar Straightening .1. General-Analysis of Straightening Process. J. Eng. Ind-T ASME. 1991;113(2):224-7. http://dx.doi.org/10.1115/1.2899682

DAVIS, J. R. Tensile Testing. 2nd. Materials Park, OH: ASM International, 2004, 283 p.

de SOUZA, T. F. *et al*. Comparison between Neutron Diffraction Measurements and Numerical Simulation of Residual Stresses of a Wire-Drawing Process. Materials Research 15 (6), 2012. p. 1-7.

de SOUZA, T. F. Metodologia de otimização de fieiras de trefilação visando a redução de tensões residuais no material trefilado através de simulação numérica e sua validação experimental. PhD thesis. UFRGS, Porto Alegre, 2017.

de SOUZA, T. F.. "Simulações Computacionais Para Análise E Minimização Das Tensões Residuais No Processo De Trefilação". Master dissertation. UFRGS, Porto Alegre, 2011.

DIAS, V. W. Influência dos Procedimentos de Corte Sobre as Distribuições de Tensões Residuais em Barras Redondas Trefiladas de Aço ABNT 1045. Master dissertation: PPGE3M/UFRGS, Porto Alegre, 2013.

DIAS, V. W. Influência dos processos de fabricação na distorção de eixos em aço ABNT NM 87 grau 1045 temperados por indução. PhD thesis. UFRGS, Porto Alegre, 2018.

DIAS, V. W.; Zottis, J.; Rocha, A. S.; Dong, J.; Epp, J. "Analysis of the Bending Distortion of Automotive Shafts Manufactured from Cold Drawn Bars" *In*: The International Conferences on Distortion Engineering (IDE), p. 3-13. Bremen, 2015

DIAS, V.W. *et al*. “Bending Distortion Analysis of a Steel Shaft Manufacturing Chain from Cold Drawing to Grinding”. Metallurgical and Materials Transactions A. V. 48, Issue 4, 2017. pp 1893–1902. DOI: 10.1007/s11661-016-3948-y

DIAS, V.W.; ZOTTIS, J.; SOARES, C.A.T.; SOUZA, T..F. de; ROCHA, A. da. Study of the influence of anisotropy on the residual stresses generated in the wire drawing process of an AISI 1045 steel. Revista Colombiana de Materiales, 2014, v. 1, p. 130-137.

DIETER, G. E. Metalurgia Mecânica. 2 ed. Rio de Janeiro: Guanabara Dois, 1981.

DIETER, G. E. Mechanical Metallurgy. Singapore: McGraw-Hill, 1988.

DITIX, P. M.; DITIX, U.S. Modeling of Metal Forming and Machining Processes: By Finite Element and Soft Computing Methods. London: Springer, 2008.

DONG, J.; EPP, J.; ROCHA, A. DA S.; NUNES, R. M.; ZOCH, H. W. "Investigation of the Influence Factors on Distortion in Induction-Hardened Steel Shafts Manufactured from Cold-Drawn Rod". *Metall. Mat. Trans. A*, 2016, vol. 47A, p. 877-888, DOI: 10.1007/s11661-015-3250-4.

DZIASZYK, S.; PAYTON, E. J.; FRIEDEL, F., MARX, V., EGGELER, G.. On the characterization of recrystallized fraction using Electron Backscatter diffraction: A direct comparison to local hardness in an IF steel using nanoindentation. Material Science and Engineering A 527 (2010): p. 7854-7864.

EPP, J., *et al*. Interdependence of Distortion and Residual Stress Relaxation of Cold-Rolled Bearing Rings During Heating. Metallurgical and Materials Transactions A. V. 42A, 2010a, p. 1205-1214.

EPP, J.; HIRSCH, T. K.; HUNKEL, M.; WIMPORY, R. C. Combined neutron and X-ray diffraction for the characterization of a case hardened disc. Materials Science Forum. 2010b; 652:37- 43. http://dx.doi.org/10.4028/www.scientific.net/MSF.652.37

ERICSSON, T. The Effect of Final Shaping Prior to Heat Treatment. *In*: Handbook of residual stresses and deformation steel. ASM International: 2002, p. 150-158.

ERICSSON, T. Residual Stresses Produced by Quenching of Martensitic Steels. In Hashmi, S. Comprehensive Materials Processing. Vol. 12, p. 271-298, 2014.

ESPINOZA, A. V. P. Use of the advanced numerical simulation techniques for the study and improvement of steel-profiles manufacturing processes. PhD thesis: Universidad de la Rioja, Espanha, 2007.

EZEILO, A. N.; WEBSTER, G. A. "Advances in Neutrons Diffraction for Engineering Residual Stress Measurements." In Textures and Microstructures. p. 151-71. London, 1999.

FISCHER, F. D.; SCHLEINZER, G. Residual stresses formation and distortion of rail steel. *In*: Handbook of residual stresses and deformation steel. ASM International: 2002, p. 424-436.

FITZPATRICK, M. E. *et al*. Determination of Residual Stresses by X-ray Diffraction – Issue 2. In Measurement good practice guide. United Kingdom, n.52, 2005.

GALAMBOS, T. V. Guide to Stability Design Criteria for Metal Structures. 5 ed. Canada: John Wiley & Sons, 1998.

GAMBIN, W. "A Method of Large Finite Elements." In Computer Methods in Applied Mechanics and Engineering. p. 351-65: Elsevier, 1977.

GEIER, M. "Considerações sobre o atrito para processos de forjamento a frio através do ensaio de compressão do anel". Master dissertation. UFRGS, 2007.

HAUK, V. Structural and Residual Stresses Analysis by Non-Destructive Methods. Elsevier, Amsterdam: 1997.

HILL, R. "A Theory of the Yielding and Plastic Flow of Anisotropic Metals." *In:* Proceedings the Royal of Society, London, 1948.

HIRSCH, T.K.; ROCHA, A. DA S.; NUNES, R.M. “Distortion Analysis in the Manufacturing of Cold-Drawn and Induction-Hardened Components”. Metallurgical and Materials Transactions A, 2013, vol 44, pp. 5806–5816. DOI: 10.1007/s11661-013-1952-z.

HIRSCH, T.K.; ROCHA, A. DA S.; NUNES, R.M. “Characterization of local residual stress inhomogeneities in combined wire drawing processes of AISI 1045 steel bars”. Int. J. Adv. Manuf. Technol., 2014, vol. 70, pp. 661-668, DOI: 10.1007/s00170-013-5314-1.

HOSFORD, W. F. Mechanical behavior of materials. 2nd. Cambridge; New York: Cambridge University Press, 2010. xv, 419 p.

https://www.helmholtz-berlin.de/pubbin/igama_output?modus=einzel&sprache=en&gid=1715&typoid=39942

HUTTON, D. V. Fundamentals of Finite Element Analysis. 1st ed. New York: McGraw-Hill, 2004.

ISO 6507-1. Metallic materials — Vickers hardness test — Part 1: Test method. 2018.

KABAYAMA, L. K.; TAGUCHI, S. P.; MARTÍNEZ, G. A. S. "The Influence of Die Geometry on Stress Distribution by Experimental and Fem Simulation on Electrolytic Copper Wire Drawing." Materials Research 12, no. 3 (2009): p. 281-85.

KALPAKJIAN, S. "Mechanical Testing for Metalworking Processes ". *In*: Handbook of Mechanical Testing and Evaluation. p. 70-78: ASM International, 2000.

KANDIL, F. A.; LORD, J. D.; FRY, A. T.; GRANT, P. V. "A Review of Residual Stress Measurement Methods - a Guide to Technique Selection." NPL Report Materials Center (2001): p. 1-42.

KATEMI, R. J.; EPP, J.; HOFFMANN, F.; STEINBACHER, M. Investigation of residual stress distributions in retained austenite and martensite after carbonitriding of a low alloy steel. Advanced Materials Research v. 996 (2014) p. 550-555. Doi: 10.4028/www.scientific.net/AMR.996.550

KRAUSE, H.; JÜHE, H.H.; KOPP, R.; BALDNER, K.R. Ziehverfahren beeinflusst Eigenspannungszustand, Röntgenographische Untersuchungen an Einzelproben von Draht und Rundstäben. Drahtwelt. 1978; 11:428-432

LANGE, K. Handbook of Metal Forming. Society of Manufacturing Engineers, 2006.

LEE, J. *et al*. Design Optimization of Roller Straightening Process for Steel Cord using Response Surface Methodology. In: AIP Conference Proceedings 908, 581-586 (2007); doi: 10.1063/1.2740873.

LIU, A.F. Mechanics and mechanisms of fracture: an introduction. Materials Park, Ohio: ASM International; 2005. vi 458 p.

LU, J. Prestress Engineering of Structural Material: A Global Design Approach to the Residual Stress Problem. *In*: Handbook of Residual Stress and Deformation Steel. p. 11-26: ASM International, 2002.

LU, J.; Society for Experimental Mechanics (SEM). Handbook of measurement of residual stresses. Lilburn, GA: Fairmont Press; Upper Saddle River, NJ: Distributed by Prentice Hall PTR, ©1996.

LÜBBEN, T.; HOFFMANN, F.; ZOCH, H.-W. T. Distortion Engineering: Basics and Application to Practical Examples of Bearing Races. *In Hashmi, S. Comprehensive Materials Processing*. Vol. 12, p. 299-344, 2014.

MARTINEZ-PEREZ, M. L. *et al*. "Measurement and Modeling of Residual Stresses in Straightened Commercial Eutectoid Steel Rods." Acta Materialia 53 (2005): p. 4415-25.

MARTINS, P., RODRIGUES, J. Tecnologia Mecânica: Tecnologia Da Deformação Plástica. Vol. 1, Lisboa: Escolar Editora, 2005.

MASSÉ, T. *et al*. "Impact of Mechanical Anisotropy on the Geometry of Flat-Rolled Fully Pearlitic Steel Wires." Journal of Materials Processing Technology 211 (2011): p.103-12.

MERKEL, C.; ENGINEER, S. Challenges Arising from Residual Stresses in the Bright Steel Manufacturing Process. *In:* The International Conferences on Distortion Engineering (IDE), p. 87-93. Bremen, 2015

METZ, M. "Caracterização Das Tensões Residuais Originadas No Processo De Trefilação Combinada Do Aço SAE 1048". Master dissertation. UFRGS, 2007.

MEYERS, M.; CHAWLA, K. Mechanical Behavior of Materials. 2 ed. New York: Cambridge University Press, 2009.

MUTRUX, A.; BERISHA, B.; HORA, P. FE Simulation of Cross Roll Straightening: A Strain Tensor Field Approach. Nonuniform 2010, Vols 1 and 2, 2010. 1252: p. 941-948. http://dx.doi.org/10.1063/1.3457658

NAKAGIRI, A.; INAKAZU, N. Relationship between residual stress and texture by multiple pass reduction drawing of titanium wire. Wire Journal International. Vol. 37, no. 12, pp. 58-63, 2004.

NALLA, R. K. *et al*. On the influence of mechanical surface treatments – deep rolling and laser shock peening – on the fatigue behavior of Ti-6Al-4V at ambient and elevated temperatures. Materials Science and Engineering A355 (2003) p. 216-230.

NASTRAN, M., KUZMAN, K. Stabilization of mechanical properties of the wire by roller straightening. J. Mater. Journal of Materials Processing Technology, v. 125–126, p. 711–719, 2002.

NORASETHASOPON, S.; YOSHIDA, K. "Prediction of Chevron Crack Initiation in Inclusion Copper Shaped-Wire Drawing." Engineering Failure Analysis 15 (2008): p. 378-93.

NUNES, R. M. "Análise De Tensões Residuais De Aços AISI 1048 Produzidos Por Trefilação Combinada Visando Minimizar Distorções Pré-Processamento". Master dissertation: PPGE3M/UFRGS, 2008.

NUNES, R. M.; HIRSCH, T. K.; ROCHA, A. S. "Análise De Tensões Residuais Via Difração De Nêutrons Em Barras De Aço AISI 1045 Produzidas Por Trefilação Combinada." *In*: Anais do 65 Congresso Anual da ABM, p. 453-64. Rio de Janeiro, 2010.

NUNES, R.M. Estudo de distorção de barras cilíndricas de aço ABNT 1045 em uma rota de fabricação envolvendo trefilação combinada e têmpera por indução. PhD thesis: PPGE3M/UFRGS, 2012

OH, S. I.; WU, W. T.; TANG, J. P. VEDHANAYAGAM, A. "Capabilities and Applications of Fem Code Deform: The Perspective of the Developer." Journal of Materials Processing Technology 27 (1991): p. 25-42.

OLIENICK FILHO, E. G. "Análise De Estampagem De Chapas Pelo Método De Elementos Finitos: Estudo Da Influência Taxa De Sensibilidade." CEFET-PR, 2003.

PAECH, A. B. Advanced semi-automatic straightening technology. Wire, pp. 2-6, 2008.

PAECH, A.B. Spring Wire Straightening. Springs, p. 55-56, 2007.

PAECH, M., Factors relating to the wire straightening process—process and peripherals. Wire Journal International, 2002. 35(12): p. 64-68.

PAECH, M., Tensile force requirement for the straightening of wire with roller straightening units. Wire Journal International, 2001. 34(6): p. 92-98

PERINI, R. "O uso de difração de raios-x para determinação da tensão residual induzida pelo processo de roleteamento em uma camisa de cilindro de motor Diesel" Master dissertation. USP, 2008.

PUTTEN, K. van; DAUBE, T. Investigation of the roller straightening process for long products. Simufact 12th Roundtable, 2010.

ROBINSON, T.; OU, H. ARMSTRONG, C. G. "Study on Ring Compression Test Using Physical Modeling and FE Simulation." Journal of Material Processing Technology 153-154 (2004): p. 54-59.

ROCHA, A. S. *et al*. "Simulação Computacional De Um Processo De Trefilação Para Produção De Barras Redondas De Aço AISI 1045." Revista Escola de Minas, 2011, p. 513-18.

ROCHA, A. S. Influência do estado superficial prévio na nitretação a plasma do aço M2. PhD Thesis: PPGEM/UFRGS, 2000. p. 198.

ROCHA, A. S.; NUNES, R. M.; FERLAUTO, E. M. "Avaliação Dos Efeitos De Tensões Residuais Através Da Remoção De Material." Estudos Tecnológicos, 2008, p. 157-69.

ROCHA, A. S.; NUNES, R. M.; HIRSCH, T. "Analysis by Design of Experiments of Distortion Potentials in Drawn and Induction Hardened Wire." Materials Research 15, n. 1 (2012).

RUUD, C. "Measurement of Residual Stress ". *In*: Handbook of Residual Stress and Deformation Steel. p. 99-108: ASM International, 2002.

SAE J-403. Chemical Compositions of SAE Carbon Steels. 1994.

SAHIN, M.; ÇETINARSLAN, C. S.; AKATA, H. E. "Effect of Surface Roughness on Friction Coefficients During Upsetting Process for Different Materials." Materials and Design 28 (2007): p. 633-40.

SANTOS, C. A. "Simulação Numérica Da Trefilação Axissimétrica Do Aço Inoxidável 420 Considerando O Efeito Do Caminho De Deformação". PhD thesis. UFMG, 2005.

SANTOS, C. C. "Influência De Parâmetros De Processo No Empenamento De Barras Trefiladas De Aço SAE 9254". Master dissertation. UFRGS, 2008.

SCHAEFFER, L.; BRITO, A. M. G.; GEIER, M. "Numerical Simulation Using Finite Elements to Develop and Optimize Forging Process." Steel Research International 76 (2005): p. 199-204.

SOARES, C.A.T. Análise das Tensões Residuais no Processo de Trefilação Considerando os Efeitos de Anisotropia. Master dissertation: PPGE3M/UFRGS, Porto Alegre, 2012.

SONMEZ, F. O.; DEMIR, A. “Analytical relations between hardness and strain for cold formed parts”. Journal of Materials Processing Technology 186, 163–173. Turkey, 2007.

SRIMANI, S. L.; PANKAJ, A. C.; BASU, J. Analysis of end straightening of rail during manufacturing. International Journal of Mechanical Science 47 (2005), p. 1874-1884.;

STEINBACHER, M., CLAUSEN, B., HOFFMANN, F., ZOCH, H. W. Influencing parameters on the distortion of disk-shaped gear wheelbase body derived from carburization. *In*: Proceedings of conference in honor of prof. dr. Božidar Liščić. Croatia, 2009, p. 343-349.

TABOR, D. “A simple theory of static and dynamic hardness”. Proc R Soc Lond Ser A: Math Phys Sci, 192 (1029) (1948), pp. 247-274.

TALAMINI, B.; GORDON, J.; PERIMAN, A. B. Finite element estimation of the residual stresses in roller-straightened rail. *In*: Proceedings of ASME International Mechanical Engineering Congress. USA, 2004.

TANGE, A.; ANDO, K.; “Study on shot peening processes of coil springs”, Proc. 6th Int. Conf. on Residual Stresses, Oxford, UK, 2000, p897–904.

TEKKAYA, A. E. "State-of-the-Art of Simulation of Sheet Metal Forming." Journal of Material Processing Technology 103 (2000): p. 14-22.

TEKKAYA, E. A. "A Guide for Validation of Fe-Simulations in Bulk Metal Forming." The Arabian Journal for Science and Engineering 151, no. 1C (2005): p. 58-62.

TISZA, M. "Numerical Modeling and Simulation in Sheet Metal Forming." Journal of Material Processing Technology 151 (2004): p. 58-62.

TORIBIO, J. *et al*. “Analysis of the Bauschinger Effect in Cold Drawn Pearlitic Steels”. Metals no. 10, 114 (2020) doi:10.3390/met10010114

van ACKER, K.; ROOT, J.; van HOUTE, P.; AERNOUDT, E. Neutron Diffraction measurement of the residual stress in the cementite and ferrite phases of cold-drawn steel wires. Acta Materialia., 10 (1996), p. 4039. http://dx.doi.org/10.1016/S1359-6454(96)00051-1

van BAEL, A. *et al*. "Anisotropic Finite-Element Analysis of Plastic Metal Forming Process." In Texture and Microstructures. p. 1007-12, 1991, vol.14.

VARNEY, B.E., FARRIS, T.N., 1997. Mechanics of roller straightening. *In*: 39th Mechanical Working and Steel Processing Conference, Indianapolis, IN, October 19–22 1997, pp. 1111–1121. Iron and Steel Society, Warrendale, PA.

WALTON, H. W. "Deflection Methods to Estimate Residual Stress ". *In*: Handbook of Residual Stress and Deformation Steel. p. 89-98: ASM International, 2002.

WANG, Z.; GONG, B. "Residual Stress in the Forming of Materials." *In*: Handbook of Residual Stress and Deformation of Steel. p. 141-49. Canada: ASM International, 2002.

WEBSTER, G. A.. "Role of Neutron Diffraction in Engineering Stress Analysis. In Measurement of Residual and Applied Stress Using Neutron Diffraction." Kluwer Academic Publishers (1992): p. 21-35.

WIMPORY, R.; BOIN, M. Emphasizing the accuracy of the uncertainty of residual stress determination using neutron diffraction. 2011. AVAILABLE IN:

YANG, F. *et al*. "Stress Evolution of Cold-Drawn Pearlitic Steel Wire Subjected to Uniaxial Tension." Materials Science and Engineering 487 (2008): p. 468-72.

YOSHIDA, K.; SUGIYAMA, T. Analysis of the straightening of drawn wires using rollers by the finite-element method (FEM). Wire Journal International. V.42, nº 5, 2009, p. 52-56

YU, J; ZHANG, Q.; YUE, Z. "Tensile mechanical properties of Ni_3Al nanowires at intermediate temperature". RSC Advances, issue 40, 2014, p. 20789–20796.

ZHAO, Y.; GUO, D.; HU, F. Finite element simulation of web falling during heavy rail roller straightening. Procedia Earth and Planetary Science 2 (2011), p. 44-49.

ZOCH, H. W. Distortion engineering: vision or ready to application? Wiley Inter Science 40, nº. 5 (2009): p. 342-348. doi: 10.1002/mawe.200900457

ZOCH, H. W. "From Single Production Step to Entire Process Chain – the Global Approach of Distortion Engineering." Wiley Inter Science 37, no. 1 (2006): p. 6-10. doi 10.1002/mawe.200500958.

ZOTTIS, J. Modelagem e análise numérica de variações dos parâmetros não controláveis em um sistema de trefilação de barras. Master dissertation: PPGE3M/UFRGS, Porto Alegre, 2013.

ZOTTIS, J.; DIEHL, C. A. T. S.; ROCHA, A. da S. "Evaluation of experimentally observed asymmetric distributions of hardness, strain and residual stress in cold drawn bars by FEM-simulation". Journal of materials research and technology 7 (4), 2018, 469-478.